Orbital Reflectometry of Nickel Oxide Heterostructures

Von der Fakultät Mathematik und Physik der Universität Stuttgart
zur Erlangung der Würde eines Doktors der Naturwissenschaften
(Dr. rer. nat.) genehmigte Abhandlung

Vorgelegt von

Meng Wu

aus Anhui, China

Hauptberichter:	Prof. Dr. Bernhard Keimer
Mitberichter:	Prof. Dr. Martin Dressel
Tag der mündlichen Prüfung:	09. Feb. 2015

Max-Planck-Institut für Festkörperforschung
Stuttgart 2015

Contents

1. Introduction

1.1. Transition metal oxides and their heterostructures

Strongly correlated materials are often found among compounds of $3d$ transition metals or rare-earth compounds and show a wide diversity of physical properties [67, 102]. The origin of those phenomena is related to the small extent of the radial distribution functions so that the on-site electron-electron Coulomb interaction becomes crucial, as well as a low energy scale of spin fluctuations. One electron band structure calculation can successfully explain the ground state electrical and magnetic properties for a large variety of solids, but they fail for transition metal oxides (TMOs), such as CoO, FeO, NiO, which are predicted to be metallic within the local density approximation (LDA) band structure calculations, but experimentally they are found to be insulating. Mott and Hubbard explained the band gap formation by introducing the electron-electron interaction [64, 102]. The idea is summarized as follows:

Two energy parameters play a competing role here: the kinetic energy t which is related to the overlap of wave functions on adjecent lattice sites and the potential energy U which refers to the on-site electron-electron Coulomb interaction. If the electron-electron interaction U is larger than the hopping term t (which is proportional to the TM $3d$ band width w based on the tight-binding model), the strong electron-electron repulsive Coulomb interaction splits the transition metal $3d$ band into two bands. As shown in Fig. 1.1(a), the upper Hubbard band and the lower Hubbard band are separated by the energy U which is typically of order several eV. The Mott-Hubbard model works properly for early $3d$ transition oxide compounds (like Ti, V compounds) with a corresponding band gap $E_g \sim U - w$ [12]. The band gap originates from the so called d-d type charge fluctuation in the form of $d^n d^n \rightarrow d^{n-1} d^{n+1}$, and the on-site Coulomb energy is expressed as: $U = E(d^{n+1}) + E(d^{n-1}) - 2E(d^n)$ [99].

However, differences arise for the late transition metal oxides (e.g. Co, Ni, Cu compounds) since less energy is required for the charge transfer from $2p$ ligand states to the $3d$ band, known as charge-transfer insulators (Fig. 1.1(b)) [12, 37]. The energy gap there is of the form $E_g \sim \Delta - W$, where Δ and W denote the ligand-to-metal charge transfer energy and the ligand band width,

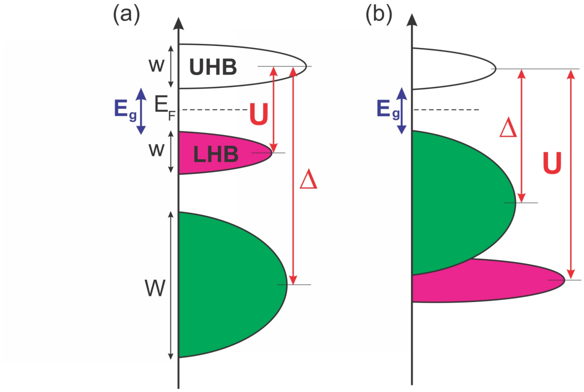

Figure 1.1.: Energy-level scheme for (a) Mott-Hubbard insulators: $U < \Delta$ with corresponding energy gap $E_g \sim U - w$ and (b) Charge-transfer insulators: $U > \Delta$ with energy gap $E_g \sim \Delta - W$, where w, W denote the band width of transition metal ions and ligand ions, respectively.

respectively. Note that this ligand band width W is much larger than the TM $3d$ bandwidth w, i.e. w can be neglected. For charge-transfer insulators, the p-d type band gap is related to the charge fluctuation $d^n d^n \rightarrow d^{n+1} d^n \underline{L}$, and the charge transfer energy is defined by $\Delta = E(d^{n+1}\underline{L}) - E(d^n)$, with $\underline{L}$ denoting a ligand hole. The charge transfer energy Δ strongly depends on the electronegativity of the transition metal ion. A cluster calculation shows that with increasing electronegativity from Mn to Cu and the same ligand environment, Δ decreases [12]. A classification of transition metal compounds can be made with the Zaanen-Sawatzky-Allen scheme which is based on the Andenson-impurity model (or the p-d model), and explicitly takes into account the ligand-metal interaction [149]. The nickel oxide compounds with large rare-earth ions, i.e. $LaNiO_3$ (LNO) and $PrNiO_3$ (PNO) which are of particular interest here, are regarded as self-doped Mott insulators with a negative charge transfer energy [71, 100, 101], as emphasized hereafter.

Regarding the electronic structures of $3d$ transition metal ions, $3d$ orbitals have a 5-fold degeneracy in the atomic limit, namely degenerate d_{xy}, d_{yz}, d_{xz}, $d_{x^2-y^2}$ and $d_{3z^2-r^2}$ orbitals. The orbital degeneracy brings a new degree of freedom to the system and is without any doubt an important source for the diversity of the electronic phase behaviors. In a cubic crystal field, the orbital degeneracy is lifted into e_g (2-fold degenerate) and t_{2g} (3-fold degenerate) orbitals. Considering a Ni ion surrounded by an octahedral environment with six oxygen ions (O_h symmetry), the Coulomb interaction along the in-plane direction (x or y direction in Cartesian coordinates) is higher than along the diagonal direction, resulting in a lowering of the energy of the t_{2g} orbitals (d_{xy}, d_{yz}, d_{xz} orbitals). The corresponding energy splitting is called crystal field splitting with a notation $10Dq$, as shown in Fig. 1.2. The interplay among orbital, charge, spin and lattice dynamics causes a variety of phenomena, e.g. the colossal magnetoresistance in manganese oxides [113, 137]. For the nickel oxide compounds of interest here, Ni^{3+} has nominally a low spin $3d^7$ electron configuration with a full occupation of the t_{2g} orbitals and a single electron ($S = 1/2$) in the doubly degenerate e_g level. Compared to bulk nickel oxide compounds without any preference of e_g orbital occupations, an additional splitting of the degeneracy of the e_g level into $d_{x^2-y^2}$ and $d_{3z^2-r^2}$, can be realized by either confining the nickelates layers between two insulating layers in a heterostructure or lowering the crystal symmetry, e.g. D_{4h} symmetry via strain (right plot in Fig. 1.2 shown as an example of a compressed octahedron) [20, 53]. Recently it was shown that dimensionality reduction from 3D to 2D is crucial in tuning the electronic phase transitions of TMO heterostructures [14, 20, 33].

The diversity of the physical properties of TMOs also largely depend on the detailed composition and the crystal structure. Many ternary TMOs show the same basic structure block known as the perovskite structure, which exhibits the general chemical formula $\mathrm{ABO_3}$. Fig. 1.3(a) shows a typical perovskite structure with ideal cubic symmetry, where each transition metal ion B is surrounded by six oxygen ions, forming a regular octahedra.

Many perovskites exhibit orthorhombic, tetragonal or monoclinic structures due to octahedral distortions or cation displacements (such as in some ferroelectric materials like $\mathrm{BaTiO_3}$, $\mathrm{PbTiO_3}$, etc) [43]. The distortion of the crystal structure was found to depend on the so-called tolerance factor, which is defined as [78]:

$$t = \frac{r_A + r_O}{\sqrt{2}(r_B + r_O)}, \tag{1.1}$$

where r_A, r_B and r_O represent the ionic radius of the A-cation, B-cation and oxygen ion, respectively. The perovskite structure is stable when $0.75 < t < 1$ [72], the structure is of cubic symmetry if $t \sim 1$. For $0.75 < t < 0.9$, the A-cation is too small to fit the interstitial site which is compensated by a distortion of the cubic parent structure. This structural distortion, in good

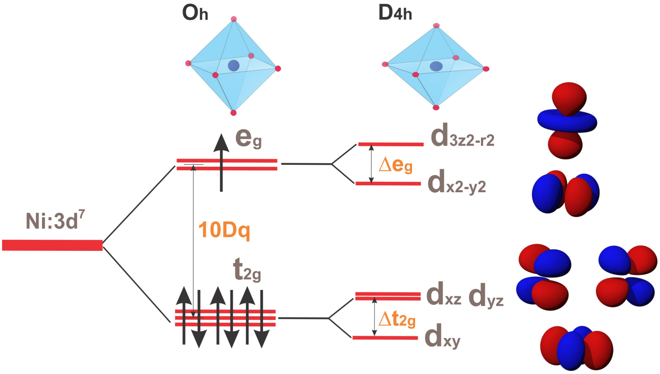

Figure 1.2.: Illustration of the orbital degeneracy for Ni^{3+} ion with $3d^7$ configuration. The 5-fold degenerate orbitals are split into e_g and t_{2g} due to a crystal field effect with O_h symmetry. The corresponding energy parameter is denoted as $10Dq$. A further splitting of e_g states into $d_{x^2-y^2}$ and $d_{3z^2-r^2}$ orbitals, and t_{2g} states into d_{xy} as well as d_{xz}, d_{yz} orbitals can be obtained in a lower D_{4h} symmetry, with the corresponding energy splitting represented by Δ_{e_g} and $\Delta_{t_{2g}}$, respectively. Note that we shown the D_{4h} symmetry for the case of a compressed octahedra here with a lower energy of the $d_{x^2-y^2}$ orbital compared to the $d_{3z^2-r^2}$ orbital. For the case of an elongated octahedra, this order is reversed. The images of atomic orbitals are adapted from wikipedia website.

approximation, can be described by tilts and rotations of the octahedra.

Fig. 1.3(b) shows a prototype of a perovskite compound with $GdFeO_3$-type, where the distortion appears as tilts of anions in BO_6 octahedra. The rotation angles along the crystal a-, b-, c-axes are denoted as α, β and γ, which can be different in each direction, i.e. $\alpha \neq \beta \neq \gamma$. A common way to describe octahedral distortion is known as the Glazer notation in the form of a^* b^* c^* [43]. The superscript $*$ can be $+$ or -, denoting that neighboring octahedra along a certain crystal axis tilt in-phase or antiphase, respectively. And $*$=0 labels no tilts along a particular axis. For instance, an $a^-b^-c^+$ rotation pattern indicates unequal tilt angles α, β, γ around the three axes, and the octahedra rotation along the a-axis, b-axis are antiphase, antiphase and in-phase along the c-axis. The antiphase rotation of the octahedra along a certain crystal axis

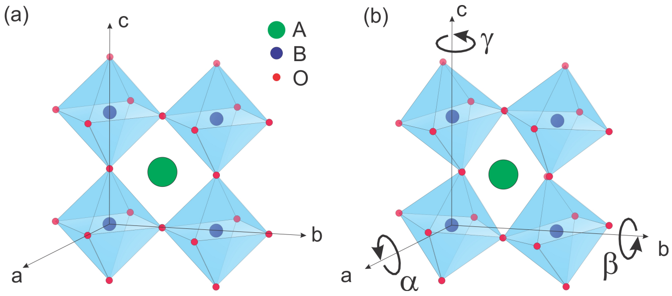

Figure 1.3.: Panel (a): crystal structure of a representative perovskite compound ABO_3 with cubic symmetry, where each B ion and six oxygen ions form an octahedra; Panel (b): a prototype of the distorted orthorhombic structure with tilted octahedra. The rotations along the crystal a-, b-, and c-axes are represented by α, β and γ.

results in a doubling of the unit cell (u.c.), and hence generates to half-integer diffraction peaks in reciprocal space. The antiphase and in-phase tilts produce two distinct classes of reflections based on the space-group symmetry. Special selection rules exist for different rotation patterns (for details see Ref. [43]), which can be used to determine the space group through x-ray diffraction experiments. A full crystallographic refinement of the half-order Bragg peak intensities allows one to obtain the oxygen positions quantitatively [34, 88, 92].

The richness of physical properties of TMOs makes them of particular interest when combining those materials in heterostructures. Perovskite superlattices offer the perspective to design new correlated systems via material engineering [65]. In the following, a brief literature review of various physical properties of transition metal oxide heterostructures is presented.

At the interface between an antiferromagnetic $CaMnO_3$ and a paramagnetic metal $CaRuO_3$, ferromagnetism was found which is attributed to a charge transfer effect at the interfaces [35, 133, 148]. A similar effect was also reported for $LaMnO_3$-$SrMnO_3$ interfaces [10, 143].

The interfaces between two insulating materials $LaAlO_3/SrTiO_3$ (LAO/STO) attracted wide-spread interests due to the observation of a high mobility 2D electron gas [106]. The two insulators have differently charged atomic layers in the ionic limit, i.e. $(La^{3+}O^{2-})^+$, $(Al^{3+}(O^{2-})_2)^-$ for the LAO compound and neutral $(SrO)^0$, $(TiO_2)^0$ layers in STO, therefore in terms of electrostatics, a polar-nonpolar discontinuity is present at the interface, which possibly reconstructs by a charge transfer from LAO to STO in order to avoid the so-called polar catastrophe [7, 136]. Another interpretation of the origin of the conducting interface is related to oxygen vacancies, possibly resulting in oxygen-deficient STO layers [61, 73]. Furthermore, a coexistence of ferrromagnetic and superconducting phases was reported for this heterostructure, which provides a fascinating system for the study of the interplay between superconductivity and magnetism [30, 83, 114].

Instead of local chemical doping introducing defects and disorders in the bulk system, heterostructures can also be used to modulate the dopants at the interface, e.g. a quantum well of $LaVO_3$ is placed between LAO layers, where a reconstruction charge is transferred to the $LaVO_3$ quantum well from the LAO layers through oxygen vacancies and lattice distortions [62, 134].

Despite the nonsuperconducting constituents, superconductivity was observed at the interface of a heterstructure composed of insulating La_2CuO_4 and overdoped $La_{2-x}Sr_xCuO_4$ compounds, and attributed to a hole redistribution from overdoped cuprate layers to undoped layers [44, 130].

At the interface of the superconductor $YBa_2Cu_3O_7$ and the ferromagnetic materials $La_{2/3}Ca_{1/3}MnO_3$ or $LaMnO_{3-\delta}$, a flow of the charge across the interface from Mn to Cu ions was reported, which induces a reconstruction of the d-orbital occupancies and the magnetic profile in the interfacial Cu cations [17, 18]. The magnetic proximity effect was found to strongly depend on the electronic structure of the manganite layers [121]. A detailed MnO_6 octahedra rotation mode shows superconductivity-induced line-shape anomalies as a function of the superconducting layer thickness, as investigated by a Raman scattering study of the lattice dynamics [32].

Interfaces composed of rare-earth nickel oxides, $LaNiO_3$-$LaAlO_3$ (LNO-LAO) superlattices grown along the diagonal (111) direction form an artificially buckled honeycomb lattices equivalent to the graphene lattice, which are predicted to show exotic electronic and topological states [119, 145]. In a heterostructure composed of paramagnetic LNO and ferromagnetic $LaMnO_3$, a shift of the magnetic hysteresis loop was observed known as exchange bias effect, indicating interface-induced magnetism in the paramagnetic LNO layers [31, 42]. When the nickelate layers are sandwiched by large band gap insulators, orbital manipulation can be achieved through a combination of quantum confinement and effect of the strain. In this way, LNO-LAO heterostructures grown along the pseudo-cubic (001) directions are predicted to show a high T_c cuprate-like Fermi surface [20, 53]. We will focus on this topic in the following.

1.2. Nickel oxide based heterostructures

Before we address the nickel oxide based heterostructures composed of $\mathrm{ANiO_3}$ (ANO) and large band-gap insulating layers, let us first review the properties of bulk nickleates.

Rare-earth nickel oxides of composition ANO (A-trivalent rare earth, A= La to Lu) exhibit a first-order metal-insulator transition (MIT) and unusual magnetic order of the Ni spins for $\mathrm{A} \neq \mathrm{La}$, which have attracted considerable recent interest. Fig. 1.4 shows the phase diagram summarizing the metal-insulator transition temperature T_{MIT} and the magnetic transition temperature T_{Neel} for different nickelates versus the tolerance factor and versus the Ni-O-Ni bond angle [16]. T_{MIT} is structurally related to the tolerance factor, which is defined as the ratio of ionic bond distances between A-O and Ni-O. From La to Lu, the ionic radius decreases accompanied with structural distortions and a reduction of the tolerance factor, resulting in a pronounced deviation of the Ni-O-Ni bond angle from 180°.

The LNO with the largest ionic radius, remains metallic and paramagnetic at all temperatures [138]. For the larger ions $\mathrm{A} = \mathrm{Pr}, \mathrm{Nd}$, which are close to the vicinity of the phase diagram, the T_{MIT} and the T_{Neel} ordering occur at a common temperature [45, 138]. The ground state antiferromagnetic

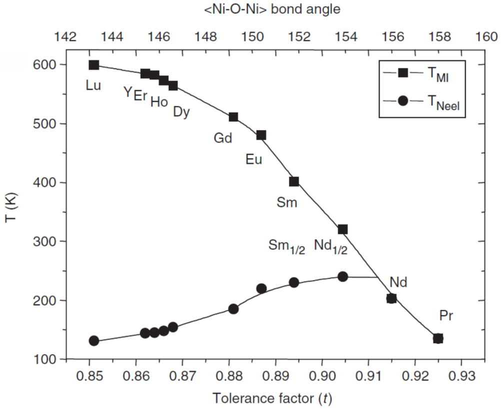

Figure 1.4.: Phase diagram of the resistive transition temperature T_{MIT} and the magnetic transition temperature T_{Neel} for different nickelates versus the tolerance factor and the Ni-O-Ni bond angle [16].

structure is often described in terms of a “up-up-down-down” sequence, i.e. non-collinear magnetic ordering as observed from resonant soft x-ray diffraction [122, 123, 132]. For ANO with smaller A ions, the onset of antiferromagnetic order was found to be lower than the MI transition. To date, the underlying mechanism of this transition is still highly debated, in particular for the members of the ANO family with larger rare earth ions, like Pr or Nd [2, 3, 45, 71, 81, 82, 94, 95]. For $PrNiO_3$ (PNO) and $NdNiO_3$ (NNO), evidence for charge disproportionation with $3d^{7-\delta}$ and $3d^{7+\delta}$ configurations on neighboring Ni sites was reported from high-resolution powder neutron diffraction and hard x-ray absorption measurements [94, 95]. A recently introduced model stresses the central role of the p-orbitals on the oxygen ligands ($\underline{L}$) and reinterprets these data in terms of a “volume collapse” of neighboring octahedra without charge transfer $((d^8\underline{L})_i(d^8\underline{L})_i \rightarrow (d^8\underline{L}^2)_{S=0}(d^8)_{S=1})$ [71]. An alternative theoretical approach based on an itinerant-electron model attributes the MIT in PNO and NNO to spin-density-wave formation driven by Fermi surface nesting [81, 82]. Photoemission experiments have indeed found a strongly nested Fermi surface, with a nesting vector approximately matching the wave vector characterizing the magnetic order [9, 147].

Our interest in nickel oxide heterostructures originates from the initial proposal by J. Chaloupka and G. Khaliullin, where they proposed a similar electronic structure as high-T_c cuprates and possible superconductivity in nickelate superlattices [20]. The key structural and electronic properties of high-T_c superconductivity are: no orbital degeneracy, spin-one-half, quasi-two dimensionality and strong antiferromagnetic correlations. LNO with $S = 1/2$ and confined between a large band gap insulator is quasi-2D since the electron hopping along one direction is suppressed, resulting in a lifting of e_g orbital degeneracy which is further enhanced by the crystal field splitting induced by strain, as illustrated in Fig. 1.5. It is thus expected an effective one-band configuration with the electron confined in the single $d_{x^2-y^2}$ orbital. In Ref. [20], the mean-field phase diagram was obtained by considering two main variables: the strength of the intra-atomic Hund coupling and the strength of charge transfer processes, indicating a phase with preferential occupation of the $d_{x^2-y^2}$ planar orbitals similar as in cuprates, as well as enhanced antiferromagnetic correlations.

Subsequent calculations based on the density functional theory provided divergent results [48, 49, 53]. Local density approximation and its combination with dynamical mean-field theory were used to calculate the band structure and the corresponding 2D Fermi surface for a composition of 1 u.c. LNO surrounded by an isostructural insulating layer LAO [58]. The insulating layers block the electron propagation along the c-axis and induce a predominant occupation of the $d_{x^2-y^2}$ orbital near the Fermi level. Tensile strain, as an additive parameter, further raises the orbital separation. The electronic correlations induce a cuprate-like single-sheet Fermi surface of $d_{x^2-y^2}$ symmetry, indicating the possible realization of superconductivity by heterostructuring [53]. Another important ingredient, i.e. the chemical control of the insulating layer, was addressed from first principles by Han *et. al* [48]. The calculations were done for different blocking layers $\mathrm{LaXO_3}$ ($\mathrm{X = B, Al, Ga, In}$), where the X-O-Ni hybridization along the surface normal direction serves as a tuning parameter. As the ionic radius of X increases, the overlap of $\mathrm{X}\,s$ - $\mathrm{O}\,2p_z$ is expected to be reduced, resulting in the enhanced hybridization of $\mathrm{Ni}\,d_{3z^2-r^2}$ - $\mathrm{O}\,2p_z$ and an enhanced $d_{x^2-y^2}$ orbital occupation (see Fig. 1.5(c)). Furthermore, Han *et al.* reported density mean field theory calculations taking into account the effect of oxygen explicitly, and claimed that the strong electron-electron interaction (Hubbard $U \neq 0$) greatly reduces the preferred $d_{x^2-y^2}$ orbital occupation. Those findings excluded a single-sheet Fermi surface in a realistic many-body model of nickelate heterostructures [49]. Recently, Parragh *et al.* claimed that the crucial parameter responsible for this discrepancy is the total number of d-orbital occupancy, which varies from a Ni $3d^7$ with one electron per Ni site on average to a Ni-O hybridized system with a large filling of ~ 1.7 electrons per site, and introduces differences of the ground state correlations [107].

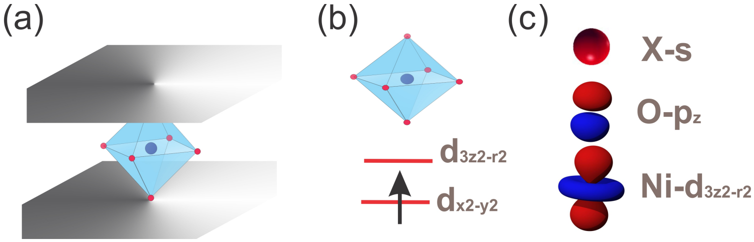

Figure 1.5.: Illustration of the possibilities of orbital manipulation in nickel oxide heterostructures: (a): confinement suppresses the electron dispersion along the out-of-plane direction; (b): tensile strain splits the e_g orbital degeneracy, with a preferred orbital occupation of the $d_{x^2-y^2}$ level; (c): the hybridization of X ions with oxygen ($\mathrm{X}\,s$ - $\mathrm{O}\,p_z$) affects the hybridization of the $\mathrm{Ni}\,d_{3z^2-r^2}$ - $\mathrm{O}\,2p_z$ orbitals. The images of atomic orbitals are adapted from wikipedia website.

Experimentally the questions were to date mainly addressed by x-ray absorption spectroscopy. The polarization dependent natural linear dichroism reflects the different orbital occupations, however, the effect of strain on orbital or spin degrees of freedom is not completely intuitive due to the octahedral rotations in the perovskite structure [115, 116]. The experimental results vary and partly disagree with theory. Freeland *et. al* reported a $\sim 5\%$ orbital polarization for 1 u.c. LNO-LAO superlattices under tensile strain and no orbital polarization for corresponding superlattices under the compressive strain. An asymmetric response of the e_g orbital splitting with strain was proposed, i.e. a splitting of orbital energies (with a lower energy of the $d_{3z^2-r^2}$ orbital compared to the $d_{x^2-y^2}$ orbital) is found for the case of compressive strain, whereas no splitting is found for the case of tensile strain [36]. It was argued that the distorted octahedra under tensile strain induce a charge disproportionation at the Ni sites, similar to the statement made for ultra-thin LNO films [19]. Our measurements are pretty of variance with these reports, as will be presented in Chapter 4 and Chapter 5.

Optical ellipsometry measurements showed that superlattices with 2 unit cell thick LNO layer stacks undergo a metal-insulator-transition around 150 K. In addition, the low-energy muon spin relaxation measurements revealed magnetic ordering below 50 K. In contrast, superlattices with 4 u.c. thick LNO layer stacks are metallic and paramagnetic down to the lowest temperatures, indicating that the electronic and the magnetic properties are controlled by the dimensionality [14]. Contradicting thickness dependencies were found. While we reported a transition between 2 u.c. and 3 u.c., other groups found a critical thickness of 5 u.c.. Liu *et. al.* reported a similar electronic phase transition in $(LNO)_n$-$(LAO)_3$ ($n = 3, 5, 10$) superlattices, where the results show a crossover from itinerant electron behavior to localized behavior with 5 u.c. LNO layers [87]. In terms of the magnetic structure, muon spin relaxation is a local probe of magnetic moments and only provides indirect information about the type of magnetic correlations between Ni moments. However, the ordered moment was estimated to be $\mu_{Ni} \approx 0.5\ \mu_B$ and ferromagnetic order was ruled out. Later on, the results from resonant x-ray diffraction demonstrated the existence of an antiferromagnetic spin-density wave in 2 u.c. LNO-based superlattices [33]. More precisely, they show an ordering vector $q_{so} = (1/4, 1/4, L)$ and different moment directions for superlattices under tensile and compressive strain due to the different relative occupation of the Ni d-orbitals, which in turn control the magneto-crystalline anisotropy via the spin-orbit coupling (Fig.3 of Ref. [33]). Octahedral distortions in nickelates are important and non-negligible for the electronic properties. Scanning transmission electron microscopy and x-ray diffraction studies showed that the NiO_6 tilts and distortions in the superlattices are generally different from those of the bulk constituents, which may have an important influence on their transport properties [27, 28, 34, 66, 92].

Besides the influence of dimensionality in electronic phase transitions reported in LNO-based superlattices mentioned above, epitaxial strain was reported to induce similar metal-insulator transition in other ANO systems. In particular, the MIT of PNO thin films can be suppressed by compressive strain induced by the lattice constant mismatch with the underlying substrate [79], resulting in metallic transport behavior down to the lowest temperatures akin to bulk LNO. A related strain-mediated MIT was also observed for ultra-thin NNO films [85, 86]. A recent Raman scattering study revealed two different low-temperature ground states in PNO-based SLs with insulating $PrAlO_3$ (PAO) blocking layers, depending on the strain imposed by the substrate [60], which is in agreement with the theoretical predictions for a spin density wave phase with charge order as a secondary order parameter [81, 82]. The strain controlled phases in nickelate heterostructures open the opportunity for novel device applications such as antiferromagnetic spintronics [89, 128].

1.3. Scope of this thesis

In Chapter 2, we will discuss the theoretical background of x-ray spectroscopy. First, we present the quantum mechanical approach of x-ray absorption phenomena through Fermi's Golden rule, followed by a derivation of the polarization dependent sum rules. Then, we discuss the resonant x-ray scattering process, especially focusing on the simulation of the x-ray reflectivity in Parratt's recursive and matrix formalisms. The data processing as well as the idea of the "orbital reflectometry" technique will be addressed. A further interpretation of the core-hole excitations, relevant for x-ray absorption is presented in terms of cluster calculations. Finally, we briefly introduce the experimental aspect, i.e. synchrotron radiation facilities and the experimental setup.

In Chapter 3, a summary of the crystal structures of the studied compounds is presented. We start from presenting a brief introduction of the pulsed laser deposition method, then the characterization of the surface morphology through atomic force microscopy, followed by the investigation of the crystal quality as well as the lattice parameters by x-ray diffraction measurements, and finally the *dc* resistivity measurements for initial characterization of the electronic properties.

Chapter 4: A major part of this PhD thesis is devoted to applying the "orbital reflectometry" technique to obtain layer-resolved orbital occupation profiles of LNO-based superlattices. We present the experimental results and the data analysis in detail, and determine the layer-resolved orbital polarization quantitatively. Finally we directly compare our experimental data with the results of density functional theory (DFT).

In Chapter 5, we discuss orbital reflectometry results on PNO-based superlattices. We focus on the temperature as well as strain dependent orbital physics in detail, which is indicative for the close interaction between orbital, charge, and spin degrees of freedom. Similar to the LNO-based heterostructures in Chapter 4, the lattice-orbital response is studied in detail.

In Chapter 6, the x-ray reflectometry technique has been tested to probe octahedral distortions. We start from presenting the idea of the experiment, then the experimental results and the analysis, followed by a discussions and simulations.

2. Backgrounds and Principles

Spectroscopy measures the energy spectrum of a solid, which can be used to provide both the static properties such as lattice arrangement, the magnetic structure and the dynamic properties such as phonons, magnons in transition metal oxides. Electromagnetic (EM) waves are a common source probe of the microscopic properties of solids. Basic experimental schemes between an EM wave and the solid are classified into absorption and scattering. In an x-ray absorption spectroscopy (XAS) experiment, core electrons are excited into the unoccupied states or into the continuum (as shown in Fig. 2.1). The excitations to the unoccupied bound states are related to the chemical binding energy of a material. We can calculate the binding energy based on the Bohr model of an atom in a semi-classical approach where the binding energy is expressed as $E = -\frac{1}{n^2}\frac{Z^2e^2}{2a_0}$ with n denoting the main quantum number, $a_0 = 0.529\,\text{Å}$ denotes the Bohr radius and Z is the atomic number. Thus, XAS has the big advantage of being an element specific probe. For instance, the resonant absorption energy shifts to higher energies with increasing Z for $3d$ transition metal elements from Sc to Zn. According to the Stoner-model for a ferromagnetic metal, the different spin oriented states form majority and minority bands depending on the relative electron populations. Spin-band resolved x-ray magnetic circular dichroism measurements can be used to study the local spin and orbital moment in a quantitative way for a particular element of interest. The difference of the absorption intensity with left- and right-circularly polarized light is directly proportional to the atomic magnetic moment, which is given by the difference of the occupations of the two bands.

Elastic x-ray scattering/diffraction is a photon-in photon-out process, where elastic means that there is no energy loss during the scattering process. Non-resonant x-ray scattering is commonly used for determining the crystal structure, but can also probe the magnetic ordering [24, 25] which is a difficult experiment and largely limited by the small scattering cross section. The problem is overcome by tuning the x-ray energy to an absorption edge where the scattering cross section is dramatically enhanced, namely, resonant elastic x-ray scattering (REXS). The momentum transfer provides the information about the periodicity of the density modulation. Further polarization analysis as well as the azimuthal dependent scattering intensity can give detailed

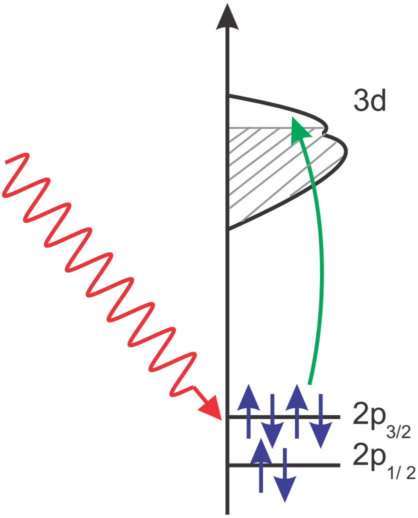

Figure 2.1: A schematic illustration of the x-ray induced core-hole excitation from $2p$ to unoccupied $3d$ states. The $2p$ states split into $2p_{3/2}$ level ($J=l+s=1+\frac{1}{2}=\frac{3}{2}$) and $2p_{1/2}$ level ($J=l+s=1-\frac{1}{2}=\frac{1}{2}$) due to spin-orbit coupling.

information on the charge and magnetic structure [33, 41, 123, 132].

2.1. X-ray absorption

2.1.1. Fermi's Golden rule

Fermi's Golden rule is the core of understanding spectroscopical phenomena, which is characterized by a quantum mechanical transition probability of an electron from an initial state $|i\rangle$ to a final state $|f\rangle$. The transition probability is expressed as:

$$T_{i\rightarrow f}=\frac{2\pi}{\hbar}|M_{if}|^2\rho=\frac{2\pi}{\hbar}|\langle f|H^{'}|i\rangle|^2\rho, \tag{2.1}$$

where M_{if} is the matrix element, $H^{'}$ is the electron-photon interaction Hamiltonian which can be treated as a perturbation to the system, ρ is the joint density of states of the final state. When neglecting the magnetic part of the incident EM wave as well as the displacements of the nuclei by the incoming photon, the perturbation Hamiltonian for electron-photon interaction reads:

$$H^{'}=\vec{E_{in}}\cdot(e\vec{r})=\hat{\epsilon}\cdot E_0(\omega)\exp[i(\vec{k}\vec{r}-\omega t)]\cdot(e\vec{r}), \tag{2.2}$$

where $\vec{E_{in}} = \hat{\epsilon} \cdot E_0(\omega) \exp[i(\vec{k}\vec{r} - \omega t)]$ is the electric field of the incident EM wave, $\hat{\epsilon}$ characterizes the beam polarization, $E_0(\omega)$ is the amplitude, and the last term $(e\vec{r})$ denotes the electric dipole moment of electrons. In the electric dipole approximations, making the assumption that the phase change of the electric field is negligible so that $\exp(i\vec{k}\vec{r}) \approx 1$, the transition matrix can be rewritten as:

$$M_{if} = |\langle f|E_0\hat{\epsilon} \cdot \vec{r}|i\rangle|. \tag{2.3}$$

In case of core-hole excitations, relevant for x-ray absorption process, a good approach is to describe the core electrons by hydrogen-like wave functions. The initial state $|i\rangle$ and the final state $|f\rangle$ can be expressed using spherical harmonics:

$$\psi_{nlm} = R_{nl}(r)\ Y_{lm}(\theta, \phi)\ \chi(s, m^s). \tag{2.4}$$

Neglecting all the pre-factors, the matrix element can be expressed as the product of the radial, angular and spin parts:

$$\begin{aligned} \langle f|\hat{\epsilon} \cdot \vec{r}|i\rangle &= \int \psi_f^*(\vec{r})(\hat{\epsilon} \cdot \vec{r})\psi_i(\vec{r})d^3\vec{r} \qquad (2.5) \\ &= \underbrace{\int r^3 dr R_{n_f l_f}^* R_{n_i l_i}}_{Radial\ integral} \underbrace{\int d\Omega Y_{l_f m_f}^* (\hat{\epsilon} \cdot \hat{r}) Y_{l_i m_i}}_{Angular\ integral} \underbrace{\delta(m_f^s, m_i^s)}_{Spin\ part}. \end{aligned}$$

It is obvious that spin flips are not allowed during the excitation since otherwise $\langle f|\hat{\epsilon}\cdot\vec{r}|i\rangle = 0$. Moreover, the dipole operator only operates on the angular part.

2.1.2. Sum rule analysis

Both, the absorption spectrum line-shape and the intensity are directly related to the ground state properties. In a normal XAS measurement with linearly polarized light, the sum rule analysis relates the integrated absorption intensity to the projected density of states of the initial state. The sum rule results from the intrinsic properties of the dipole operator, which are obtained only through symmetry considerations, regardless of the details of the Hamiltonian. A comprehensive derivation of the sum rules is shown in Ref. [54] based on an one-electron approximation. The derivation of sum rules for $2p \rightarrow 3d$ excitations presented below can be found in Refs. [6, 54, 70].

In electron-dipole approximation, the x-ray absorption intensity can be written

$$I_{XAS} \propto M_{if}\ {}^{2} = \langle\psi_i|\hat{\epsilon}\cdot\vec{r}|\psi_f\rangle\langle\psi_f|\hat{\epsilon}\cdot\vec{r}|\psi_i\rangle, \tag{2.6}$$

summing over all the final states, such that $\sum_f |\psi_f\rangle\langle\psi_f| = 1$, thus

$$I_{XAS} \propto \langle\psi_i|\hat{\epsilon}\cdot\vec{r}\ ||\ \hat{\epsilon}\cdot\vec{r}|\psi_i\rangle. \tag{2.7}$$

The dipole operator can be expressed in terms of spherical harmonics [120]: $(\hat{\epsilon}\cdot\hat{r}) = rC_q^{(1)}$ [1], with $q = -1, 0, +1$, denoting the polarization vector for left circular polarized light, z linear polarized light and right circular polarized light, respectively. The dipole operator for x- and y-polarized light are expressed as $r\sqrt{\frac{1}{2}}(C_{-1}^{(1)} - C_1^{(1)})$ and $r\ i\sqrt{\frac{1}{2}}(C_{-1}^{(1)} + C_1^{(1)})$, respectively.

Whether a transition is allowed or forbidden depends on the direct product of these three spherical harmonics (Eq. 2.5) and could be easily evaluated through symmetric consideration, i.e. by evaluating $< Y_{l_f}^{m_f} \mid C_q^{(1)} \mid Y_{l_i}^{m_i} >$. The parity of a state depends on the quantum number l, i.e. *parity* $= (-1)^l$, and it is clear that $C_q^{(1)}$ is odd in parity. Therefore, the other two spherical harmonics should be opposite in parity so that the integral over odd-odd-even (or even-odd-odd) terms is non-zero, which yields the following dipole selection rules:

$$\begin{aligned} \Delta l &= \pm 1 \\ \Delta m &= 0,\ \pm 1 \\ \Delta s &= 0 \\ \Delta m_s &= 0. \end{aligned} \tag{2.8}$$

In the following, we will derive the sum rules for a $2p \rightarrow 3d$ transition in the atomic limit. First, we expand the dipole operator in second quantization:

$$rC_q^{(1)} = r \sum_{m\sigma m'\sigma'} c_{m'\sigma'} l_{m\sigma}^{\dagger} \langle l_{m\sigma}|C_q^{(1)}|c_{m'\sigma'}\rangle. \tag{2.9}$$

The spectral intensity can be written as:

---

[1] Here, usually Racah's spherical tensor operator instead of the normal spherical harmonics Y_l^m is used to get rid of the pre-factor, i.e. $C_m^{(l)} = \sqrt{\frac{4\pi}{2l+1}}Y_l^m$.

$$\begin{aligned}&\langle\psi_i|r\sum_{m\sigma m'\sigma'}c_{m'\sigma'}l^{\dagger}_{m\sigma}\langle l_{m\sigma}|C^{(1)}_q|c_{m'\sigma'}\rangle|\psi_f\rangle\langle\psi_f|\\&r\sum_{m''\sigma''m'''\sigma'''}c_{m'''\sigma'''}l^{\dagger}_{m''\sigma''}\langle l_{m''\sigma''}|C^{(1)}_q|c_{m'''\sigma'''}\rangle|\psi_i\rangle.\end{aligned}\tag{2.10}$$

A separation of the radial and the angular integral part results in:

$$\begin{aligned}&|\langle R_i|r|R_f\rangle|^2\sum_{m\sigma\ldots\sigma'''}\langle\psi_i|\\&l_{m\sigma}c^{\dagger}_{m'\sigma'}c_{m'''\sigma'''}l^{\dagger}_{m''\sigma''}|\psi_i\rangle\langle l_{m\sigma}|C^{(1)}_q|c_{m'\sigma'}\rangle\langle l_{m''\sigma''}|C^{(1)}_q|c_{m'''\sigma'''}\rangle.\end{aligned}\tag{2.11}$$

For $2p\rightarrow 3d$ transitions, the $2p$ shell ($c=1$) is completely filled, therefore $c^{\dagger}_{m'\sigma'}c_{m'''\sigma'''}=\delta_{m'm'''}\delta_{\sigma'\sigma'''}$, as a result: $m'=m'''$, $\sigma'=\sigma'''=\sigma''$ (the dipole moment is not σ dependent). The spectrum intensity can be further written as:

$$I_q=|\langle R_i|r|R_f\rangle|^2\sum_{m\ldots m''\sigma}l_{m\sigma}l^{\dagger}_{m''\sigma}\langle l_{m\sigma}|C^{(1)}_q|c_{m'\sigma}\rangle\langle l_{m''\sigma}|C^{(1)}_q|c_{m'\sigma}\rangle.\tag{2.12}$$

The Wigner-Eckart theorem relates the matrix element to the coupling coefficients which can be replaced by a $3J$-symbol as:

$$\langle l_m|C^{(k)}_q|c_{m'}\rangle=(-1)^m\sqrt{(2l+1)(2c+1)}\begin{pmatrix}l&k&c\\0&0&0\end{pmatrix}\begin{pmatrix}l&k&c\\-m&q&m'\end{pmatrix}.$$

A physically reasonable $3J$ symbol should satisfy: $-m+q+m'=0$, i.e. $m=q+m'$. Similarly for the second $3J$-symbol, it requires: $m''=q+m'$. Now let us specify the absorption intensity with $c=l$ - 1 (dipole allowed):

$$\begin{aligned}I_q&=|\langle R_i|r|R_f\rangle|^2\sum_{m\sigma m''\sigma}(-1)^{m+m''}(2l+1)(2c+1)l_{m\sigma}l^{\dagger}_{m''\sigma}\\&\begin{pmatrix}l&1&c\\0&0&0\end{pmatrix}\begin{pmatrix}l&1&c\\-m&q&m'\end{pmatrix}\begin{pmatrix}l&1&c\\0&0&0\end{pmatrix}\begin{pmatrix}l&1&c\\-m''&q&m'\end{pmatrix}\\&=|\langle R_i|r|R_f\rangle|^2\sum_{m\sigma}(2l+1)(2l-1)\underline{n}_{m\sigma}(\begin{pmatrix}l&1&l-1\\0&0&0\end{pmatrix}\begin{pmatrix}l&1&l-1\\-m&q&m-q\end{pmatrix})^2,\end{aligned}\tag{2.13}$$

with $\underline{n}_{m\sigma} = l_{m\sigma} l^{\dagger}_{m\sigma}$.

By setting all l- and c-dependent prefactors to A^2_{cl}, we obtain the absorption intensity for $q =$-1, 0, and +1 as follows:

$$\begin{aligned}
I_{-1} &= A^2_{cl} \sum_{m,\sigma} \underline{n}_{m\sigma} \frac{(l-m)(l-m-1)}{2l(2l+1)(2l-1)} \\
I_{0} &= A^2_{cl} \sum_{m,\sigma} \underline{n}_{m\sigma} \frac{(l-m)(l+m)}{l(2l+1)(2l-1)} \\
I_{+1} &= A^2_{cl} \sum_{m,\sigma} \underline{n}_{m\sigma} \frac{(l+m)(l+m-1)}{2l(2l+1)(2l-1)}.
\end{aligned} \tag{2.14}$$

Next we can derive the spectral intensity for x- and y-polarized light. Replacing the dipole operator for x- and y-polarized light, the intensity reads:

$$\begin{aligned}
I_x =& |\langle R_i | r | R_f \rangle|^2 \sum_{m \ldots m'' \sigma} l_{m\sigma} l^{\dagger}_{m''\sigma} \\
& \langle l_{m\sigma} | \sqrt{\frac{1}{2}} (C^{(1)}_{-1} - C^{(1)}_{1}) | c_{m'\sigma} \rangle \langle l_{m''\sigma} | \sqrt{\frac{1}{2}} (C^{(1)}_{-1} - C^{(1)}_{1}) | c_{m'\sigma} \rangle,
\end{aligned} \tag{2.15}$$

then:

$$\begin{aligned}
I_x =& \frac{1}{2}(I_{-1} + I_{+1}) - \frac{1}{2} A^2_{cl} \sum_{m\sigma m''\sigma} (-1)^{m+m''} l_{m\sigma} l^{\dagger}_{m''\sigma} \\
& (\begin{pmatrix} l & 1 & c \\ -m & -1 & m' \end{pmatrix} \begin{pmatrix} l & 1 & c \\ -m'' & 1 & m' \end{pmatrix} + \\
& \begin{pmatrix} l & 1 & c \\ -m & 1 & m' \end{pmatrix} \begin{pmatrix} l & 1 & c \\ -m'' & -1 & m' \end{pmatrix}) \\
=& \frac{1}{2}(I_{-1} + I_{+1}) - \frac{1}{2} A^2_{cl} \sum_{m\sigma m''\sigma} (-1)^{m+m''} l_{m\sigma} l^{\dagger}_{m''\sigma} \\
& (\begin{pmatrix} l & 1 & l-1 \\ -m & -1 & m+1 \end{pmatrix} \begin{pmatrix} l & 1 & l-1 \\ -m-2 & 1 & m+1 \end{pmatrix} + \\
& \begin{pmatrix} l & 1 & l-1 \\ -m & 1 & m-1 \end{pmatrix} \begin{pmatrix} l & 1 & l-1 \\ -m+2 & -1 & m-1 \end{pmatrix}).
\end{aligned} \tag{2.16}$$

Note that for non-vanishing angular momentum dipole matrix elements, the first $3J$ symbol should satisfy: $m' = 1 + m$, $m'' = 1 + m' = 2 + m$; and it implies: $m' = -1 + m$, $m'' = -1 + m' = -2 + m$ for the second $3J$ symbol. Thus for $c = l$ - 1 dipole transition, I_x can be written as:

$$I_x = \frac{1}{2}(I_{-1} + I_1) - A_{cl}^2 \frac{1}{2} \sum_{m,\sigma} \frac{\sqrt{l-m-1}\sqrt{l-m}\sqrt{l+m+1}\sqrt{l+m+2}}{2l(2l-1)(2l+1)} (l_{m+2\sigma} l_{m\sigma}^\dagger + l_{m\sigma} l_{m+2\sigma}^\dagger); \tag{2.17}$$

Similarly, we can calculate the absorption intensity for I_y:

$$I_y = \frac{1}{2}(I_{-1} + I_1) + A_{cl}^2 \frac{1}{2} \sum_{m,\sigma} \frac{\sqrt{l-m-1}\sqrt{l-m}\sqrt{l+m+1}\sqrt{l+m+2}}{2l(2l-1)(2l+1)} (l_{m+2\sigma} l_{m\sigma}^\dagger + l_{m\sigma} l_{m+2\sigma}^\dagger). \tag{2.18}$$

The $3d$ orbitals could be expressed in terms of spherical harmonics as follows:

$$\begin{aligned} 3d_{x^2-y^2} &= \tfrac{1}{\sqrt{2}}(Y_2^2 + Y_2^{\bar{2}}) \\ 3d_{3z^2-r^2} &= Y_2^0 \\ 3d_{xy} &= -\tfrac{i}{\sqrt{2}}(Y_2^2 - Y_2^{\bar{2}}) \\ 3d_{yz} &= -\tfrac{i}{\sqrt{2}}(Y_2^1 + Y_2^{\bar{1}}) \\ 3d_{xz} &= \tfrac{1}{\sqrt{2}}(Y_2^1 - Y_2^{\bar{1}}). \end{aligned} \tag{2.19}$$

To derive the absorption intensity for I_z, only transition including $d_{3z^2-r^2}$, d_{xz}, and d_{yz} orbitals are symmetrically allowed and contribute. Furthermore, we know:

$$\begin{aligned} \underline{n}_{3z^2-r^2} &= d_{3z^2-r^2} d_{3z^2-r^2}^\dagger \\ \underline{n}_{xz} &= d_{xz} d_{xz}^\dagger = \frac{1}{2}(\underline{n}_{-1} + \underline{n}_1) - \frac{1}{2}(d_{-1} d_1^\dagger + d_1 d_{-1}^\dagger) \\ \underline{n}_{yz} &= d_{yz} d_{yz}^\dagger = \frac{1}{2}(\underline{n}_{-1} + \underline{n}_1) + \frac{1}{2}(d_{-1} d_1^\dagger + d_1 d_{-1}^\dagger). \end{aligned}$$

Taking into account the transition probability (pre-factors of the $3J$-symbol calculation in Eqs. 2.14- 2.18) for each transition, one can easily obtain the

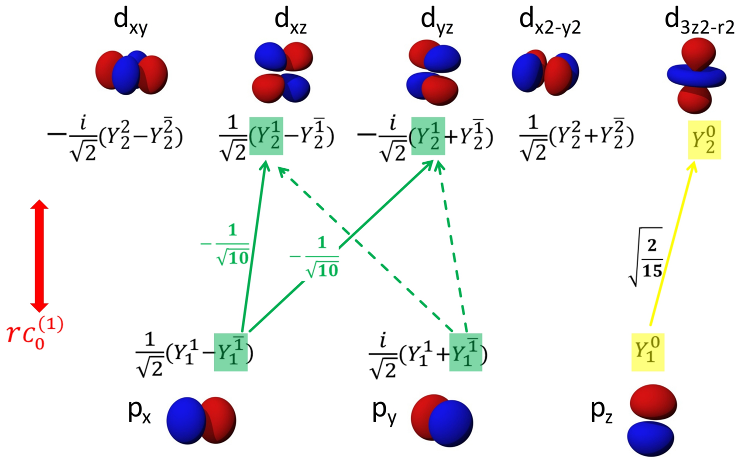

Figure 2.2.: Schematic presentation of excitations from the $2p$ core level (p_x, p_y, p_z orbitals) to the unoccupied $3d$ band (d_{xy}, d_{xz}, d_{yz}, $d_{x^2-y^2}$ and $d_{3z^2-r^2}$ orbitals) with linear z-polarized light ($q=0$). All orbitals are expressed in terms of spherical harmonics. The allowed dipole excitations are marked by lines. The value written next to each transition corresponds to the expectation value of the $3J$-symbols considering only the symmetry.

sum rules as follows:

$$\begin{aligned}
I_x &= \frac{1}{\underline{n}}(\frac{1}{2}\underline{n}_{xy} + \frac{1}{2}\underline{n}_{yz} + \frac{1}{6}\underline{n}_{z^2} + \frac{1}{2}\underline{n}_{x^2-y^2} - \sqrt{\frac{1}{12}}(d_{z^2}d^\dagger_{x^2+y^2} + d^\dagger_{z^2}d_{x^2+y^2})) \\
I_y &= \frac{1}{\underline{n}}(\frac{1}{2}\underline{n}_{xy} + \frac{1}{2}\underline{n}_{yz} + \frac{1}{6}\underline{n}_{z^2} + \frac{1}{2}\underline{n}_{x^2-y^2} + \sqrt{\frac{1}{12}}(d_{z^2}d^\dagger_{x^2+y^2} + d^\dagger_{z^2}d_{x^2+y^2})) \\
I_z &= \frac{1}{\underline{n}}(\frac{1}{2}\underline{n}_{xz} + \frac{1}{2}\underline{n}_{yz} + \frac{2}{3}\underline{n}_{z^2}). \qquad (2.20)
\end{aligned}$$

Fig. 2.2 and Fig. 2.3 show an illustration of the transition from the $2p$ core level to the unoccupied $3d$ states, with z-polarized light and left circular polarized light, respectively. In each plot, we show the allowed dipole excitations as well as the expectation values of the $3J$-symbols. Note that the square of the expectation values multiplied by the relative weight of each orbital ex-

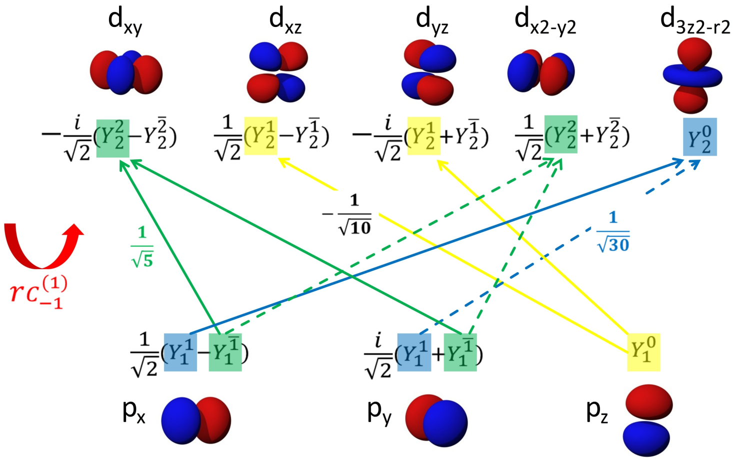

Figure 2.3.: Dipole allowed transitions from the $2p$ core level to the unoccupied $3d$ states with left circular polarized light ($q=$-1). The value written next to each transition is the expectation value of the Matrix element which is calculated by evaluating the $3J$-symbols with purely symmetry considerations. The square of the expectation values multiplied by the relative weight for each orbital results from the different pre-factors in Eq. 2.20. The orbitals shown in Fig. 2.2 and Fig. 2.3 are adopted from wikipedia website.

actly represents the different pre-factors in Eq. 2.20. For instance, the relative spectral intensity of I_z is given by:

$$n_{xz} : n_{yz} : n_{z^2} = 2*(\frac{1}{\sqrt{2}})^2*(-\frac{1}{\sqrt{10}})^2 : 2*(\frac{1}{\sqrt{2}})^2*(-\frac{1}{\sqrt{10}})^2 : (\sqrt{\frac{2}{15}})^2 = \frac{1}{2} : \frac{1}{2} : \frac{2}{3}.$$

Particularly for a Ni^{3+} ion ($3d^7$: $t_{2g}^6 e_g^1$) with crystal symmetry higher than orthorhombic: $\underline{n}_{xy} = \underline{n}_{xz} = \underline{n}_{yz} = 0$. Neglecting the interference terms results in:

$$\begin{aligned} I_x &= I_y = \frac{1}{6}\underline{n}_{z^2} + \frac{1}{2}\underline{n}_{x^2-y^2} \\ I_z &= \frac{2}{3}\underline{n}_{z^2}. \end{aligned} \tag{2.21}$$

It is obvious that XAS measurements with incident light perpendicular and parallel with respect to the scattering plane reflect directly the hole occupations with $d_{x^2-y^2}$ and $d_{3z^2-r^2}$ symmetry.

2.1.3. Absorption intensity from optical theorem

The interaction of light with matter can be treated by an optical response approach, where atoms are modeled by classical dipole oscillators with characteristic resonant frequency ω. The small displacement vector (or the polarization vector) of the electron $\vec{P}$ in response to a time dependent incident EM wave $\vec{E}_{in}$ is linear and can be expressed as:

$$\vec{P} = \chi \, \vec{E}_{in}, \tag{2.22}$$

where $\vec{E}_{in}$ is the electric field of the incoming beam (with the same expression as Eq. 2.2) and χ denotes the electric susceptibility of the electron. The current density can then be written:

$$\vec{j} = \frac{\partial \, \vec{P}}{\partial \, t} = -\omega\chi\vec{E}_{in}. \tag{2.23}$$

The current density $\vec{j}$ arises due to the conduction electrons and can be related to the conductivity σ, i.e. $\vec{j} = \sigma \, \vec{E}_{in}$. It is obvious that: $\sigma = -\omega \, \chi$.

The final x-ray absorption intensity can be simply expressed in term of conductivity as follows:

$$I_{XAS} \propto \mathrm{I_m} \, [\hat{\varepsilon}^* \ \cdot \sigma \cdot \ \hat{\varepsilon}]. \tag{2.24}$$

Note that the conductivity σ is a second rank tensor which will be discussed in detail in the following.

2.2. X-ray scattering

To illustrate a scattering process one can imagine that the incoming x-rays force the electrons of a material to vibrate, and the oscillating electrons act as a dipole source and radiate an EM field. The simplest scattering process would be the scattering of x-rays by one electron, where the scattering ability of an electron is called the Thomson scattering length, which is given by the classical electron radius with $r_0 = 2.82 \times 10^{-5}$ Å. Since its value is smaller than the typical lattice spacing, multiple scattering is negligible. Considering the scattering ability of x-rays by one atom consisting of Z electrons (where Z is the atomic number associated with electron density distribution $\rho(\vec{r})$) we have to take into account the atomic form factor $f^0(\vec{Q})$. Mathematically, the radiated strength of an atom is the superposition of all electrons, the total atomic scattering length is $-r_0 f^0(\vec{Q})$ with $\vec{Q}$ being the momentum transfer. The atomic form factor $f^0(\vec{Q})$ reads:

$$\begin{aligned} f^0(\vec{Q}) &= \int \rho(\vec{r}) e^{i\vec{Q}\vec{r}} d\vec{r} \\ &= \begin{cases} Z & for\ Q \rightarrow 0 \\ 0 & for\ Q \rightarrow \infty. \end{cases} \end{aligned} \tag{2.25}$$

For a general scattering problem, the atomic form factor is a complex quantity which is both energy $\hbar\omega$ and momentum $\hbar\vec{Q}$ dependent:

$$f^0(\vec{Q}, \hbar\omega) = f^0(\vec{Q}) + f'(\hbar\omega) + if''(\hbar\omega), \tag{2.26}$$

where $f'(\hbar\omega)$ and $f''(\hbar\omega)$ account for the resonant part (dispersion), and are related directly to the reflection index in a material as will be discussed in the next section. The resonant process, namely when the photon incident energy corresponds to the absorption edge of a particular element, has the advantage in probing small density modulations such as the charge, orbital and magnetic orderings in solid state research due to the large enhancement of the scattering cross section. The momentum dependent part $f^0(\vec{Q})$ plays a role in the structure determination of solids, normally performed at fixed wavelengths, e.g. at Cu and Mo K_α energies.

X-ray scattering is a photon-in photon-out process as illustrated in Fig. 2.4. The scattering intensity for a scattering process can be written as:

$$I_{scat} = |\sum_i \ \exp(i\ (\vec{k}_{in} - \vec{k}_{out})\ \vec{R}_i)\ \epsilon^*_{out}\ f_i\ \epsilon_{in}|^2, \tag{2.27}$$

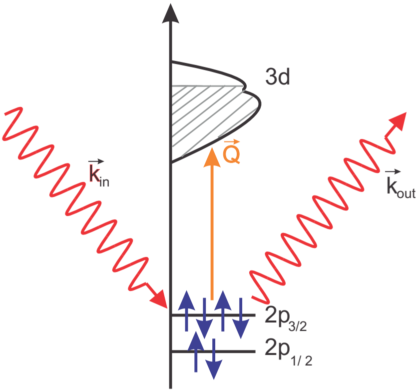

Figure 2.4: A simple illustration of x-ray scattering as a photon-in photon-out process for $2p \rightarrow 3d$ excitations. $\vec{Q}$ denotes the momentum transfer during the scattering process, i.e. $\hbar\vec{Q} = \hbar\vec{k}_{out} - \hbar\vec{k}_{in}$.

where $\vec{k}_{in}$ and $\vec{k}_{out}$ denote the incoming and the outgoing wave vector, ϵ_{in} and ϵ_{out} represent the polarization of the incoming and outgoing light, respectively. The total scattering intensity is sensitive to the momentum transfer $\vec{Q}$ during the scattering process: $\hbar\vec{Q} = \hbar\vec{k}_{out} - \hbar\vec{k}_{in}$. f_i denotes the scattering factor at site i. Furthermore, the total scattering factor sums up different atomic positions $\vec{R}_i$ with a phase factor, i.e. $F(Q) = \sum_i f_i \exp(i\vec{Q}\vec{R}_i)$. From the optical theorem, the scattering factor is related to the conductivity σ (or the dielectric tensor ϵ) through:

$$F = -\,\omega\,\sigma, \tag{2.28}$$

with σ as a second rank tensor:

$$\sigma = \begin{pmatrix} \sigma_{xx} & \sigma_{xy} & \sigma_{xz} \\ \sigma_{yx} & \sigma_{yy} & \sigma_{yz} \\ \sigma_{zx} & \sigma_{zy} & \sigma_{zz} \end{pmatrix}. \tag{2.29}$$

In general, the response or induced vectors (properties) of a material to an external/applied vector can be expressed by a tensor of second rank, such as the heat flow density in response to an applied temperature gradient is linked by the thermal conductivity, or the dielectric displacement which is related to the applied electric field through the permittivity, or the magnetic induction which is related to an external magnetic field by the permeability, etc. Similarly here, the electron is correlated to the incoming electromagnetic wave through the conductivity tensor σ. Moreover, the symmetry of physical properties (σ, ϵ, etc.) is related to the symmetry of the crystal known as the

Neumann's Principles, which state [105]:

The symmetry elements of any physical property of a crystal must include the symmetry elements of the point group of the crystal.

Taking into account the crystal symmetry for a non-magnetic crystal, the conductivity tensors are as follows, representing cubic, tetragonal (hexagonal, trigonal), orthorhombic and monoclinic crystal symmetry (e.g. $\sigma_{xy} = \sigma_{yx}$), respectively.

$$\sigma_{cub} = \begin{pmatrix} \sigma_{xx} & 0 & 0 \\ 0 & \sigma_{xx} & 0 \\ 0 & 0 & \sigma_{xx} \end{pmatrix} \qquad \sigma_{tetra} = \begin{pmatrix} \sigma_{xx} & 0 & 0 \\ 0 & \sigma_{xx} & 0 \\ 0 & 0 & \sigma_{zz} \end{pmatrix}$$

$$\sigma_{orth} = \begin{pmatrix} \sigma_{xx} & 0 & 0 \\ 0 & \sigma_{yy} & 0 \\ 0 & 0 & \sigma_{zz} \end{pmatrix} \qquad \sigma_{mono} = \begin{pmatrix} \sigma_{xx} & \sigma_{xy} & 0 \\ \sigma_{yx} & \sigma_{yy} & 0 \\ 0 & 0 & \sigma_{zz} \end{pmatrix}.$$

Triclinic as the lowest symmetry has basically the same form as Eq. 2.29, but it preserves the symmetrical properties, i.e. $\sigma_{ij} = \sigma_{ji}$ (i, j = x, y, z).

The conductivity tensor of a magnetic material with a local moment along the z-axis is given by:

$$\sigma = \begin{pmatrix} \sigma_{xx} & \sigma_{xy} & 0 \\ -\sigma_{xy} & \sigma_{yy} & 0 \\ 0 & 0 & \sigma_{zz} \end{pmatrix},$$

with $\sigma_{yx} = -\sigma_{xy}$ [56].

A general polarization dependent scattering problem can be easily visualized and understood from the scattering tensor. For instance, in a resonant magnetic diffraction process, a magnetic scattering tensor with off-diagonal components must be considered. Details of the ground state magnetic structure can be obtained from the polarization and the azimuthal dependence of the scattered intensity [33, 123]. In terms of the charge modulation in layered heterostructures considered throughout this thesis, we take into account the conductivity tensor σ with tetragonal symmetry which has been first proposed in Ref. [8], the idea of which is explained hereafter.

Let us consider a layered structure, which either can be atomic planes of a crystal or different layers in a heterostructure, neglecting the multiple scattering, the x-ray scattering intensity along the specular direction is directly related to the total scattering factor F_{q_z}, which is a superposition of scatter-

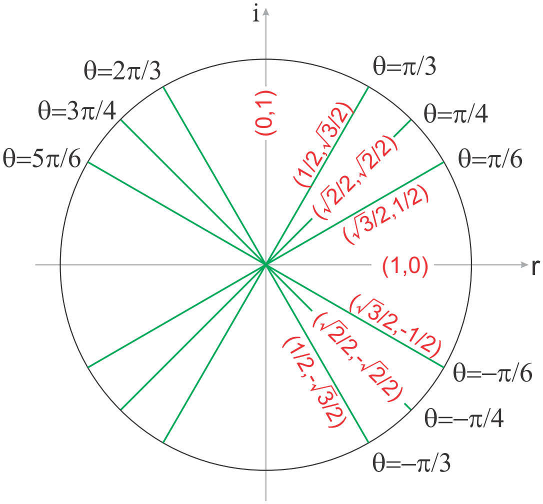

Figure 2.5.: Visual picture to calculate $\exp(i\theta)$ for some frequently used angles in a unit circle. The horizontal and the vertical axis denote the real and the imaginary part of a complex number.

ing factors of the individual layers with a phase factor:

$$F_{q_z} = \sum_i f_i e^{iq_z z}, \tag{2.30}$$

where f_i denotes the atomic form factor of layer i, q_z is the momentum transfer during the scattering process and z is the thickness of layer i.

The phase factor can be expressed by trigonometric functions using Euler's formula, i.e. $\exp(i\theta) = \cos\theta + i\sin\theta$, which can be easily calculated with the help of a unit circle (Fig 2.5).

We performed our x-ray scattering experiments at fixed momentum transfer q_z, i.e. a fixed phase factor for each individual layer in Eq. 2.30, from which the total scattering factor can be obtained. Fig. 2.6 shows the relative weight of phase factors for different layers with fixed q_z around the $SL(001)$ reflection and $SL(002)$ reflection for a superlattice configuration of 4 u.c. LNO and 4 u.c. LAO. Note that the specular momentum is written in terms of the Miller index L, i.e. $q_z = 2\pi\ L/c$, with c denoting the superlattice bilayer period. L reflects the modulation from the superlattice period, e.g. the $SL(001)$ and $SL(002)$

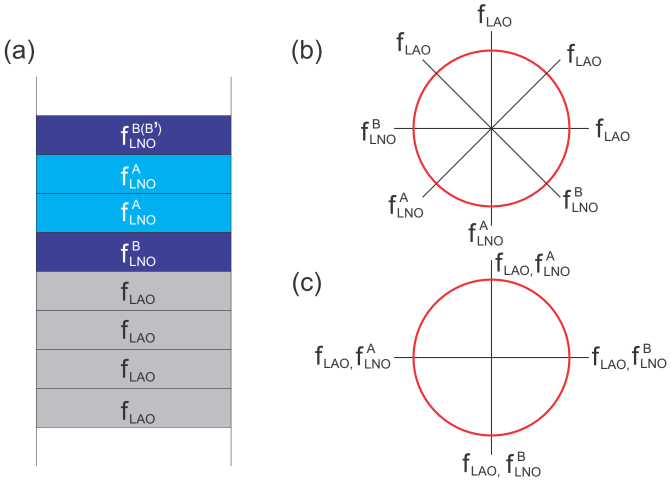

Figure 2.6.: Illustration of a fixed q_z reflectivity measurement in a LNO-LAO (4 u.c.//4 u.c.) superlattice. (a) A sketch of the layer structure with 4 u.c. LAO (with the scattering factor f_{LAO}) and 4 u.c. LNO (f^B_{LNO} and f^A_{LNO} denote the scattering factor of the interfacial layer and the inner layer, respectively.); (b),(c) show the relative weight of the phase factor for $q_z = SL(001)$ and $q_z = SL(002)$, respectively.

correspond to the reflection with the period of the superlattice and half of the bilayer period, respectively (as shown in Fig. 2.6). The total scattering factors $F_{(001)}$ and $F_{(002)}$ read:

$$\begin{aligned} F_{(001)} &= \sum_i f_i \ \exp(iq_z \ z) \\ &= f_{LAO} + (\frac{\sqrt{2}}{2} + \frac{\sqrt{2}}{2}i)f_{LAO} + if_{LAO} + (-\frac{\sqrt{2}}{2} + \frac{\sqrt{2}}{2}i)f_{LAO} \\ &- f^B_{LNO} - (\frac{\sqrt{2}}{2} + \frac{\sqrt{2}}{2}i)f^A_{LNO} - if^A_{LNO} + (\frac{\sqrt{2}}{2} - \frac{\sqrt{2}}{2}i)f^B_{LNO} \\ &= (1 - \frac{\sqrt{2}}{2} + \frac{\sqrt{2}}{2}i)(f_{LAO} - f^B_{LNO}) + (i + \frac{\sqrt{2}}{2} + \frac{\sqrt{2}}{2}i)(f_{LAO} - f^A_{LNO}); \end{aligned} \tag{2.31}$$

$$\begin{aligned} F_{(002)} &= \sum_i f_i \; \exp(iq_z \; z) \\ &= f_{LAO} + if_{LAO} - f_{LAO} - if_{LAO} + f^B_{LNO} + if^A_{LNO} - f^A_{LNO} - if^B_{LNO} \\ &= (1-i)(f^B_{LNO} - f^A_{LNO}). \end{aligned} \tag{2.32}$$

It is obvious that the intensity of the $SL(002)$ superlattice reflection is determined by the difference of the scattering factors of the outer and the inner layers (i.e. $F_{(002)} \propto (f^B_{LNO} - f^A_{LNO})$). We will show later that a polarization-dependent analysis of the scattering intensity allows a map of layer-resolved charge profiles inside the 4 u.c. layer stacks.

2.3. Simulation of the x-ray reflectivity intensity

Resonant x-ray reflectivity is a well-known method for exploring detailed structural information of multilayers or thin films such as the individual layer thickness, roughness and the electronic density. However, one cannot get direct information about the structural properties due to the loss of phase information in intensity measurements. Here, we use the program REMAGX to simulate the resonant x-ray reflectivity curves based on either the Paratt's recursive or the matrix formulism. Prior to the simulation, the knowledge of appropriate optical constant of each layer in the system is crucial. Theoretical values of the form factors can be found in the Henke or the Chantler table [21, 59]. For instance, the Chantler table shows the real and imaginary part of the form factor (f_1 and f_2) for all elements (up to Uranium, $Z=92$) from $10\,eV$ to $400\,keV$ [21]. The photoelectric absorption cross section is obtained from self-consistent Dirac-Hartree-Fock calculations for isolated atoms taking into account only the spin-orbit coupling, which is in good agreement with experimental results at non-resonant energies. At absorption edges, the fine structure is important which changes the scattering form factor dramatically. In our data analysis, a proper optical constant is obtained by merging the experimentally measured absorption spectrum near resonant energies to the theoretical values from the Chantler table.

From the optical theorem, we know that the x-ray absorption cross section is proportional to the imaginary part of the scattering factor f_2 through:

$$f_2 = -\frac{\sigma_a}{2r_0\lambda}, \tag{2.33}$$

where σ_a, r_0 and λ denote the absorption cross section, the classic electron radius and the wavelength of the incoming photon, respectively.

Thus, the imaginary part f_2 can be derived from the atomic photo-absorption cross section. The real part of the atomic scattering factor f_1 is related to the imaginary part f_2 by the Kramers-Kronig dispersion relation (for details see Appendix. A).

The data processing to obtain the optical constant is performed as follows:

First, we create the theoretical atomic form factor for a compound by taking the sum of the scattering factor of all individual atoms times the relative number of each type of atom in the compound. For instance, the theoretical atomic form factor for LNO (f_{LNO}) is obtained through:

$$f_{LNO} = 1 * f_{La} + 1 * f_{Ni} + 3 * f_O. \tag{2.34}$$

The energy spectrum of the imaginary part f_2 close to the Ni L-edges are shown in Fig. 2.7(a), with La M_5 and M_4 edges nearby (i.e. four resonant energies in total).

Then, we merge the experimental XAS spectrum to the Chantler table. We notice that the imaginary part of the scattering factor shows a linear decay of the scattering intensity above resonant edges, which is due to the damping term for the semiclassical treatment of the electron-photon interactions as classical harmonic oscillators. Thus, we fit the background prior to the resonant edges with a linear function in the form of $y = b - k * E(\hbar\omega)$, where b and k corresponds to the offset as well as the slope of the linear background (Fig. 2.7(b)). The edge jump is denoted by h. Next, we merge the experimental $XAS*E(\hbar\omega)$ spectrum to the Chantler table which captures the edge jump, i.e. the characteristic atomic transition of core electrons (Fig. 2.7(c)). One can do this by simply multiplying the edge jump h, followed by adding the linear fitting of the background line to the normalized $XAS * E(\hbar\omega)$ curve. [2] Finally the real part of the scattering factor f_1 is obtained through a Kramers-Kronig transformation.

In the last step, we obtain the optical constants δ and β. The real and the imaginary parts of the refraction index $n = 1 - \delta + i\beta$ are related to the real and the imaginary parts of the atomic form factor as follows:

$$\begin{aligned} \delta(E) &= \frac{2\pi\rho r_0 (c\hbar)^2}{E^2}(Z^* + f_1(E)) \\ \beta(E) &= \frac{2\pi\rho r_0 (c\hbar)^2}{E^2}(f_2(E)), \end{aligned} \tag{2.35}$$

where $r_0 = 2.8179\times\ 10^{-15}\,m$ represents the classical electron radius, ρ denotes the mass density in the unit of mass/volume, $c = 2.998\times10^8\,m/s$ is the light velocity, $\hbar = 6.582\times10^{-16}\,eV \cdot s$ is the Planck constant and Z^* is the atomic number after a relativistic correction: $Z^* = Z - (Z/82.5)^{2.37}$. $E = \hbar\omega$ is the x-ray energy.

Having the proper optical constants at hand, we are ready for the simulation of the reflectivity curves. As mentioned before, two methods, the Parratt's recursive and the matrix formulism have been used to calculate the reflectivity intensity. Parratt's recursive method is based on the dynamical approach [108], taking into account multiple scattering effects. The idea for the Parratt's recursive simulation is summarized as below, following Refs. [68, 108, 109].

---

[2] The normalized $XAS * E(\hbar\omega)$ curve is defined as the absorption line after subtracting a linear background followed by scaling the continuum edge to one (e.g. $E = 880\,eV$ for LNO-based superlattices).

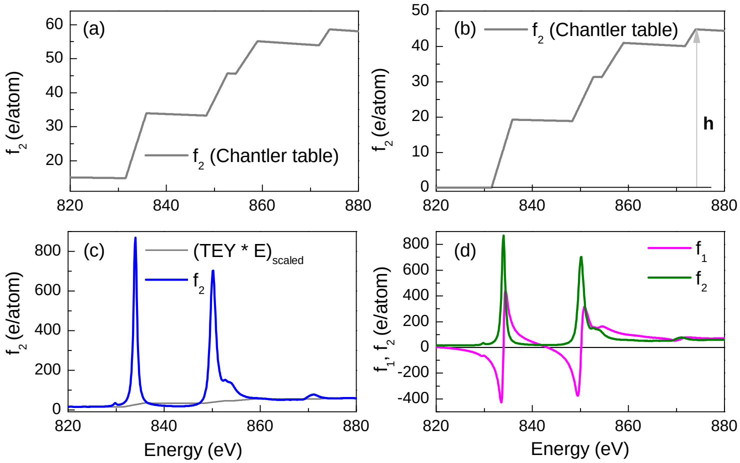

Figure 2.7.: (a) The imaginary part of the scattering factor f_2 of LNO obtained from the Chantler table. (b) Scattering factor f_2 after subtracting a linear line ($y = 34.4521 - 0.02329 * E$), which shows a step height $h = 44.785$. (c) In the last step the normalized $(XAS * E(\hbar\omega))$ spectrum is merged to the Chantler data and multiplied by the edge jump. (d) The real part f_1 is obtained from f_2 through a Kramers-Kronig transformation.

The total reflectivity amplitude $r_{j-1,j}$ between the neighboring $(j-1)$ and j layers taking into account the multiple reflections can be expressed as:

$$\begin{aligned} r_{j-1,j} &= r'_{j-1,j} + t'_{j-1,j} r'_{j,j+1} t'_{j,j-1} (e^{iz_j q_j})^2 + t'_{j-1,j} (r'_{j,j+1})^2 t'_{j,j-1} r'_{j,j-1} (e^{iz_j q_j})^4 + \dots \\ &= r'_{j-1,j} + t'_{j-1,j} r'_{j,j+1} t'_{j,j-1} (e^{iz_j q_j})^2 \sum_{m=0}^{\infty} (r'_{j,j-1} r'_{j,j+1} (e^{iz_j q_j})^2)^m . \end{aligned}$$

The summation is a geometric series, and similar to the phase factor summation. $r_{j-1,j}$ can thus be rewritten as:

$$r_{j-1,j} = \frac{r'_{j-1,j} + r_{j,j+1}\ e^{iz_j q_j}}{1 + r'_{j-1,j} r_{j,j+1}\ e^{iz_j q_j}}, \tag{2.36}$$

where $e^{iz_j q_j}$ accounts for the phase shift of the beam reflected from $(j-1,\ j)$

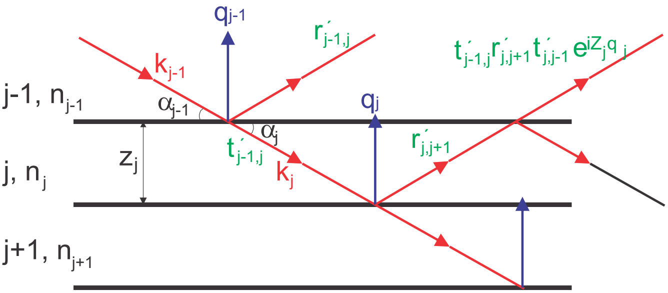

Figure 2.8.: Illustration of the recursive approach to calculate the reflection amplitude at an arbitrary $(j-1,\ j)$ interface. n_{j-1}, n_j and n_{j+1} represent the refraction index of $(j-1)$, j and $(j+1)$ layer, respectively. The total reflectivity amplitude $r_{j-1,j}$ takes into account the multiple reflections, $r'_{j-1,j}$ is the direct reflection amplitude from the Fresnel equation. The second reflection arises from the transmitted beam at the $(j-1,\ j)$ interface with transmission amplitude $t'_{j-1,j}$, is reflected at $(j,\ j+1)$ interface with $r'_{j,j+1}$, then again transmit at $(j,\ j-1)$ interface with $t'_{j,j-1}$, resulting in a reflectivity amplitude $(t'_{j-1,j}r'_{j,j+1}t'_{j,j-1}e^{iz_jq_j})$ with $e^{iz_jq_j}$ denoting the phase shift of a layer with thickness Z_j. The direct reflectivity amplitude $r'_{j-1,j}$ and the transmission amplitude $t'_{j-1,j}$ are related to the wave vector transfer q_{j-1} and q_j as mentioned in the main text.

and $(j,\ j+1)$ interfaces, z_j is the thickness of layer j and q_j is the wave vector transfer as illustrated in Fig. 2.8. $r'_{j-1,j}$ denotes the Fresnel coefficient without multiple reflection which is related to the wave vector transfer between layer $(j-1)$ and layer j through:

$$r'_{j-1,j} = \frac{q_{j-1} - q_j}{q_{j-1} + q_j}. \tag{2.37}$$

The wave vector transfer $q_j = 2k_j \sin(\alpha_j)$ is further related to the reflection index n_j through:

$$\alpha_j = 2\pi\sqrt{n_j^2 - 1 + \sin\ \alpha}, \tag{2.38}$$

with α denotes the incident angle of the x-rays at the vacuum-sample interface.

The Eq.2.36 could be solved numerically by assuming that the substrate is infinitely thick, so that there is no reflection from the substrate surface. The reflectivity amplitude between the last layer N and the substrate can be expressed as:

$$r_{N,\infty} = r'_{N,\infty} = \frac{q_N - q_\infty}{q_N + q_\infty}. \tag{2.39}$$

Note that the Fresnel equation is polarization dependent. Instead of using Cartesian coordinates, σ and π are used, defining a coordinate perpendicular (σ or s) and parallel (π or p) to the scattering plane. A sketch of the geometry is shown in Fig. 2.17. The reflectivity amplitude r' and the transmission amplitude t' for σ polarization and π polarization are summarized as follows:

$$\begin{aligned} r'^{,\sigma}_{j-1,j} &= \frac{q_{j-1} - q_j}{q_{j-1} + q_j} \\ t'^{,\sigma}_{j-1,j} &= \frac{2q_{j-1}}{q_{j-1} + q_j} \\ r'^{,\pi}_{j-1,j} &= \frac{n_j^2\, q_{j-1} - n_{j-1}^2 q_j}{n_j^2\, q_{j-1} + n_{j-1}^2 q_j} \\ t'^{,\pi}_{j-1,j} &= \frac{2n_j^2\, q_{j-1}}{n_j^2\, q_{j-1} - n_{j-1}^2 q_j}. \end{aligned} \tag{2.40}$$

The difference due to different polarization is small except around the Brewster's angle, where $r^\pi = 0$, because there is no intensity reflected parallel to the electric dipole direction.

Fig. 2.9 shows the simulated reflectivity curve with $I = |r|^2$. The q_z dependent reflectivity curve corresponds to a Co/Cu multilayer with a thickness of 10Å/60Å and a repetition of 6 times. The distance between the main peaks can be used to estimate the bilayer thickness. The simulation is done at a photon energy of $777eV$ assuming a perfect surface and no roughness at the interfaces.

The reflectivity of a rough interface can be calculated by the Nevot-Croce method [104] which is given by:

$$r'^{,grad}_{j-1,j} = r'_{j-1,j}\; e^{-2k_{j-1}k_j\gamma^2}, \tag{2.41}$$

where γ is the roughness of the interface between layer $(j-1)$ and layer j, assuming that the roughnesses are small compared to the thicknesses. For roughnesses that follow a Gaussian distribution, the change of the optical constants is given by an error function like profile. Note that it is impossible to

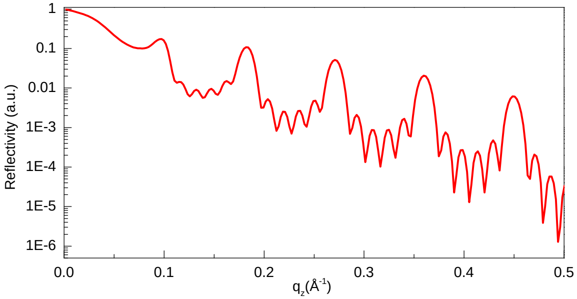

Figure 2.9.: A characteristic reflectivity simulation curve using the Parratt's recursive method for a Co/Cu multilayer with a thickness (10Å/60Å) and a repetition of 6 times. The simulation curve is calculated at a photon energy of 777 eV (Co L_3 edge).

describe materials with non-cubic scattering factor in the Parratt's formulism, i.e. the scattering factor is a scalar.

A further polarization dependent scattering intensity is obtained via the matrix formulism taking into account the tensor nature of the dielectric constant

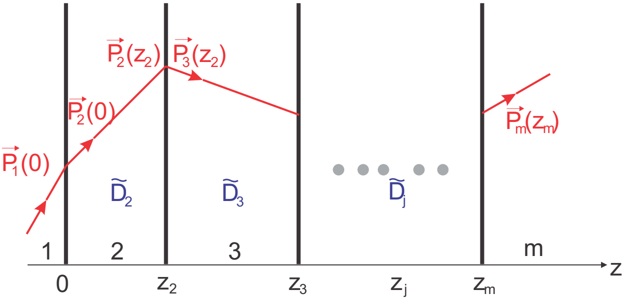

Figure 2.10.: Illustration the matrix formulism. $\vec{P}_j(z_{j-1})$ and $\widetilde{D_j}$ denote the wave propagation vector at the position z_{j-1} and the propagation matrix of a medium j, respectively. The final outgoing propagating vector $\vec{P}_m(z_m)$ is related to the incoming vector $\vec{P}_1(0)$ through a series of matrix products of each individual layer.

[150, 151]. The main idea is that the incoming light vector is related to the outgoing light vector via matrices, which are built up by the matrix products of all individual matrix elements. To understand the propagation of the field vectors inside a medium, two matrices have to be defined, i.e. the medium boundary matrix **A** and the medium propagation matrix $\widetilde{\mathbf{D}}$. The boundary field vector is represented by **F**, and is related to the wave propagating vector **P** by the medium boundary matrix **A**, i.e.

$$\mathbf{F} = \mathbf{A}\ \mathbf{P}.$$

From Maxwell's equations, we know that the tangential components of the field vector are continuous at the interface. Considering an arbitrary interface between layer 1 and layer 2, it requires: $\mathbf{F}_1 = \mathbf{F}_2$, i.e. $\mathbf{A}_1\mathbf{P}_1 = \mathbf{A}_2\mathbf{P}_2$.

Furthermore, each wave propagation vector **P** at the interface can be expressed with four-components:

$$\mathbf{P} = \begin{pmatrix} E^i_\sigma \\ E^i_\pi \\ E^r_\sigma \\ E^r_\pi \end{pmatrix},$$

where i and r refer to the incident and the reflected light, respectively. E_σ and E_π correspond to a beam with electric field perpendicular or parallel to the scattering plane, respectively. Therefore, if the medium boundary matrix **A** is known, one can calculate the incoming and reflected beam intensities at neighboring layers. The derivation for **A** is lengthy, the details as well as the final expression for an arbitrary magnetic interface is presented in Refs. [150, 151].

For a medium composed of more interfaces, an additional propagation matrix $\widetilde{\mathbf{D}}$ needs to be introduced, which accounts for the damping and the phase shift of the field. As shown in Fig. 2.10, the wave propagation vector at $z = z_2$ of medium 2 is given by $\mathbf{P}_2(\mathbf{0}) = \widetilde{\mathbf{D}_2}\ \mathbf{P}_2(z_2)$. Therefore:

$$\begin{aligned} A_1\ P_1 &= A_2\ P_2(0) \\ &= A_2\ \widetilde{D}_2\ P_2(z_2) \\ &= (A_2\widetilde{D}_2A_2^{-1})\ A_2\ P_2(z_2) \\ &= (A_2\widetilde{D}_2A_2^{-1})\ A_3\ P_3(z_2)\ . \end{aligned} \tag{2.42}$$

In summary, the propagation of light from the vacuum down to the substrate

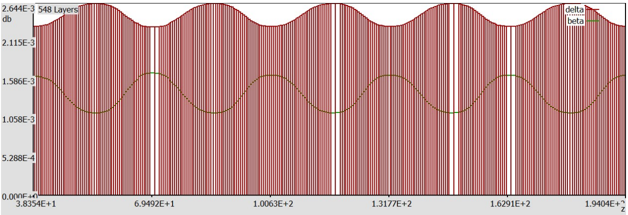

Figure 2.11.: Illustration of the layer segmentation in the Matrix formulism. Each layer can be sliced into elements with an atomic-layer thickness and individual dielectric constant. The roughness of an interface is modeled by a gradual change of the optical constants.

is described by:

$$A_{vac}\ P_{vac} = \prod_{j=1}^{m} (A_j\ \widetilde{D}_j A_j^{-1}) A_{sub}\ P_{sub}\ . \tag{2.43}$$

Similar to the Parratt formulism, this equation could be solved numerically by assuming a substrate with infinite thickness, i.e. there is basically no reflected intensity inside the substrate.

The matrix approach describes all effects that can be modeled by a dielectric tensor, since the medium boundary matrix **A** is related directly to the incident angle and the dielectric tensor [150, 151]. For each layer, both, σ and π polarized reflected and transmitted intensities are calculated simultaneously before entering the next layer. Thus this method provides the full polarization dependent scattering intensities.

To account for possible roughness of the interfaces/surface, a layer segmentation is included in the simulation (Fig. 2.11), each layer is sliced into thin elements with atomic-layer resolution. For the superlattice with a composition of (4 u.c. // 4 u.c.) LNO-LAO, each LNO block is composed of 4 u.c. LNO, and we assigned a different scattering tensor to each 1 u.c. thick LNO layer, denoted as $f^{\mathrm{B}}_{\mathrm{LNO}}$, $f^{\mathrm{A}}_{\mathrm{LNO}}$, $f^{\mathrm{A}}_{\mathrm{LNO}}$ and $f^{\mathrm{B}}_{\mathrm{LNO}}$ in Fig. 2.6(a). The layer is sliced into a bunch of layers with thickness of 0.5Å to account for the roughness. The roughness in the segmented layer is modeled by a gradual change of the optical constants (δ, β) (Fig. 2.11). The roughness between layer A and layer B was assumed to be zero ($\sigma = 0$), while at the LNO-LAO interface, the roughness was taken from the structural fit using Parratt's method.

2.4. Cluster calculation of XAS spectra

X-ray absorption spectroscopy measures core-hole excitations. In transition-metal oxides, a transition to the metal K-edges can be explained simply and nicely in a single particle model, where only one electron core excitation is considered and a number of computer codes are available to calculate the absorption cross section. However, these approaches do not give good results for the transition metal L-edges, since here multiplet effects are important due to strong overlap between the core and the valence electron wave-functions [46]. In the past years, a proper quantitative description of the core-hole excitation spectrum at L-edges was made by a cluster model based on a many body configuration interaction (CI) [12, 140, 141], accounting for the full multiplet effects.

The cluster calculation program used in this thesis was written by Maurits W. Haverkort [54, 57]. The cluster calculation was performed for a NiO_6 cluster, i.e. an octahedron with one Ni ion surrounded by six-neighboring O ligands. In LNO, the Ni ion has nominally a 3+ valence state, i.e. a $2p^63d^7$ configuration. However, the charge transfer energy is small, allowing for a transfer of electrons from O $2p$ orbitals to Ni $3d$ orbitals. For bulk LNO, it is discussed that the charge transfer energy is even negative (i.e. $\Delta = \text{-}0.5\,eV$ as shown in Fig. 2.13), giving rise to a $2p^63d^8\underline{L}$ ground state, with $\underline{L}$ denoting the ligand hole (rather than $2p^63d^7$). Within our cluster calculation, the ground state is composed of a basis set of states: $2p^63d^7\underline{L}^0$, $2p^63d^8\underline{L}^1$, $2p^63d^9\underline{L}^2$, $2p^63d^{10}\underline{L}^3$, where the three terms label the number of core electrons in the Ni $2p$, the Ni $3d$ shell and the number of holes in the ligands p shell, respectively.

For a $2p^63d^7\underline{L}^0$ configuration, there are $C^3_{10} = 120$ possible wave-functions, i.e. the first hole on the Ni site can fill in 10 possible orbitals ($m_l = \text{-}2$, -1, 0, 1, 2, each with spin up and spin down), the second hole can fill in 9 orbitals, and so on. Since the electrons are indistinguishable, this results in a total of $\frac{10\times9\times8}{3\times2\times1} = 120$ wave-functions. Similarly, there are $C^2_{10}C^1_{10} = 450$, $C^1_{10}C^2_{10} = 450$ and $C^3_{10} = 120$ wave-functions for the $2p^63d^8\underline{L}^1$, $2p^63d^9\underline{L}^2$ and $2p^63d^{10}\underline{L}^3$ configurations, respectively. Thus, the Hamiltonian is represented by a 1140×1140 matrix. Similarly, the final state of the $2p \rightarrow 3d$ dipole transition includes a basis set of: $2p^53d^8\underline{L}^0$, $2p^53d^9\underline{L}^1$ and $2p^53d^{10}\underline{L}^2$, with corresponding $C^1_6C^2_{10} = 270$, $C^1_6C^1_{10}C^1_{10} = 600$ and $C^1_6C^2_{10} = 270$ wave-functions. Therefore, there is also a 1140×1140 Hamiltonian matrix for the final state.

The ground state wave-function is a superposition of all basis configurations:

$$\Psi_i = \alpha_0 \ |p^6 d^7 \underline{L}^0 > + \alpha_1 \ |p^6 d^8 \underline{L}^1 > + \alpha_2 \ |p^6 d^9 \underline{L}^2 > + \alpha_3 \ |p^6 d^{10} \underline{L}^3 >, \quad (2.44)$$

where the coefficients (α_i, $i = 0, 1, 2, 3$) and ground state energies are obtained by diagonalizing the Hamiltonian matrix. Note that these states do not have the same energy and depend on several energy parameters, i.e. the *d*-*d* Coulomb repulsion energy U_{dd}, the O 2p - metal 3d charge transfer energy Δ, the O 2p - metal 3d hybridization T and the core-hole - d Coulomb energy U_{pd}. The energy schemes for different ground states and x-ray absorption final states are shown in Fig. 2.12, where the $2p^6 3d^7 \underline{L}^0$ configuration is assumed to be the ground state. The energy difference between $2p^6 3d^8 \underline{L}^1$ and $2p^6 3d^7 \underline{L}^0$ is only due to the charge transfer energy Δ, which characterizes the energy to move one electron from the ligand to the 3d states. The next configuration $2p^6 3d^9 \underline{L}^2$, requires additional energy to transfer electrons to the 3d states. In addition the higher occupancy of the metal *d*-orbitals cost the the electron-electron Coulomb energy U_{dd}. Thus the energy difference is Δ $+U_{dd}$. So is the energy of the next configuration, but with twice of the electron-electron interaction.

The XAS final state is different from the initial state since an additional attractive core-hole and 3d transition metal interaction must be taken into account. In the energy scheme of the final state, the on-site energy of the $2p^5 3d^8 \underline{L}^0$ configuration is set as the reference. The energy difference of $2p^5 3d^9 \underline{L}^1$ includes: the transfer of one electron from the ligand states to the Ni 3d states, the Coulomb interaction between electrons, as well as U_{pd} accounting for the attractive core-hole - 3d interaction.

The ground state Hamiltonian is expressed as:

$$H = H_{CFd} + H_{CFL} + H_{Hop} + H_{U\Delta}, \quad (2.45)$$

where H_{CFd} is the crystal field splitting of 3d orbitals, H_{CFL} is the crystal field of ligand p orbitals, H_{Hop} denotes the hopping term and $H_{U\Delta}$ is the Coulomb interaction plus the charge transfer energy term.

The crystal field effect is treated with in a mean-field approximation. The local potential can be expressed in spherical harmonics, which could be simplified by symmetry considerations. For a crystal with O_h symmetry, only one parameter is left to describe the crystal field splitting, i.e. $10Dq$, denoting the energy difference between e_g and t_{2g} states. For a lower D_{4h} symmetry, there are three parameters, i.e. $10Dq$, the energy lifting of e_g levels Δ_{e_g} (splitting between $d_{x^2-y^2}$ and $d_{3z^2-r^2}$) and the energy splitting of t_{2g} levels $\Delta_{t_{2g}}$ (energy difference between d_{xz},d_{yz} and d_{xy} orbitals)(Fig. 1.2). For a lower symmetry, like the D_{2h} and D_{3d} point group, more energy parameters should be consid-

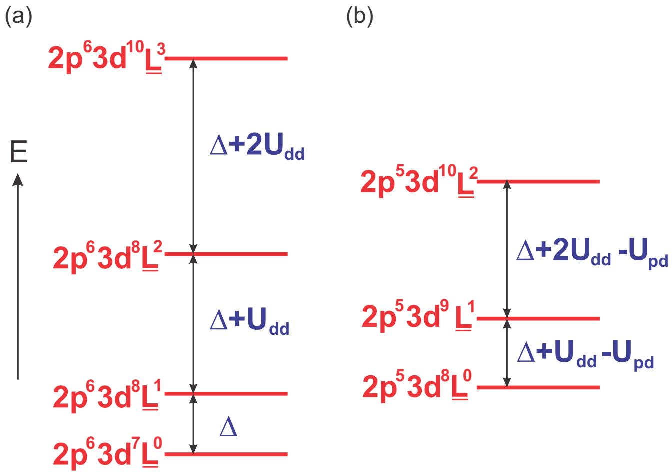

Figure 2.12.: The relative on-site energy-level scheme for (a) the ground state and (b) the XAS final states of different configurations. U_{dd}, Δ, U_{pd} denote the $3d$-$3d$ Coulomb interaction energy, the charge transfer energy and the core-hole-$3d$ Coulomb attractive energy, respectively. Here, Δ is assumed to be positive.

ered, the details are summarized in Ref.[54]. Within the scope of this thesis, cluster calculations were performed considering a D_{4h} symmetry of the NiO$_6$ cluster. We used $10Dq = 2\,eV$, while the energy splitting Δ_{e_g} was varied.

The hopping term describes the hybridization effect between oxygen and the transition metal ion which mixes the two different configurations, e.g. $2p^63d^7\underline{L}^0$ and $2p^63d^8\underline{L}^1$. It enters the off-diagonal terms of the Hamiltonian and the size of the hopping can be expressed in terms of the Slater-Koster parameters known as $pd\sigma$ and $pd\pi$ [129]. The σ bonding corresponds to those orbitals which remain symmetrical under rotation along the internuclear axis (i.e. the bonding of O $2p$ orbitals with Ni $3d_{x^2-y^2}$ and Ni $3d_{3z^2-r^2}$ orbitals), whereas the π orbitals change the phase under a rotation along the internuclear axis (i.e. the bonding of O $2p$ orbitals with d_{xy}, d_{xz} and d_{yz} orbitals). In general, the bonding of the ligand π orbitals is weaker than the ligand σ orbitals. For transition metal oxides, the transfer integral $pd\sigma$ is within the range of -1.0 to -2.5 eV [99]. In our cluster calculation, we used commonly accepted values for nickel oxides, i.e. $pd\sigma = $ -1.88 eV, and $pd\pi = pd\sigma/2.17$ [124, 135].

The last term of the initial state Hamiltonian $H_{U\Delta}$ includes the $d-d$ Coulomb interaction and the charge transfer energy, which enters the Hamiltonian in the diagonal terms and relates directly to the multiplet states for different basis configurations. The electron-electron interaction can be expressed by spherical harmonics in second quantization, the radial part is obtained from Hartree-Fock calculation as summarized in Ref. [54], where the electron-electron Coulomb interaction can be described in terms of Slater integrals, i.e. $F_{dd}[0]$, $F_{dd}[2]$ and $F_{dd}[4]$. The values of $F_{dd}[2]$ and $F_{dd}[4]$ for our calculation are used with a corrections of 80% to account for the intra-atomic CI as pointed out by F.M.F. de Groot *et al.* [26], i.e. $F_{dd}[2]=13.276*0.8$, $F_{dd}[4]=8.294*0.8$. In general, U_{dd} is around 6-8 eV for later transition metal oxides. The charge transfer energy Δ depends on the transition metal ion, which increases as the atomic number of the transition metal decreases due to the electronegativity. In our cluster calculation, the Δ value is negative, $\Delta_{3+} = \Delta_{2+} - U_{dd} = -0.5\,eV$ with $U_{dd}=7\,eV$ and $\Delta_{2+} = 6.5\,eV$ from Ni^{2+} [124]. The energy-level scheme for LNO as an example for a typical negative charge transfer insulator is illustrated in Fig. 2.13.

We emphasize again that the final state Hamiltonian is different from the initial state Hamiltonian since it takes into account the attractive interaction between the core hole and the $3d$ electrons U_{pd}, as well as the spin-orbital coupling of $2p$ holes:

$$H_{XAS} = H_{XASCFd} + H_{XASCFL} + H_{XASHop} + H_{XASU\Delta} + H_{\underline{c}LS}. \tag{2.46}$$

Similar to the treatment of $H_{U\Delta}$ in the ground state Hamiltonian, the radial part of the Hamiltonian $H_{XASU\Delta}$ now considers different spin configurations, i.e. it includes not only the $3d-3d$ Coulomb interaction and the $2p-3d$ Coulomb interaction in terms of $F_{pd}[2]$, but also the exchange interaction. The exchange interaction brings the states to singlets and triplets with different energy as $G_{pd}[1]$ and $G_{pd}[3]$. All the values are again calculated from Hartree-Fock and summarized in Ref. [54]. We take the values with a correction of 80%. For the Coulomb interaction between O $2p$ and Ni $3d$, we use $U_{pd}=8.5\,eV$. The last term represents the spin-orbital coupling of $2p$ holes $H_{\underline{c}LS}$ with a coupling strength $\zeta_{2p}=11.506\,eV$. All the parameters are summarized as Tab. 2.1.

After the diagonalization of the Hamiltonian, we obtain the eigen-energies of the ground state as well as the coefficient α_i of each configuration in the basis. The spectrum calculation is based on Fermi's Golden rule (electron-dipole approximation). As mentioned before, the expectation value of the dipole operator depends on the polarization of the incident light. For the cluster calculation with linearly polarized light, the unoccupied states are only

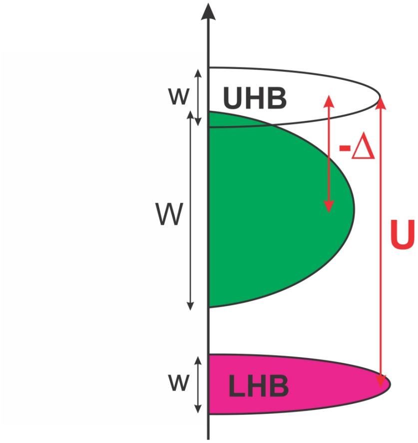

Figure 2.13: Energy-level scheme for LNO as a negative charge-transfer insulator with Δ<0, resulting in a metallic ground state due to the merging of the ligand band with the upper Hubbard band.

in the e_g levels, i.e. $d_{x^2-y^2}$ and $d_{3z^2-r^2}$ orbitals. We obtain the absorption spectrum: $F_{xx}\ d_{3z^2-r^2}$, $F_{zz}\ d_{3z^2-r^2}$, $F_{xx}\ d_{x^2-y^2}$ and $F_{zz}\ d_{x^2-y^2}$ individually, which denote the transition to $d_{3z^2-r^2}$ with x-polarized light, to $d_{3z^2-r^2}$ with z-polarized light, to $d_{x^2-y^2}$ with x-polarized light and to $d_{x^2-y^2}$ orbital with z-polarized light, respectively. The absorption spectrum for x- and z-polarized light is described in terms of the linear combination of these with 100% occupation of either the $d_{x^2-y^2}$ or the $d_{x^2-y^2}$ orbital, i.e.

$$\begin{aligned} F_{E\|x} &= \alpha * F_{xx}\ d_{3z^2-r^2} + (1-\alpha) * F_{xx}\ d_{x^2-y^2} \\ F_{E\|z} &= \alpha * F_{zz}\ d_{3z^2-r^2} + (1-\alpha) * F_{zz}\ d_{x^2-y^2}. \end{aligned} \tag{2.47}$$

U_{dd}	Δ	$pd\sigma$	$F_{dd}[2]$	$F_{dd}[2]$	U_{pd}	$F_{pd}[2]$	$G_{pd}[1]$	$G_{pd}[3]$	ζ_{2p}
7	-0.5	-1.88	10.621	6.635	8.5	6.679	6.329	3.602	11.506

Table 2.1.: List of all the parameters for cluster calculations in unit of eV. The definition of each parameter is specified in the main text.

2.5. X-ray sources

X-ray absorption measurements were performed by varying the incident photon energies and collect the absorption intensities in forms of the fluorescence yield or the total electron yield. The latter case is collecting the photoelectrical current produced by the second electrons and measures the drain current, which is weak so that the high brilliance of synchrotron radiation facility is required. Moreover, a pair of linear polarization (σ- and π-polarization) or circular polarization ($\sigma+$ - and $\sigma-$ -polarization) is needed to measure linear or circular dichroism. The modern third generation synchrotron radiation can provide almost fully polarized light. In this section, we will present a brief overview of the synchrotron radiation.

In traditional x-ray sources like x-ray tubes, electrons are generated by a heated filament and then accelerated by a high electric field to hit a target (usually tungsten, molybdenum or copper). A typical x-ray radiation spectrum includes a continuous part (known as 'bremsstrahlung' due to the deceleration of the high energy electrons and the conversion to photons) as well as several discrete characteristic white lines. Those characteristic lines are related to atomic transitions. In the x-ray source used for structure characterization here is Cu K_α radiation, which corresponds to the atomic transition from $n=2$ to $n=1$ level of Cu.

Synchrotron radiation provides electromagnetic radiation covering a broad range from hard x-rays with $E \sim 10-100\,keV$ to the far infrared range and tera-hertz range with $E \sim 1\,meV$ with high brilliance. The working principle to some extent is similar to the traditional x-ray tube: electrons are accelerated close to the speed of light in a booster and then are inducted into a storage ring with large bending magnets of regular intervals. Those bending magnets serve as guides for the electrons in the center of the storage ring. In between the bending magnets are the insertion devices which will be discussed in detail below as Fig. 2.14(b). Now relativistic accelerated electrons produce radiation in a dipole pattern with no radiation along the acceleration direction. In a synchrotron, the electrons are accelerated close to the speed of light, and the dipole pattern gives rise to intensity along the trajectory and the radiation appears in a narrow cone with an opening angle $1/\gamma$ (Fig. 2.14(a)).

Special magnetic devices can be used to customize the radiation characteristics for special experimental requirements, which are called “insertion devices” (IDs). Regular IDs are wigglers and undulators consisting of a series of periodically arranged magnets which deflect the electron beam path sinusoidally. A dimensionless strength parameter $K = \frac{eB_0\lambda_u}{2\pi\ mc} = 0.934B_0(\mathrm{T})\lambda_u(cm)$ is defined to distinguish a wiggler and an undulator. It is called a wiggler for

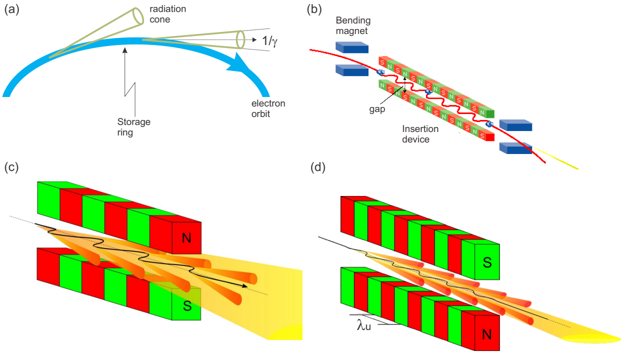

Figure 2.14.: (a) Trajectory of electrons moving in the storage ring, electron relativistic radiation along the forward direction with the radiation cone $1/\gamma$. (b) Illustration of the bending magnet and insertion devices. (c) Insertion devices: wigglers with radiation intensity proportional to the number of magnet poles N and a broad radiation spectrum. (d) Insertion devices: undulator with a periodic arrangement of magnets, the constructive interference of electrons resulting in an enhanced intensity proportional to N^2 and a narrow radiation angle. Panel (b)-(d) are adapted from SPring 8 and DESY synchrotron radiation facility websites.

$K \gg 1$ and known as an undulator for $K \ll 1$. Wigglers could be considered as a series of bending magnets where the radiation intensity is enhanced and scales with the number of magnetic poles N. Every electron of the electron bunch radiates independently resulting in a broad radiation spectrum (Fig. 2.14(c)).

An undulator has the big advantage that oscillating electrons interfere constructively and result in a narrow radiation cone in the forward direction. The electron beam is periodically deflected by weak magnetic fields. The electrons perform oscillations with the same period of the undulators. The emission wavelength of the electrons in an undulator is given by the undulator period (L_p), shortened first by the Lorentz contraction (γ) and then by the Doppler shift(γ). It means that the normal undulator period length is of the order of cm, which is reduced by a factor γ^2 ($\sim 10^6 - 10^8$) to yield short wavelength radiation in the x-ray regime, i.e. the electrons could 'see' the compressed undulator (Fig. 2.14(d)).

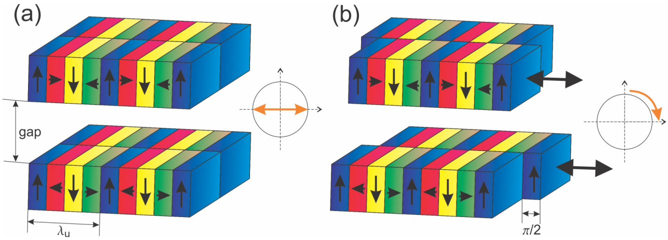

Figure 2.15.: Illustration of permanent magnet arrangement to produced circular polarized light. Panel (a) Linear (horizontal) polarized light perpendicular to the electron trajectory. Panel (b) Circular left (or right) polarized light which is realized by shifting the relative positions of the diagonal array of magnets.

In general, wigglers cover a broad radiation spectrum range, while undulators are optimizied the beam brightness in a comparably small energy range. Despite synchrotron x-ray sources have the big advantage of high brilliance (which is defined as a quantity related to the number of photons per second, the collimation of the beam, the beam size as well as the spectral distribution), it can provide light with a broad and tunable energy range and a high degree of polarization. The first practical question would be how to tune the photon energy. The wavelength is changed by varying the gap between the magnetic dipoles, namely, changing of the gap modifies the magnetic field strength, thus the K value, resulting in a photon energy matching the experimental demand. The emission photon energy is given by:

$$\varepsilon_k(eV) = 950 \, \frac{kE^2(GeV^2)}{\lambda_u(cm)(1+\frac{1}{2}K^2+\gamma^2\theta^2)} \tag{2.48}$$

where E is the energy of electrons, k is the k-th harmonic (only odd harmonics exist), K denotes the strength parameter which as mentioned could be modified by the magnetic field strength, λ_u is the periodicity of the magnetic undulator field, γ is the relativistic factor of electrons, and θ is the observation angle from the undulator axis.

The synchrotron light is linearly polarized in the electron plane (perpendicular to the electron trajectory). The change from linearly polarized light to circularly polarized light is done by shifting the relative positions (phases) of the diagonal arrays of magnets by $\frac{1}{4}\lambda_u$ (as shown in Fig. 2.15(b)).

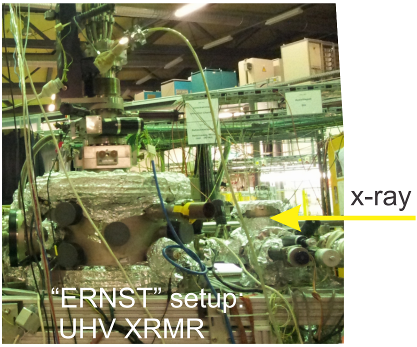

Figure 2.16: The setup of the the UE56/2-PGM1 soft-x-ray beamline at BESSY II in Berlin, Germany, with the advanced three-axis ultrahigh-vacuum (UHV) resonant magnetic reflectometry (XRMR).

2.6. The experimental setup

The resonant x-ray reflectivity and x-ray absorption spectroscopy (XAS) measurements were performed at the UE56/2-PGM1 soft-x-ray beam line at BESSY II in Berlin, Germany, using the advanced three-axis ultrahigh-vacuum reflectometer described in Ref. [15] (as shown in Fig. 2.16).

Since it is impossible to perform measurements with the electric field vector of the incident light parallel to the surface. Therefore, an absorption measurement is always performed with the sample tilted by an arbitrary angle θ with respect to the incident photon propagation direction. Fig. 2.17 shows a sketch of the measurement geometry in the front view (a) and an illustration of the scattering geometry from the top view (panel (b)). Linearly polarized soft x-rays (σ and π polarization) tuned to the resonant edges were used to measure XAS spectra in two collection modes, total electron yield (TEY) and total fluorescence yield (FY). The TEY mode is collecting the photocurrent induced by scattered secondary electrons. The idea is as follows: x-rays make core-hole excitations, the core holes are filled by Auger decay which is dominant in the soft x-ray region. On the one hand the emitted Auger electrons can provide a direct measurement of the x-ray absorption intensity which is highly surface sensitive (less than 10Å in the soft x-ray region), known as Auger electron yield. On the other hand, the Auger electrons create secondary electrons which are the main contribution to the TEY intensity.

The measured intensity is proportional to the projected density of states along this special direction, which includes two contributions, i.e. from the in-plane component $I_{E\parallel x}$ and the out-of-plane component $I_{E\parallel z}$. They satisfy the following equation [131]:

$$I(\theta) = I_{E\parallel x}\cos^2\theta + I_{E\parallel z}\sin^2\theta. \tag{2.49}$$

Particularly, the measurements here are performed with an incident angle $\theta = 30^\circ$ with σ- and π-polarized light. The intensity along the in-plane direction $I_{E\parallel x}$ directly corresponds to the integrated intensity of the σ-polarized spectrum. However, a correction of the geometry for the intensity along the out-of-plane direction $I_{E\parallel z}$ is needed, which is proportional to the unoccupied hole states along z-direction. Applying Eq.2.49 we obtained:

$$\begin{aligned} I_{E\parallel x} &= I_\sigma \\ I_{E\parallel z} &= \frac{4}{3}(I_\pi - \frac{1}{4}I_\sigma), \end{aligned} \tag{2.50}$$

where I_σ and I_π denote the intensity for σ- and π-polarized absorption spectra, and $I_{E\parallel x}$ and $I_{E\parallel z}$ represent the intensity along the in-plane and the out-of-plane direction, respectively.

The photocurrent is measured by a Keithley 6715A electrometer. Secondary electrons created deeper in the sample can hardly escape due to the work

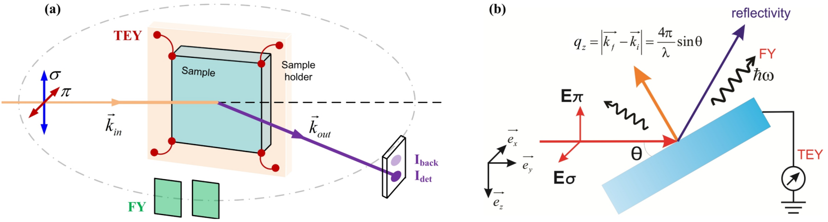

Figure 2.17.: Panel (a): Sketch of the measurement geometry in the front view. The absorption spectra are collected in both TEY and FY modes simultaneously. Panel (b): Illustration of the scattering angles and scattering geometry. The sample is tilted with an angle θ related to the incoming beam direction. The absorption as well as the resonant x-ray reflectivity spectra are measured for both σ and π polarization. The reflectivity intensity is collected with a Hamamatsu GaAsP diode. q_z denotes the momentum transfer during the scattering process along the specular direction.

function, making TEY a surface sensitive method with a penetration depth up to a few angstroms in the soft x-ray region. Four contacts are made at the sample surface to provide a good conductivity. The emitted fluorescence light is collected by two Hamamatsu GaAsP diodes (G1740 type) which are placed in front of the samples. Therefore, in an absorption measurement, both TEY and FY intensities are collected simultaneously. The reflected beam intensities were detected with a Hamamatsu GaAsP diode (G1116 type), which is placed in a direction perpendicular to the propagation direction of the outgoing light. A second diode is mounted 28 mm above the scattering plane to measure the diffuse background from the sample. All intensities were normalized to the incoming intensity measured with a gold mesh.

3. Sample preparation and structural characterization

3.1. Bulk structural properties

In this section, a summary of the bulk properties of the studied compounds is presented. The composition of the nickel oxide superlattices is denoted as $ANiO_3$-RXO_3 (ANO-RXO) $(x//y)\times\ m$, with A = La, Pr, R = La, Dy, Gd, Pr and X = Al, Ga, Sc, where x, y denote the number of unit cells for ANO and RXO, respectively, with a stacking repetition of m times.

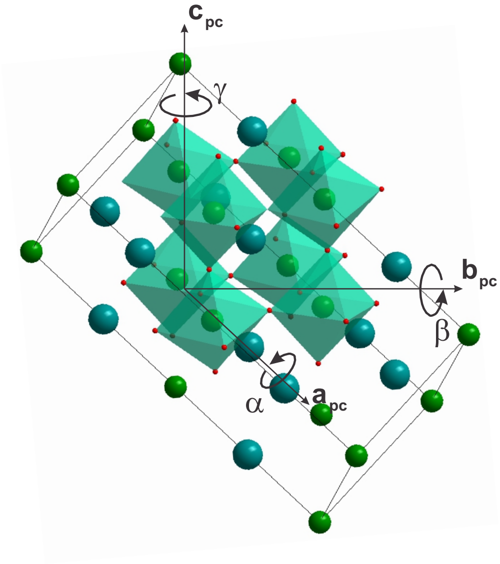

Figure 3.1.: Crystal structure of bulk LNO with a trigonal cell and the cubic unit cell is highlighted by octahedra.

Fig. 3.1 shows the crystal structure of bulk LNO with a trigonal cell. The pseudo-cubic unit cell is highlighted by the octahedra. The octahedral distortion away from the ideal cubic pervoskite can be described using the Glazer notation [43]. Bulk LNO is described by an $a^-a^-a^-$ rotation pattern, where the corresponding rotation angles are $\alpha = \beta = \gamma = 5.2°$ with respect to the pseudocubic a_{pc}-, b_{pc}- and c_{pc}- crystal axes [92].

Throughout this thesis, we studied LNO-based and PNO-based oxide superlattices. Chapter 4 mainly presents the experimental results of LNO-based superlattices with four consecutive unit cells LNO and equally thick layer stacks of the different band insulators RXO (i.e. LAO, $LaGaO_3$ (LGO), $DyScO_3$ (DSO) and $GdScO_3$ (GSO)). These samples were grown on different substrates with different lattice constant mismatch compared to bulk LNO, i.e. on $YAlO_3$ (YAO), $LaSrAlO_4$ (LSAO), $SrTiO_3$ (STO), DSO, and GSO substrates. Tab. 3.1 summarizes the bulk properties of these compounds[1].

Chapter 5 focuses on the experimental results of PNO-PAO superlattices with $x = y = 4$ u.c. grown on different substrates, i.e. on STO, LSAO, LAO and $(LaAlO_3)_{0.3}$-$(Sr_2Al_{0.5}Ta_{0.5}O_6)_{0.7}$ (LSAT). The bulk properties as well as the lattice constant mismatch compared to bulk PNO are summarized in Tab. 3.2. The space group of bulk PNO is *Pbnm* at room temperature; this so-called $GeFeO_3$-type distortion is found in many related perovskites.

3.2. Deposition method: pulsed laser deposition

Pulsed laser deposition (PLD) is a thin film preparation technique which is commonly used for complex oxides such as high T_c superconductors [17, 32], piezoelectric and ferroelectric materials [154] etc, with the advantage that the deposited films preserve the cation stoichiometry of the target materials. The deposition process is as follows: the PLD chamber is pumped to low pressure to ensure a long mean free path of evaporated particles. A high power laser beam is focused on the target inside a vacuum chamber. A laser plume is formed due to the vaporization of atoms from the target material, which travels mostly in the forward direction. Eventually, the ablated material is deposited as thin films on a substrate. The substrate is always heated to a certain temperature to provide the sufficient activation energy for atom diffusion as well as to enable epitaxial growth with a proper reaction between the thin film and the substrate of a certain phase. The optimized growth condition for each material can be controlled by deposition parameters such as laser pulse, laser energy,

---

[1] Note that the density stated in Tab. 3.1- 3.2 is also the one used to calculate the optical constant (Eq.2.37).

Compounds	lattice constant (Å)	space group	a_{pc} (Å)	ρ (g/cm^3)	m (%)
LNO	a=b=5.456, c=13.143	R$\bar{3}$c [144]	3.837	7.268	-
LAO	a=b=5.363, c=13.103	R$\bar{3}$c [58]	3.789	6.329	-1.2
LGO	a=b=5.531, c=13.394	R$\bar{3}$c [29]	3.889	7.231	+1.3
DSO	a=5.554, b=5.71, c=7.89	Phnm [84]	3.95	6.9	+3.0
GSO	a=5.45, b=5.75, c=7.93	Pbnm [84]	3.96	6.6	+3.2
STO	a=b=c=3.905	Pm$\bar{3}$m [63]	-	5.11	+1.6
LSAO	a=b=3.756, c=12.636	I4/mmm [126]	-	5.92	-2.4
YAO	a=5.18, b=5.31, c=7.35	Pbnm [118]	3.71	4.88	-3.5

Table 3.1.: Bulk properties for LNO-based superlattices: compounds, bulk lattice constant, space group, pseudocubic lattice constant, density ρ as well as the lattice constant mismatch m compared with bulk pseudo-cubic LNO. Different signs and amplitudes of the lattice mismatches are induced to the superlattices, i.e. $a_{YAO} < a_{LSAO} < a_{\mathrm{LNO\,bulk}} < a_{STO} < a_{DSO} < a_{GSO}$ where a is the lattice constant of the pseudocubic perovskite structure. The lattice mismatch is calculated by $(a_{sub}$-$a_{LNO})/a_{LNO}$.

deposition temperature, background pressure and so on. Monitoring precisely the growth rate can be realized by reflection high-energy electron diffraction (RHEED) where one oscillation period in the diffraction pattern corresponds to the deposition of one unit cell based on the diffraction and reconstruction of the surface. However, the PLD system for the nickelate superlattices studied here is not equipped with RHEED which is very challenging to be combined with the requirement of a high oxygen pressure for the growth of stoichiometric $LaNiO_{3.0}$. Fig. 3.2(b) shows a schematic view of the PLD chamber used for the nickelate superlattices' deposition. Fig. 3.2(c) is a photograph of the laser plume. The high laser plume intensity indicates highly ablation rates and highly energetic particles during the thin film deposition process.

Compounds	lattice constant (Å)	space group	a_{pc} (Å)	ρ (g/cm^3)	m (%)
PNO	a=5.42, b=5.38, c=7.63	Pbnm [97]	3.815	6.31	-
PAO	a=b=5.327, c=12.957	R$\bar{3}$c [153]	3.737	6.73	-2.4
STO	a=b=c=3.905	Pm$\bar{3}$m [63]	-	5.11	+1.9
LSAO	a=b=3.756, c=12.636	I4/mmm [126]	-	5.92	-2.0
LSAT	a=b=c=3.87	PN3-MZ [110]	-	6.74	+1.0
LAO	a=b=5.363, c=13.103	R$\bar{3}$c [58]	3.789	6.329	-1.0

Table 3.2.: Bulk properties for PNO-based superlattices: compounds, bulk lattice parameters, space group, pseudocubic lattice constant, density ρ as well as the lattice mismatch m related to the bulk pseudocubic PNO. Similarly, the lattice mismatch is calculated by $(a_{sub}$-$a_{PNO})/a_{PNO}$.

The superlattices are deposited by pulsed laser deposition from stoichiometric targets of ANO and RXO, using a KrF excimer laser with a deposition rate of $2\,Hz$ and an energy density of $1.6\,J/cm^2$. All materials are deposited in $0.9\,mbar$ oxygen atmosphere at $730\,^\circ C$, followed by annealing in $1\,bar$ oxygen atmosphere at $690\,^\circ C$ for $30\,min$. Thickness control of the individual superlattice layer is accomplished by counting laser pulses. A first rough estimation of the individual grow rates η_{ANO} and η_{RXO} of ANO and RXO is obtained from thin films grown on different substrates. Taking those grow rates as starting values, we deposite superlattices with, e.g. (i) (2//4) u.c. and (ii) (3//3) u.c. structure, where 1 u.c. of ANO (RXO) corresponds to x_k (y_k) laser pulses for samples $k=$(i),(ii). By solving the linear equation system $x_k \cdot \eta_{ANO} + y_k \cdot \eta_{RXO} = D_{\mathrm{SL}}$, where D_{SL} is determined from the x-ray diffraction feedback of sample $k=$(i), (ii), we optimized the grow rates for the deposition of both materials.

Prior to the thin film deposition, most of the substrates are chemically treated to provide a well-defined surface for the layer-by-layer deposition. The surface morphology before and after the thin film deposition is characterized by Atomic Force Microscopy (AFM) as shown in Fig. 3.3. The working principle of AFM with very high-resolution images at nano-scales can be simply summarized as follows: it works essentially as a scanning probe microscope, where the cantilever with an atomically sharp tip is scanned over the sample surface. During the scan, the tip moves up and down following the contour of the surface, different deflections of the cantilever are expected. The deflection is measured through a laser beam focused on the front side of the cantilever and converts it into an array of position-sensitive photodiodes. If the measured deflection is different from the expected value, the feedback system transfers this information to a piezoelectric material connected to the cantilever which then adjusts the relative height of the cantilever. The tip can scan at a constant height or at a constant force mode. However, in a constant height mode, the tip can be easily damaged due to surface collision. Hence, in most cases, a constant force with tunable tip-to-sample distances is used. The cantilever position and its oscillation can be detected as a function of the lateral position of the sample which reflects the information of the sample surface.

STO (miscut angle $< 0.1\,^{\circ}$) is treated using a HF solution followed by annealing at $900\,^{\circ}C$ for 1 hour to obtain the TiO$_2$-termination and a good surface recombination [74]. AFM images, taken after the termination, reveal a step height of 4-5 Å and a terrace width of 300-500 nm (Fig. 3.3(b)-(c)(left)). This surface morphology provides an optimized surface for the growth of super-

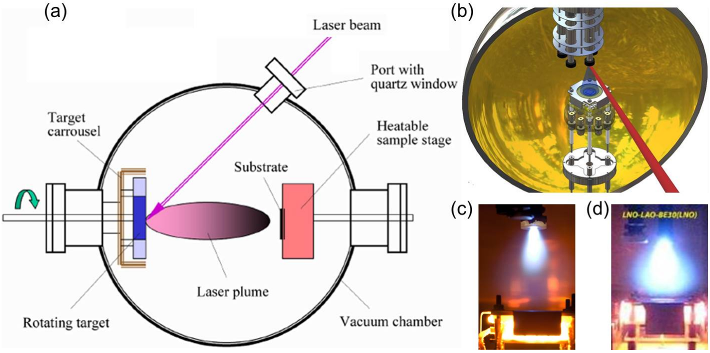

Figure 3.2.: (a) Sketch of the PLD system. Figure adapted from the website at the research group of Prof. R. Schwarz, I.S.T., Lisboa, Portugal. (b) Schematic view of the inner part of the PLD chamber (© Max-Planck-Institute for Solid-State-Research). Photograph of the laser plume (c) when LAO and (d) when LNO is deposited.

a) LNO-DSO-BE20 (4 //4) x 8 on DSO

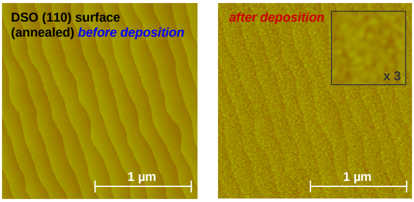

b) LNO-DSO-BE19 (4 //4) x 8 on STO

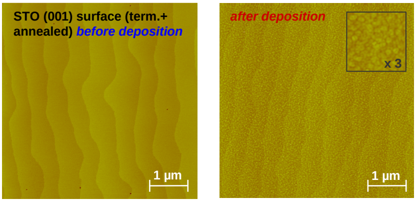

c) LNO-LGO-BE16 (4 //4) x 8 on STO

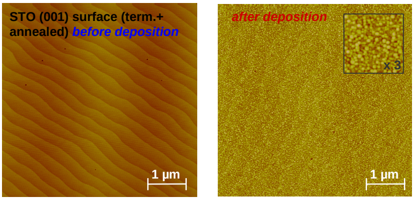

Figure 3.3: Ex-situ AFM pictures of the specimen surfaces before and after deposition on various substrates for a) LNO-DSO on DSO, b) LNO-DSO on STO and b) LNO-LGO on STO. For all the three samples the surface morphology of the substrate is preserved after the deposition of the superlattice.

lattices with atomically flat interfaces. The LSAO substrates are not further treated and hence the surface termination is unknown. However, the big out-of-plane lattice constant with both LaO and SrO layers, between alternating AlO_2 layers might cause a more complex substrate-superlattice interface as indicated from the cross-sectional TEM studies [27, 28]. The DSO substrate was annealed to obtain surface rearrangement before the deposition of superlattices. The surface morphology shows ~4 Å high terraces, but the termination is unclear (Fig. 3.3(a)(left)). AFM images indicate that the superlattices preserve the surface morphology of the substrate after the deposition (right panels of Fig 3.3). The deposited LNO-RXO surfaces show small islands which indicate a layer-by-layer epitaxial growth. The island diameters are roughly a) 300 Å, b) 500 Å, and c) 300 Å for different specimens (see insets in Fig. 3.3), in good agreement with the structural coherence length determined from x-ray diffraction [27, 34].

3.3. Structural characterization

3.3.1. X-ray diffraction experimental setup

X-ray diffraction (XRD) is a powerful tool to check the crystal quality, to verify the chemical composition, and the preferred crystal orientation, as well as to determine the atomic structure of a crystal. The diffraction experiments throughout this thesis were performed on a four-circle diffractometer with four tunable angles ω, 2θ, χ, and ϕ, as indicated in Fig. 3.4. The experiments are done in a ϕ-fixed mode, since the crystal orientation is sufficiently determined by three degrees of freedom. The diffraction intensity is collected by a Mythen detector (line detector), which consists of a linear array of small n-doped Si microstrip sensors.

A coupled $\omega - 2\theta$ scan is used to measure the Bragg diffraction angles corresponding to different diffraction planes. The scans along the specular direction ([00l] in Fig. 3.4(b)) of thin films show characteristic thickness fringes, which arise from the interference of x-ray waves diffracted from the thin film interface and the surface of substrate. From the period of the thickness fringes, the total thickness of thin film can be read off. The additional periodicity of

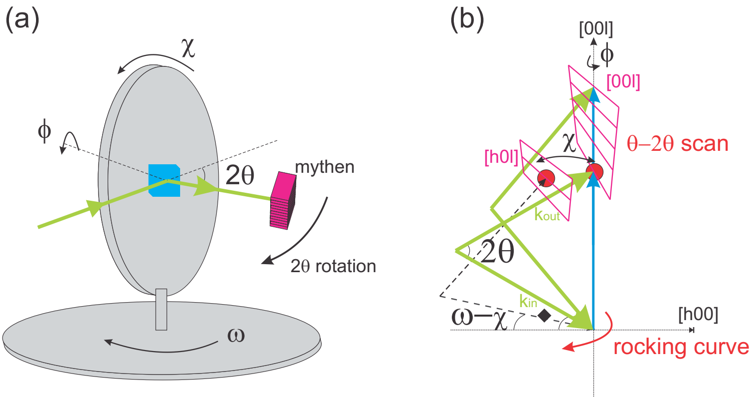

Figure 3.4.: (a)Sketch of a 4-circle x-ray diffractometer with four tunable angles: ω, 2θ, χ, and ϕ. (b) A sketch of how different angular scans movements give rise to 2D maps in reciprocal space using the mythen detector along the specular [00l] and the off specular [h0l] directions.

a superlattice gives rise to satellite peaks around the main peak (i.e. $(00l)$ reflection). From the position of the satellite peaks, the superlattice bilayer thickness is obtained.

Reciprocal space mapping (RSM) allows one to measure a two dimensional diffraction pattern in k-space (pink area in Fig. 3.4(b)). In principle, two reciprocal space points along different crystal directions should be enough to define the whole reciprocal space for a crystal with tetragonal or cubic symmetry. A more accurate definition of the reciprocal space can be achieved by aligning more reciprocal space points along the specular and the off-specular directions (better statistics). As shown in Fig. 3.4(b), the off-specular reciprocal lattice point could be reached by either rotating the scattering plane from $(h0l)$ to $(0kl)$ plane by χ (which is perpendicular to the sketched scattering plane) or staying in $(h0l)$ plane with the tilting of χ compensated by ω $((\omega - \chi)$ or

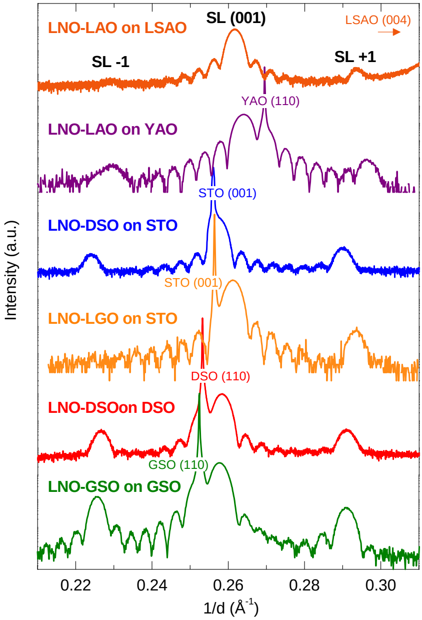

Figure 3.5.: High resolution x-ray diffraction scans along the specular rod $(00l)$ of the investigated samples.

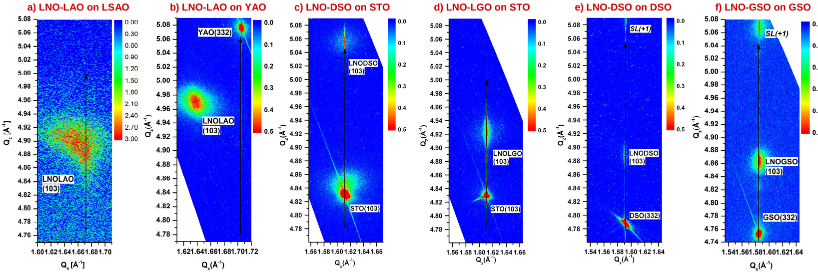

Figure 3.6.: Reciprocal space maps around the cubic (103) peak position for (4//4) u.c. superlattices (a) LNO-LAO-BE110 on LSAO, (b) LNO-LAO-BE27 on STO, (c) LNO-DSO-BE19 on STO, (d) LNO-LGO-BE16 on STO, (e) LNO-DSO-BE20 on DSO, and (f) LNO-GSO-BE7 on GSO.

$(\omega + \chi)$). Both approaches basically provide the same result as long as the crystal has a cubic or tetragonal symmetry. From the reciprocal lattice points along the off-specular direction, one can obtain the in-plane lattice constant, which allows a direct evaluation of the strain state, i.e. whether the thin films or superlattices are fully strained to the substrate (with identical in-place lattice constant) or relaxed (thin film with the same in-plane lattice constant as the bulk material) or partially relaxed (the reciprocal space pattern lies between the fully strained line and the fully relaxed line).

3.3.2. Structural properties of LaNiO$_3$-RXO$_3$ superlattices

In this study, high resolution XRD has been used to test the quality of the LNO-based superlattices and to provide structural information such as the lattice constants, the periodicity as well as the thickness of the superlattices. Fig. 3.5 shows the XRD scans along the specular rod (with Cu K_α radiation, i.e. $E = 8047\,eV$) for LNO-RXO (4 u.c.//4 u.c.) superlattices. The diffraction intensity is plotted as a function of $1/d$. Symmetrically around the $SL(001)$ peaks, we observe superlattice satellites, labeled with $SL{+}1$ and $SL{-}1$ in each panel and thickness fringes in-between. From the position of the satellites we obtain the bilayer thickness d_{bi} and from the periodicity of the thickness fringes the total thickness D is read off. Figs. 3.6 shows the off-specular RSMs around the (103) reflection, from which we obtained the average in-plane and out-of-plane lattice constant a_{SL} and c_{SL}, respectively, all the values are tabulated in

Composition	Sub.	d_{bi} (Å)	D (Å)	a_{SL} (Å)	c_{SL} (Å)	R
LNO-LAO	LSAO	30.1±0.6	314±8	3.756(5)	3.813(5)	0 %
LNO-LAO	YAO	30.5±0.5	243±6	3.835(5)	3.790(3)	100 %
LNO-LAO	STO	30.2±0.5	247±8	3.853(2)	3.779(3)	54 %
LNO-LGO	STO	30.5±0.5	245±5	3.902(2)	3.829(1)	0 %
LNO-DSO	DSO	31.0±0.5	244±10	3.949(2)	3.870(2)	0 %
LNO-DSO	STO	30±1	241±10	3.905(2)	3.870(10)	0 %
LNO-GSO	GSO	30.6±0.4	248±9	3.964(3)	3.881(3)	0 %

Table 3.3.: Superlattice composition, substrate material, bilayer thickness d_{bi}, total thickness D, and lattice parameter a_{SL}, and c_{SL} of the investigated LNO-based heterostructures. The averaged LNO-RXO in-plane a_{SL} and out-of-plane c_{SL} lattice constants have been determined by hard x-ray reciprocal space mapping around the cubic (013) reflex positions and scans along the specular rod (Fig. 3.5). Note that the lattice constants have been determined with respect to the substrate lattice parameters and by assuming a tetragonal crystal structure of the overlayer. The last column shows the relaxation R in percentage, where 0 % corresponds to a "fully-strained" state and 100 % corresponds to a "fully-relaxed" state related to the substrate.

Tab. 3.3.2. In same case we tried to get better values by taking into account the (002) and (203) reflections as well. The error bars of c_{SL} and a_{SL} are obtained by evaluating (001), (002), (103), (203) reflections and (103), (203) reflections, respectively. The layer reflections with respect to the fully strained case (black line) are marked in each map, providing the relaxation information of the superlattices. Note that the superlattices are fully strained, showing the same in-plane lattice constant as the substrate. The only exception is LNO-LAO grown on YAO substrate which is fully relaxed.

3.3.3. LaNiO$_3$-DyScO$_3$ superlattices: the effect of cation R on orbital occupancy

The effect of cation R in orbital occupancy can be directly evaluated by carefully designing the superlattice configurations, as explained in Sec. 4.4 in detail. For this purpose, two superlattices are studied:

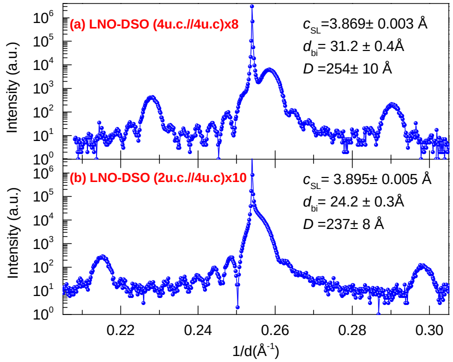

Figure 3.7.: High resolution x-ray diffraction scans along the specular direction of LNO-DSO superlattices with different stacking sequences, as written in each panel.

(**a**) LNO-DSO (4 u.c.//4 u.c.)×8 grown on DSO substrate;
(**b**) LNO-DSO (2 u.c.//4 u.c.)×10 grown on DSO substrate.

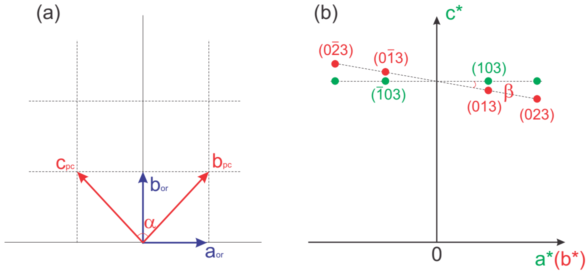

Figure 3.8.: Illustration of the relationship between orthorhombic and pseudocubic perovskite unit cells. Panel (a): a_{or} and b_{or} denote the orthorhombic cell frame, b_{pc} and c_{pc} represent the the pseudocubic unit cell, which is along the <110> and <1$\bar{1}$0> directions in the orthorhombic cell. Panel (b) sketches the crystallographic structure in the reciprocal lattice of a pseudocubic unit cell. The (103) and ($\bar{1}$03) reflections show identical Q_z values, whereas the (013) and (0$\bar{1}$3) reflections show different Q_z values, which is characteristic of the orthorhombic distortion.

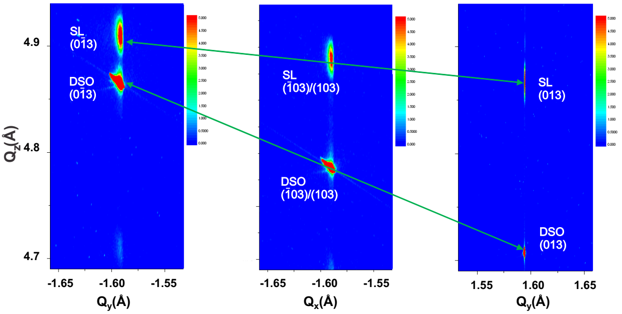

Figure 3.9.: Reciprocal space maps around $(0\bar{1}3)$ (*left*), $(\bar{1}03)/(103)$ (*middle*) and (013) (*right*) reflections of sample (**a**): LNO-DSO (4 u.c.//4 u.c.)×8 superlattice grown on DSO substrate in a pseudocubic reciprocal unit cell.

Fig. 3.7 shows the XRD patterns for LNO-DSO superlattices along the specular direction. The average lattice constant c_{SL}, the bilayer thickness d_{bi} as well as the total thickness D are shown in the legend.

The DSO substrate has an orthorhombic structure ($a_{or} \neq b_{or} \neq c_{or}$). The orthorhombic distortion can be described by a pseudocubic unit cell with a tilt angle β, denoting the deviation of the angle between the pseudocubic (010) and (001) planes (or between $(110)_{\mathrm{or}}$ and $(1\bar{1}0)_{\mathrm{or}}$ plane in the orthorhombic unit cell) from 90° (Fig. 3.8(a)). The reciprocal lattice points in a pseudocubic

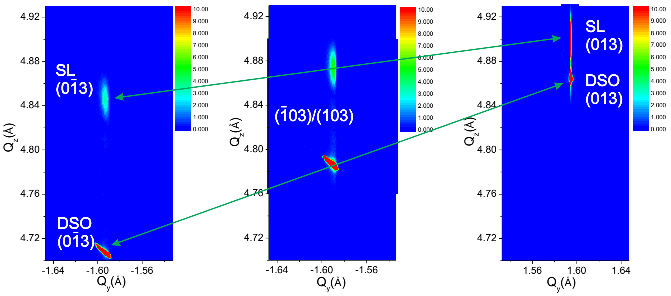

Figure 3.10.: Reciprocal space maps of sample (**b**) LNO-DSO (2 u.c.//4 u.c.) around $(0\bar{1}3)$ (*left*), $(\bar{1}03)/(103)$ (*middle*) and (013) (*right*) reflections in a pseudocubic reciprocal unit cell.

unit cell taking into account the orthorhombic distortion are illustrated in Fig. 3.8(b). Note that the reciprocal lattice points show identical Q_z values along $(h0l)$ and $(\bar{h}0l)$ planes, whereas different Q_z values exist along $(0kl)$ and $(0\bar{k}l)$ planes, such as the (013) and $(0\bar{1}3)$ reflexes as shown in Fig. 3.8. A similar crystallographic structure of the $NdGaO_3(110)$ substrate has been reported in Ref. [38]. The tilt angle β for the orthorhombic distortion can be obtained from RSM measurements through: $\beta = \arctan \frac{\Delta Q_z}{2Q_x}$.

Figs. 3.9 and Figs. 3.10 show reciprocal space maps around the {013} family. Bulk DSO in a pseudocubic unit cell exhibits a lattice constant $c_{pc} = 3.944$ Å and $\beta \sim 2.8°$. The superlattices follow the distortion of the substrate, but with clearly smaller distortion angles than the substrate. Slightly different tilt angles, i.e. $\beta = 0.84°$ and $\beta = 0.97°$ were estimated from the read-off positons of the reciprocal lattice points for sample **a** and sample **b**, respectively.

3.3.4. LaNiO$_3$-LaGaO$_3$ superlattices: a probe of octahedral distortions

Chapter 6 discusses the layer resolved orbital profiles and their sensitivity to different bonding environments, i.e. different octahedral rotation patterns in LNO layers. Two samples are under investigation particularly:

Sample **A**: LNO-LGO (1 u.c.//3 u.c.) × 16 on STO substrate;

Sample **B**: LNO-LGO (1 u.c.//4 u.c.) × 13 on STO substrate.

The samples are prepared with approximately the same total thickness. Good sample qualities are verified by hard x-ray diffraction measurements as shown in Fig. 3.11, where both superlattices show satellite peaks and thickness fringes in between. The superlattice structural parameters including d_{bi} and D as well as the average out-of-plane lattice constant c_{SL} are shown in the corresponding legend.

3.3.5. Structural properties of PrNiO$_3$-PrAlO$_3$ superlattices

Similar experiments have been performed also for PNO-PAO superlattices on different substrates. Fig. 3.12(a) shows the XRD scans along the specular direction and Fig. 3.12(b)-(e) show the corresponding reciprocal space maps around the (103) reflection. The superlattice structural parameters, i.e. d_{bi} and D, as well as the crystal lattice constants a_{SL} and c_{SL} assuming a tetragonal crystal symmetry are summarized in Tab. 3.3.5. For superlattices grown on compressive strain inducing substrates, they show the same a_{SL} as the substrate indicating a fully strained state. However, the superlattices are partially relaxed when grown on LSAT and STO substrate. The relaxation can

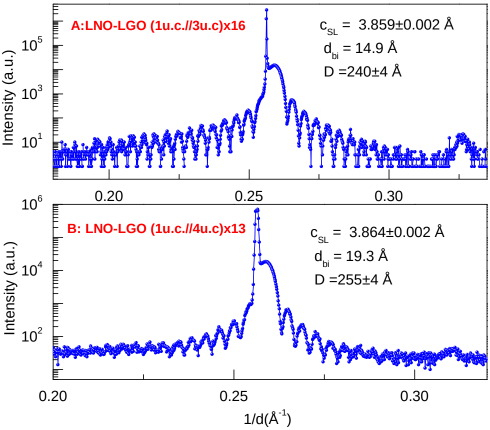

Figure 3.11.: High resolution x-ray diffraction measurements along the specular $(00l)$ direction for superlattice **A**: LNO-LGO (1 u.c.//3 u.c.)×16 on STO substrate (top panel) and superlattice **B**: LNO-LGO (1 u.c.//4 u.c.)×13 grown on STO substrate (bottom panel).

be defined as:

$$R = \frac{a_L^{str} - a_s}{a_L^{rel} - a_s}, \tag{3.1}$$

Composition	Sub.	d_{bi} (Å)	D (Å)	a_{SL} (Å)	c_{SL} (Å)	R
PNO-PAO	STO	31±1	241±6	3.831(2)	3.766(3)	57 %
PNO-PAO	LSAT	30±0.5	237±8	3.847(3)	3.75(3)	24 %
PNO-PAO	LAO	31.2±0.5	251±9	3.79(1)	3.788(3)	0 %
PNO-PAO	LSAO	30.8±0.3	260±8	3.755(3)	3.823(3)	0 %

Table 3.4.: Superlattice composition, substrate material, bilayer thickness d_{bi}, total thickness D, and lattice parameter a_{SL}, and c_{SL} of the investigated nickelate heterostructures. The averaged PNO-PAO in-plane a_{SL} and out-of-plane c_{SL} lattice constants have been determined by hard x-ray reciprocal space mapping around the cubic (013) reflex positions and scans along the specular rod (Fig. 3.12(b)-(d)).

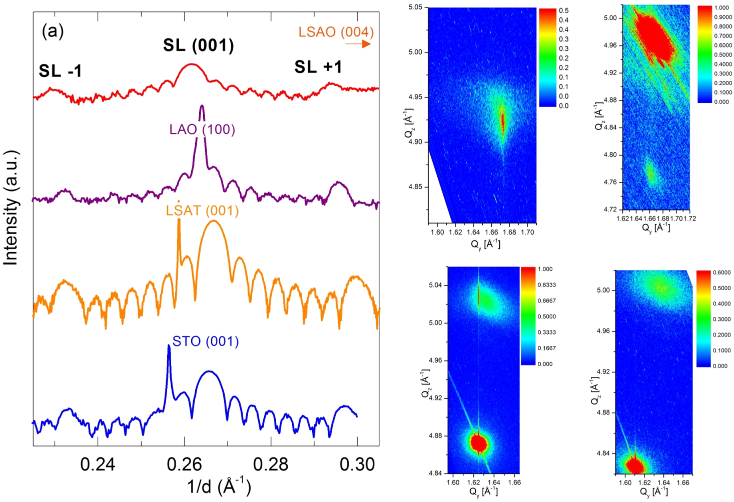

Figure 3.12.: High resolution x-ray diffraction scans for PNO-PAO superlattices. Panel (a) shows the XRD spectra along the specular rod $(00l)$ for PNO-PAO (4 u.c.//4 u.c.) grown on LSAO, LAO, LSAT as well as on STO substrate. Panel (b)-(e) shows the corresponding reciprocal space maps around the (103) reflex. Note that for the superlattices grown on tensile strain induced substrates, the thin films are partially relaxed as discussed in the main text.

where a_L^{str} and a_L^{rel} denote the in-plane lattice constant of the strained and the relaxed layer, respectively. The parameter a_s represents the in-plane lattice constant of the substrate. Here, we take $a_L^{rel} = 3.776$ Å (the averaged in-plane lattice constant of PNO and PAO layers), a_L^{str} is the measured averaged lattice constant of the superlattice. We obtain a relaxation of 24 % and 57 % for the LSAT substrate ($a_s = 3.87$ Å) and the STO substrate ($a_s = 3.905$ Å), respectively.

3.4. Electrical transport measurements

The electrical resistance measurements were performed using a standard four probe method. For this measurement four contacts were made using silver paste and gold wires, known as Van-der Pauw method. Fig. 3.13(a) shows

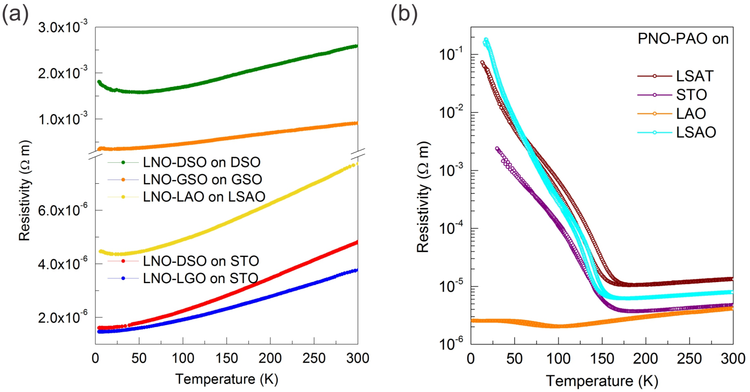

Figure 3.13.: Temperature dependent *dc* resistivity measurements for (a): LNO-RXO superlattices and for (b): PNO-PAO superlattices, determined by the Van der Pauw method.

the temperature dependent *dc* resistivity (in units of $\Omega \cdot m$) of LNO-RXO superlattices. The resistivity is calculated by taking the LNO layer thickness as approximately half of the total thickness D obtained from x-ray diffraction, assuming that the conductivity is determined by the "metallic" LNO layers. A careful reader may notice that some of the superlattices show a minimum in resistivity followed by a small upturn at low temperatures ($T < 30\,\mathrm{K}$). This minimum resistivity may be related to quantum interference due to electron-electron interaction and weak localization [39, 80] or magnetic scattering related to the Kondo effect [91].

Similarly, Fig. 3.13(b) represents the temperature dependent *dc* resistivity of PNO-PAO superlattices grown on substrates that induce different tensile and compressive strain. The superlattices under tensile strain (grown on STO and LSAT substrates) show a metal-insulator transition, whereas this behavior is suppressed for the PNO-PAO superlattice deposited on a compressive strain inducing LSAO substrate. The hysteresis indicates a first order transition as discussed in Ref. [60].

4. Orbital reflectometry on $LaNiO_3$-based heterostructures

In this chapter, we report a combined analysis of x-ray absorption and resonant reflectivity data designed to obtain the orbital polarization profiles of LNO-based superlattices with (4 u.c.//4 u.c.) stacking sequence. This superlattice geometry allowed us to partly separate the influence of epitaxial strain from interfacial effects controlled by the chemical composition of the insulating blocking layers. Our quantitative analysis revealed orbital polarizations up to 25%. We further show that strain is the most effective control parameter, whereas the influence of the chemical composition of the blocking layers is comparatively small.

Since our *dc* resistivity measurements show that superlattices with 4 u.c.-thick LNO layer stacks exhibit a metallic temperature dependence, we conclude that this do not exhibit any temperature-induced changes of the electronic and magnetic structure (Fig. 3.13, the same as prior studies in Refs. [14, 33]), we present room-temperature data.

4.1. X-ray linear dichroism

We first discuss the Ni L edge XAS data shown in Fig. 4.1. Except for the LNO-LAO on LSAO superlattice (Fig. 4.1(a)), the spectra of all superlattices clearly show a polarization dependence, which we attribute to natural linear dichroism. The magnitude of the observed dichroism varies substantially between superlattices of different composition and can be clearly seen in the normalized difference spectra (lower panels in Fig. 4.1(a-f)). In particular we point out that the observed dichroism in LNO-RScO superlattices is substantial, having in mind that even in the case of full x^2-y^2 orbital polarization in the atomic limit the integrated intensity of the spectrum for x polarization is about 60% of that of the z polarization. [1] Although the spectra obtained in

---

[1] Compared to cuprates with only one hole and an almost 100% difference between the intensity for x and z polarized light, in nickelates with 3 holes, even in the case of full $d_{x^2-y^2}$ orbital polarization, the intensity of the spectrum for x polarization is about 60% of that of the z polarization.

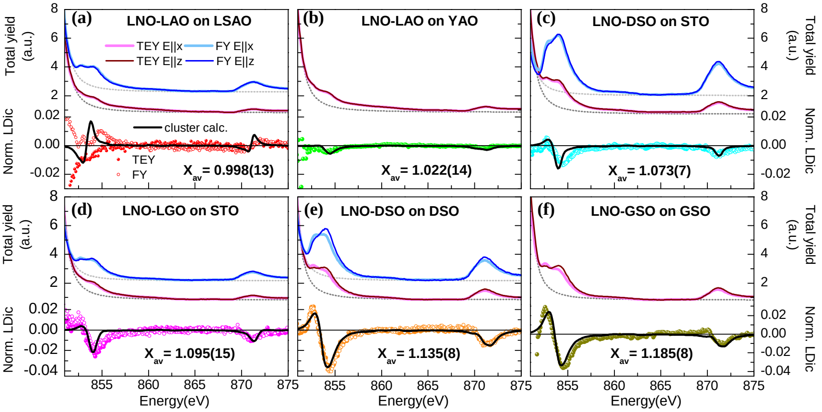

Figure 4.1.: XAS spectra (FY shifted by +1.5 for clarity) measured with linearly polarized light. Dotted grey lines show the results of Lorentzian fits to the tail of the La M_4 lines. The normalized difference spectra $(I_x(E)\text{-}I_z(E))/(\frac{1}{3}(2I_x + I_z))$ are shown directly below the corresponding spectra, together with the results of the cluster calculation. (a) LNO-LAO on LSAO; (b) LNO-LAO on YAO, (c) LNO-LAO on STO (Ref. [8]), (d) LNO-DSO on STO, (e) LNO-LGO on STO, (f) LNO-DSO on DSO , and (g) LNO-GSO on GSO .

TEY and FY detection modes differ in spectral weight and line shape, their polarization dependency agree remarkably well (lower panels in Fig. 4.1(a-f)). This confirms that the observed linear dichroism is robust and not related to surface effects.

In order to quantitatively analyze the observed dichroism, we applied the sum rule for linear dichroism [8, 139], which relates the ratio of holes in the Ni e_g orbitals to the energy-integrated XAS intensities across the Ni L-edge $I_{x,z} = \int_{L_{3,2}} I_{x,z}(E)dE$ for photons with in-plane (x) and out-of-plane (z) polarization, respectively:

$$X = \frac{h_{3z^2-r^2}}{h_{x^2-y^2}} = \frac{3I_z}{4I_x - I_z}. \tag{4.1}$$

Here $h_{x^2-y^2}$ and $h_{3z^2-r^2}$ are the hole occupation numbers of orbitals with $x^2 - y^2$ and $3z^2 - r^2$ symmetry.

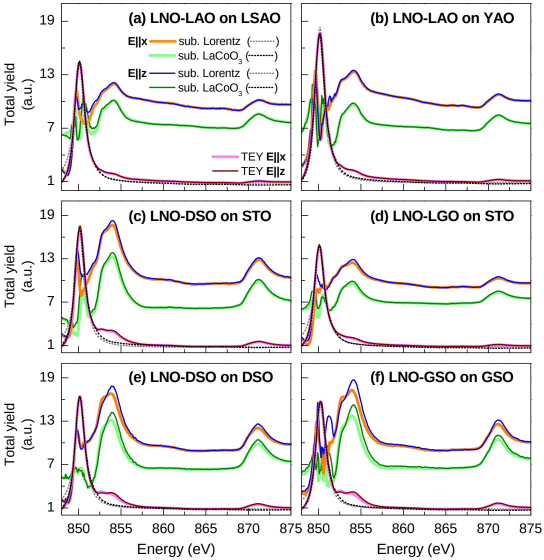

Figure 4.2.: Absorption spectra (TEY) measured with linear polarized light before and after the subtraction of the La M_4 line for all superlattices (see the labels in panel (a)-(f)). The dotted grey line is a Lorentzian fit to La M_4 line and the black dotted line shows a measured reference XAS spectrum of a $LaCoO_3$ thin film. The XAS spectra after subtraction are enlarged by a factor of 5 and shifted by +6 (subtraction of La M_4 lines from $LaCoO_3$) and +9 (subtraction of the Lorentzian fits of La M_4 lines) for clarify.

Before proceeding to describe the analysis of the linear dichroism, we add a remark about data processing. Since the La M_4 line partially overlaps the Ni L_3 contribution, it has to be subtracted before integrating the Ni XAS spectra. We carefully estimated the error associated with this subtraction. The results presented in the following were obtained by subtracting Lorentzian line shapes from the TEY and FY data (dashed lines in Fig. 4.1). Because there is a substantial difference in the La M edge line shape measured in TEY and FY, different Lorentzians were subtracted from these spectra. Note, however, that there is no linear dichroism at the La M-edge, so that identical Lorentzians can be subtracted for light polarization parallel to x and z. To further crosscheck our results, we compared the sum rule results obtained by

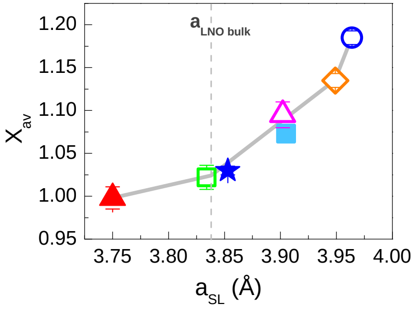

Figure 4.3: Hole ratio $X_{\rm av}$ obtained via the sum rule Eq. 4.1 vs the in-plane lattice constant $a_{\rm SL}$ of LNO-LAO on LSAO (▲), LNO-LAO on YAO (□), LNO-LAO on STO (Ref. [8]; ★), LNO-DSO on STO (■), LNO-LGO on STO (△), LNO-DSO on DSO (◇), and LNO-GSO on GSO (○).

integrating across the Ni $L_{3,2}$ lines with those obtained by integrating only across the Ni L_2 region, which is not affected by the La M_4-line subtraction. Again we found that both results are identical within the given error bars. In addition the La M_4 contribution has been subtracted using a TEY reference spectrum measured on a LaCoO$_3$ film, in which the La lines are well separated (Fig. 4.2). In conclusion, we found that the error made by these different subtractions is small and lies within the error bars.

In this way, the spatially averaged hole ratio $X_{\rm av}$ was calculated from the average of values determined from the sum rule analysis of TEY and FY XAS data. This quantity is shown in each panel of Fig. 4.1(a)-(f). In Fig. 4.3, we show $X_{\rm av}$ as a function of the measured in-plane lattice parameter $a_{\rm SL}$ (see structural characterization Fig. 3.5 in Sec. 3.3.2). $X_{\rm av}$ increases monotonically with increasing $a_{\rm SL}$. We will further discuss this hereafter.

4.2. Resonant x-ray reflectivity and constant q_z measurements

In an effort to elucidate the influences of strain and interfacial chemistry on the orbital occupation, we have determined layer-resolved profiles inside the LNO block. For this purpose, the intensity of the specularly reflected beam was measured as a function of momentum transfer (q_z) and photon energy.

The principle of layer-resolved orbital reflectometry is summarized as follows. According to the optical theorem, the x-ray absorption intensity is proportional to the imaginary part of the scattering factor, for instance, in superlattices with four unit cell LNO with outer layers B and inner layers A (inset of Fig. 4.11), the absorption intensity I_{XAS} is expressed as:

$$\begin{aligned} I_{XAS} &\propto \mathrm{I_m}|\varepsilon^{*}\sigma\varepsilon| \\ &= \frac{1}{\omega}\,\mathrm{I_m}|\varepsilon^{*}(f_A + f_B)\varepsilon|. \end{aligned} \tag{4.2}$$

As mentioned before, the hole ratio of the averaged four unit cell of LNO layers can be obtained from the polarization dependent linear dichroism. This analysis of the scattering intensity allows to determine a layer resolved orbital profile.

In the first step of our analysis, a structural model was obtained from fits of models in Parratt's recursive approach with nine independent parameters (as illustrated in Fig. 4.4) to the q_z-dependent non-resonant reflectivity using the reflectivity fitting tool REMAGX [90]. To improve the fits,we allowed the layer directly adjacent to the substrate and the top layer at the surface to

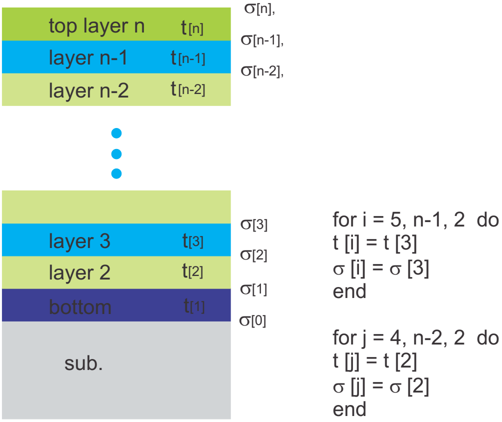

```
for i = 5, n-1, 2  do
t [i] = t [3]
σ [i] = σ [3]
end

for j = 4, n-2, 2  do
t [j] = t [2]
σ [j] = σ [2]
end
```

Figure 4.4.: Illustration of the structural fitting parameters of LNO-RXO superlattices using Parratt's recursive approach. There are nine independent parameters in total, i.e. substrate roughness $\sigma[0]$ with thickness ∞, the bottom layer 1 with roughness $\sigma[1]$ and thickness $t[1]$, the top layer n with different $\sigma[n]$, $t[n]$, as well as $\sigma[2]$, $t[2]$ for layer 2 and $\sigma[3]$, $t[3]$ for layer 3. The fitting parameters of the rest layers are synchronized to layer 2 and layer 3 via the script given on the right, which is executed individually for every data point.

have different thickness and roughness. Within the error, for all superlattices, our fits confirm the expected (4 u.c.//4 u.c.) structure with interface roughnesses around 1 u.c. (see Tab. 4.1). The individual layer thickness as well as the roughness are summarized in Tab. 4.1. In the following, the structural parameters were fixed for the simulation of the dichroic reflectivity. While for all other superlattices we used the measured linearly polarized XAS data to construct the optical constants, for the LNO-LAO on LSAO superlattice, these data were not available since $P_{\mathrm{av}} \sim 0$. In order to construct the optical constant, we add the difference from cluster calculations to the averaged experimental XAS data, i.e. XAS + $\frac{1}{2}$LDic for x and XAS - $\frac{1}{2}$LDic for z polarized light, respectively. The results of fits to the non-resonant ($E = 8048\,eV$) and resonant (Ni L_2) q_z-dependent reflectivity data are shown in Fig. 4.5.

The constant q_z measurements is performed with fixed momentum transfer along the specular direction by varying the incident beam energy as well as the scattering angle simultaneously. A careful selection of the momentum transfer q_z can make the total scattering factor quite sensitive to the local charge scattering or magnetic scattering. For instance, for the superlattice structure of (4 u.c.//4 u.c.) LNO-RXO investigated here, the scattering factor close to $SL(002)$ peak reflected from such a symmetric superlattice is sensitive to modulations within the LNO layer stack [8]: $F_{002} = \sum_i f_i \exp(iq_z) = (1-i)(f_B - f_A)$ (Eq. 2.32).

Fig. 4.6 shows the energy- and polarization-dependent resonant reflectivity of various samples with fixed momentum transfer q_z close to the (002) superlattice reflex. Note that the actual q_z values given in the caption of Fig. 4.5 vary slightly for the different superlattices because of their (small) structural differences. Using the numerical routines [90], we computed the normalized dichroic difference spectra for models with different orbital occupation in the inner layers A and outer layers B based on the Matrix formulism. The charge anisotropy for outer and inner layer is introduced by a tetragonal tensor with the form:

$$\varepsilon_{\mathbf{A(B)}} = \begin{pmatrix} \varepsilon^{xx}_{A(B)} & 0 & 0 \\ 0 & \varepsilon^{xx}_{A(B)} & 0 \\ 0 & 0 & \varepsilon^{zz}_{A(B)} \end{pmatrix}.$$

The modulation is parameterized by:

$$(\varepsilon_{A(B)})^{jj} = (1 \mp \alpha)\varepsilon^{jj} \pm \alpha\varepsilon_{cubic}, (jj = xx, zz), \alpha \in [0,1] \tag{4.3}$$

with $\varepsilon_{cubic} = 1/3(2\varepsilon^{xx} + \varepsilon^{zz})$ denotes the cubic case. In order to model the constant q_z scan, we varied α between 0 and 1 to change the dielectric con-

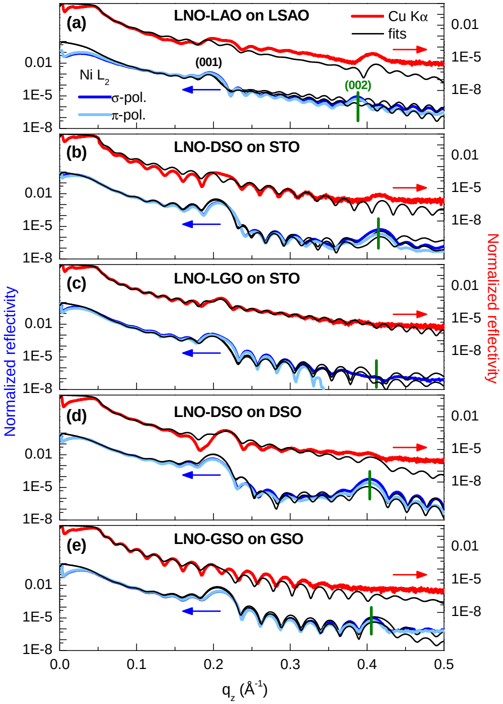

Figure 4.5.: Reflectivity as a function of q_z for the (a) LNO-LAO on LSAO, (b) LNO-DSO on STO, (c) LNO-LGO on STO, (d) LNO-DSO on DSO, and (e) LNO-GSO on GSO superlattice. The q_z values at (002), chosen for the constant-q_z shown in Fig. 4.6, are marked by green vertical lines and correspond to values of (a) 0.3880 Å^{-1}, (b) 0.4146 Å^{-1}, (c) 0.4120 Å^{-1}, (d) 0.4035 Å^{-1}, (e) 0.4055 Å^{-1}.

stants of layers A and B, i.e. the relative orbital occupation of layer A and B. We changed the different input files of the optical constant until we found the best agreement with the normalized different spectra from constant q_z measurements, with the constraint that the total hole ratio measured by XAS is constant. Taking the example of LNO-DSO superlattice grown on DSO substrate with $X_{\mathrm{av}} = 1.135$ and assume $\alpha = 0$. In this case, there is no difference between layer A and B, i.e. a homogenous distribution across all LNO layers with a preferred hole occupation of the $d_{3z^2-r^2}$ orbital. Our result $\alpha = 0.15$ ob-

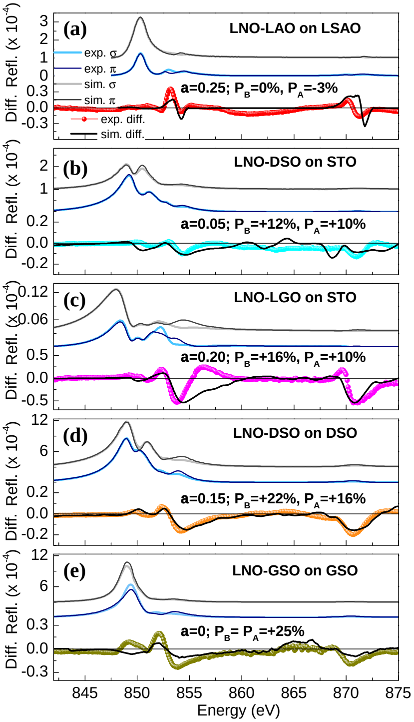

Figure 4.6.: Experimental and simulated constant-q_z energy scans at the (002) superlattice peak of (a) LNO-LAO on LSAO, (b) LNO-DSO on STO, (c) LNO-LGO on STO, (d) LNO-DSO on DSO, and (e) LNO-GSO on GSO. The experimentally obtained normalized difference $(I_\sigma(E)\text{-}I_\pi(E))/(I_\sigma(E)+I_\pi(E))$ is shown directly below the corresponding spectrum together with the simulated one. The obtained layer-resolved orbital polarizations within the LNO layer stack, P_B (interface layer) and P_A (inner layers), are stated in each panel.

tained from the reflectivity simulation yields $X_\mathrm{B} = X_\mathrm{av} + (1+\alpha)(X_\mathrm{av}\text{-}1) = 1.155$ and $X_\mathrm{A} = X_\mathrm{av} + (1\text{-}\alpha)(X_\mathrm{av}\text{-}1) = 1.115$. It is obvious that the extreme case of $\alpha = 1$ results in $X_\mathrm{B} = 1.27$ and $X_\mathrm{A} = 1$, implying that the dichroism arises from the interface B layers only. The variation of the optical constant β profiles with different modulation parameter α is shown in Fig. 4.7. The dark black

Composition	Sub.	structure (u.c.)	α	$\mathbf{P}_{\text{av}}$ (%)
LNO-LAO	$\text{LSAO}_{0.5}$	$4.4_{0.7}[(4.1_{0.6}/4.2_{0.7})\text{x}9]4.7_{0.8}$	0.25	$\mathbf{0 \pm 2}$
LNO-LAO	YAO	(4//4)x8		$\mathbf{3 \pm 2}$
LNO-DSO	$\text{STO}_{0.8}$	$5.0_{0.8}[(3.9_{1.3}/4.0_{1.7})\text{x}7]3.4_{1.3}$	0.05	$\mathbf{10 \pm 1}$
LNO-LGO	$\text{STO}_{0.6}$	$4.0_{0.5}[(4.0_{0.9}/4.2_{0.8})\text{x}7]5.1_{1.6}$	0.20	$\mathbf{12 \pm 2}$
LNO-DSO	$\text{DSO}_{0.6}$	$4.7_{1.4}[(4.2_{1.4}/3.9_{0.7})\text{x}7]3.6_{1.3}$	0.15	$\mathbf{19 \pm 1}$
LNO-GSO	$\text{GSO}_{0.8}$	$3.7_{0.6}[(4.0_{0.6}/3.9_{0.8})\text{x}7]4.4_{1.2}$	0	$\mathbf{25 \pm 2}$

Table 4.1.: Superlattice composition and structure, substrate material, the modulation α from dichroic reflectivity modeling and the averaged orbital polarizations of the investigated nickel oxide heterostructures. The superlattice structure obtained from fits to the reflectivity (see text) is given in the following nomenclature: $d_\sigma^{LNObottom}[(d_\sigma^{LNO}/d_\sigma^{RXO})\text{xM}]d_\sigma^{RXOtop}$ with thickness d and roughness σ in u.c. calculated by dividing with c_{SL}. The roughness of the substrate is given in the corresponding column as an index, i.e. $R\text{XO}_\sigma$. For the LNO-LAO on YAO no reflectivity measurements were performed.

line corresponds to cubic symmetry. As a consequence of an increasing modulation α for z-polarized light, β of layer A is decreasing and increasing for layer B. The opposite case occurs for x-polarized light, resulting in a small linear dichroism of layer A and a large linear dichroism of layer B. The values of the modulation α for different samples are given in each panel of Fig. 4.6 (also summarized in Tab. 4.1).

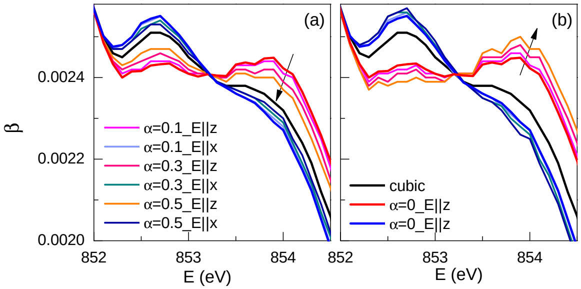

Figure 4.7.: The varying of the imaginary part β of a refraction index with different modulation α for (a) layer A and (b) layer B in different polarization.

4.3. Discussion

4.3.1. Linear orbital-lattice coupling

XAS is a well-established technique for studying the unoccupied site- and symmetry-projected electronic density of states of solids, providing the possibility to compare experimental results with single-particle band-structure calculations, often obtained using DFT. In the past, it was demonstrated that for a satisfactory description of the observed fine structure of transition-metal L-edges, it is important to include many-body effects, in particular the interaction of the $2p$ core hole created in the absorption process with electrons in the partially filled $3d$ final state. For rather localized electrons (insulating material), a reasonable description can be obtained by a cluster calculation based on many body configuration interaction, which takes into account the full multiplet effects [26].

Hence, as a further step in the analysis of the spectroscopic data, we per-

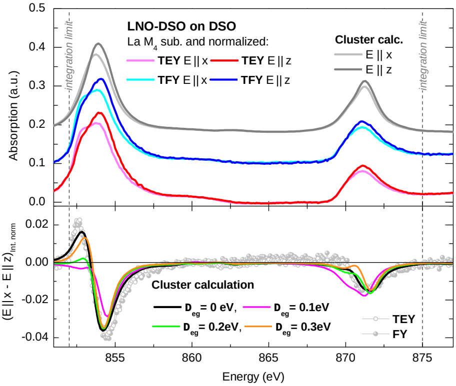

Figure 4.8.: (Top) Polarization-dependent XAS spectra (TEY and FY) after subtraction of the La M_4 line (Lorentzian fit) together with the spectra obtained from our cluster calculation ($\gamma = 0.6$, $\delta = 0.4$, and $\Delta e_g = 300\,meV$). All spectra are normalized by their polarization-averaged integral [$A = (2I_x + I_z)/3$]. (Bottom) Normalized difference spectra [$I_x(E)$-$I_z(E)$]$/A$. The results of the cluster calculation are shown for $\gamma = 0.6$, $\delta = 0.4$, and different values of Δe_g, ranging from 0 to 300 meV.

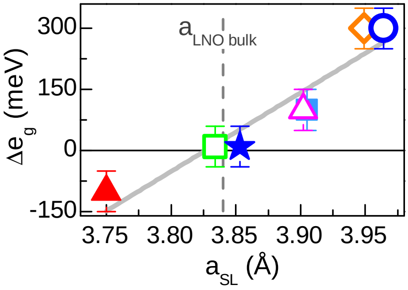

Figure 4.9: Crystal field splitting Δe_g obtained from the cluster calculation vs the in-plane lattice constant a_{SL} of LNO-LAO on LSAO (▲), LNO-LAO on YAO (□), LNO-LAO on STO (Ref. [8]; ★), LNO-DSO on STO (■), LNO-LGO on STO (△), LNO-DSO on DSO (◇), and LNO-GSO on GSO (○).

formed a cluster calculation for a Ni $3d^7$ ion in a tetragonal ligand field of six oxygen ions, in which both the orbital polarization and the energy difference between the Ni e_g orbitals, Δe_g, were adjusted to maximize agreement with the dichroic difference spectra. Additional parameters are radial integrals, Slater integrals, and spin-orbit coupling constants, which were obtained by atomic Hartree-Fock calculations, as well as $10Dq$, the hybridization strength $pd\sigma$ and $pd\pi$, and the charge-transfer energy Δ_{3+}. These parameters used for the cluster calculations are summarized in Tab. 2.1. The measured spectra were then described as linear superpositions of spectra, $I_{x,z}^{x^2-y^2}(E)$, $I_{x,z}^{3z^2-r^2}(E)$ calculated for 100% occupation of either the x^2-y^2 or the $3z^2-r^2$ orbital and for polarization of the incoming light parallel to the x and z directions, respectively. For instance, the absorption spectra for z-polarized light is obtained by $I_z(E) = \gamma I_z^{x^2-y^2}(E) + \delta I_z^{3z^2-r^2}(E)$. The admixture coefficients (γ and δ with $\gamma+\delta=1$) and Δe_g were then varied until the best agreement with the experimental linear-dichroic difference spectra was found. As shown in the bottom panel of Fig. 4.8, the derivative-like up-and-down line shape in the normalized different curve of LNO-DSO superlattice grown on DSO substrate can only be reproduced by increasing the crystal field splitting Δe_g.

Since the cluster calculation is a local approach and the LNO layers in all superlattices studied here are metallic, it is not surprising that the line shapes of the spectra are not exactly reproduced (see Fig. 4.8 and the discussion in Ref. [8]). We emphasize, however, that the normalized dichroic difference spectra $[I_x(E)\text{-}I_z(E)]/A$ ($[A=(2I_x+I_z)/3]$) are almost independent of the individual line shape and describe our experimental data very well (see Fig. 4.1). While a preferred orbital occupation of one of the e_g orbitals is seen as an intensity difference between $I_x(E)$ and $I_z(E)$ spectra, the effect of the crystal-field splitting manifests itself as an energy shift between these spectra, which results in a derivative-like line shape of the difference spectra (lower panels in Figs. 4.1(a)-(f)). At this point, we emphasize that for the determination of orbital polarizations from energy integrals of the XAS spectra across the full Ni L-edge via Eq. 4.1, a detailed understanding of the XAS fine structure is not necessary. While the effect of the core hole potential enters the Hamiltonian of the system, the sum rule is independent of it, and therefore X_{av} reflects the polarization dependence of the d-projected unoccupied density of states.

The variation of Δe_g as a function of the measured in-plane lattice constant a_{SL} Fig. 4.9 is consistent with the behavior of X_{av} (see Fig. 4.3). Whereas the value for the LNO-LAO superlattice under compressive strain ($\Delta e_g \approx$-$100\,meV$) agrees with the one reported earlier for a similar sample [19, 36], we see a comparable shift also for tensile strain with a roughly linear dependence of Δe_g on a_{SL} based on a large number of samples. Our results clearly indicate an approximately linear orbital-lattice coupling, and confirm the stabilization of the planar $d_{x^2-y^2}$ orbital under tensile strain, which will be discussed in detail below. This result differs from the previously reported asymmetry between the behavior under tensile and compressive strain of ultrathin LNO thin film [19] and LNO-based superlattices [36], at least in the (4 u.c.//4 u.c.) superlattice structures investigated here.

4.3.2. Orbital polarization

Before comparing our experimental results with density functional theory (DFT) predictions, let us first have a brief literature review of the theoretical calculations made for nickel oxide heterostructures. The nominally Ni^{3+} ions in bulk LNO adopt the electron configuration $t_{2g}^6 e_g^1$, and initial analytical calculations indicated a single Fermi surface with dominant $d_{x^2-y^2}$ character for the e_g electrons in suitably prepared nickel oxide superlattices. The shape of this Fermi surface was predicted to resemble the one of the cuprate superconductors, raising hopes for "engineered" high-temperature superconductivity [53]. Subsequent calculations based on DFT addressed the influence of confinement, strain, structural distortions, chemical composition of the insulating layers, and electronic correlations on the orbital polarization of the Ni e_g electron, with widely divergent results [11, 48, 49, 51, 52]. Whereas some DFT calculations supported original predictions, Han *et al.* [49] later reported that the combined effect of the on-site Hund interaction and the covalency of the nickel-oxygen bond greatly reduces the orbital polarization, so that the orbital degeneracy retains its dominant influence on the electronic structure of the nickel oxides, even under the most favorable conditions. This conclusion received support from x-ray absorption spectroscopy (XAS) studies of ultra-thin LNO films [19] and superlattices [36]. Whereas films under compressive strain showed a slightly enhanced occupation of the $d_{3z^2-r^2}$ orbital, XAS data for films under tensile strain were interpreted as evidence of a charge-ordering instability with negligible orbital polarization.

In order to compare our experimental results with the DFT predictions mentioned above,we define the orbital polarization following Refs. [48] and [49] and using Eq. 4.1

$$P = \frac{n_{x^2-y^2} - n_{3z^2-r^2}}{n_{x^2-y^2} + n_{3z^2-r^2}} = \left(\frac{4}{n_{e_g}} - 1\right)\frac{(X-1)}{(X+1)}, \tag{4.4}$$

where $n_{x^2-y^2}$ and $n_{3z^2-r^2}$ denote the numbers of electrons in orbitals of x^2-y^2

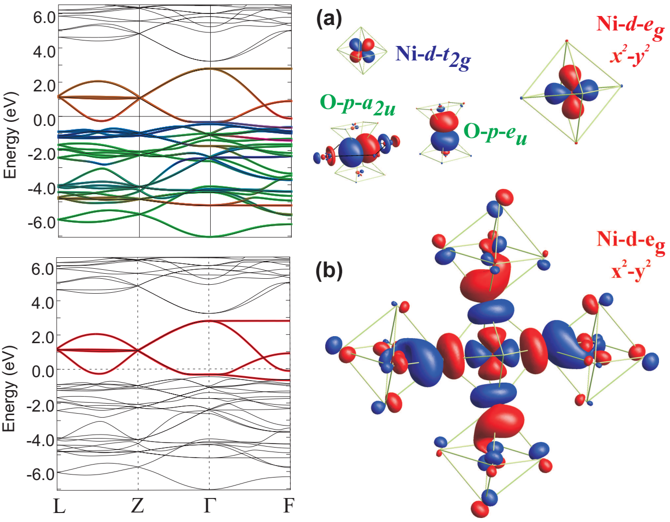

Figure 4.10.: Band structure (left) and Wannier orbitals (right) of bulk LNO (space group R$\bar{3}$c [40]): (a) down-folded to atomic Ni d and O p orbitals and (b) down-folded to extended Ni-**d**-e$_g$ orbitals, explicitly including covalency. The difference in phase of the wave functions is depicted by red and blue colors. The color coding for the band structure is as follows: red corresponds to Ni e_g, blue to Ni t_{2g} and green to O p character of the bands. The calculations were done using the Stuttgart-NMTO code [4, 5].

and $3z^2$-r^2 symmetry. The prefactor in Eq. 4.4 depends on the total number of e_g electrons, n_{e_g}, and deserves particular attention, since hybridization between Ni d and O p is not negligible and can be affected by strain and the composition of the insulating material. In order to calculate P of the local, atomic-like Ni d orbitals for all different superlattices, the value of $n_{e_g}^{atomic}$ has to be known. Theoretical values show fairly large variations of $n_{e_g}^{atomic} = 1.5$-2.1 as a function of composition and interactions [48, 50], but an experimental determination is a difficult task. Here, we suggest to consider the orbital polarization of extended Wannier orbitals in order to provide a well-defined quantitative description for the discussion and comparison of superlattices with possibly different hybridization. The orbital polarization of those extended Wannier orbitals is obtained via Eq. 4.4 using $n_{e_g} = 1$ for all superlattices studied.

To illustrate the different wave functions, we performed DFT calculations using the experimentally reported crystal structure of bulk LNO [40] (for details see Ref. [57]).We considered two cases: (i) a large basis of five atomic-like Ni d and three O p orbitals with $n_{e_g}^{atomic} = 1.8$ due to hybridization (top panel in Fig. 4.10) and (ii) a small basis of extended Wannier orbitals, labeled with $\mathbf{d}$, representing the antibonding Ni e_g and O p states near the Fermi level with $n_{e_g} = 1$ (bottom panel in Fig. 4.10). The latter orbitals are very close to the band eigenstates and reflect the covalency due to their large weight at the oxygen positions, but exhibit the full symmetry of the e_g orbitals. Describing our results using this basis functions does not require the knowledge of the strain and composition dependent values $n_{e_g}^{atomic}$, since the differences in hybridization are reflected in a local change of the Wannier functions. Furthermore, a similar orbital basis set was used to calculate orbital polarizations in Refs. [53], [48], and [49], i.e. only bands spanning a small energy window close to the Fermi level were integrated to obtain the corresponding occupation numbers $n_{x^2-y^2}$ and $n_{3z^2-r^2}$ (-3 and -1.5 eV to $E_{\mathrm{F}} = 0$ in Refs. [49] and [48], respectively). A detailed inspection of the revised results [50] of Ref. [49] indicates that the Fermi surface properties, in particular, the size of the central Fermi surface patch, is reflected in $P_{3\to 0}$ (extended Wannier orbitals) rather than in $P_{-\infty\to 0}$ (atomic like orbitals). While the values of $P_{3\to 0}$ are materially different for the interacting cases (23-37%, large central patch) compared to the noninteracting case (50%; very small central patch), the values for $P_{-\infty\to 0}$ fall into a fairly narrow range of 11-17% for all cases. Note that, the total number of these states is $n_{e_g} \approx 1$ and therefore comparable to our experimental results on an absolute scale. For all superlattices, we obtain positive values in the range $P_{\mathrm{av}} = 25\%$ for the spatially averaged orbital polarization, corresponding to a substantially enhanced occupancy of the orbital with x^2-y^2 symmetry.

As mentioned above, discrepancy exists from previous LDA+DMFT studies, which is mainly related to the treatment of the hybridization with O p orbitals [49, 52, 53]. Parragh *et al.* reconsidered the existing LDA+DMFT studies at a model level, and pointed out the crucial role of d electron occupation n_{e_g} in understanding the contradict. The different filling in the d-only model ($n_{e_g} = 1$) and in the dp-model ($n_{e_g} = 1.7$) leads to differences for the ground state correlations. In the d-only model, the crystal field splitting provides a preferred $d_{x^2-y^2}$ orbital occupancy similar to the Fermi surface topology as cuprates. Whereas in the latter case, the Hund's coupling favors, resulting in a strong local moment and a small orbital polarization P. Moreover, Peil *et al.* presented the LDA+DMFT calculations taking both the structural distortions and the electronic correlations recently, where the orbital polarizations P are in good agreement with our experiment results quantitatively, i.e. a stabilization of the planar $d_{x^2-y^2}$ orbital under tensile strain [111].

4.3.3. Layer resolved orbital polarization

Fig. 4.11 provides a synopsis of the orbital polarizations P_{av}, P_{A}, and P_{B} as a function of a_{SL}. Note that the hole ratio X_{av} plotted in Fig. 4.3 is linearly related to P_{av} over the range investigated here, and within the given error bars. The polarization P_{A} of the inner layers, which is less strongly affected by interfacial effects, depends linearly on a_{SL} over the entire measured range, including both the samples under tensile strain and the compressively strained LNO-LAO superlattice on LSAO, where P_{A} is negative corresponding to an enhanced occupation of the $d_{3z^2-r^2}$ orbital. The fitted straight line crosses zero around $a_{\mathrm{SL}} = 3.79$ Å, slightly below the pseudocubic bulk lattice constant of LNO of 3.838 Å. We attribute this shift to the effect of confinement, yielding a slightly preferred $x^2 - y^2$ occupation even for the inner layers (i.e. a small positive value of P_{A}). The strain dependence of both the energy splitting Δe_g extracted from the cluster model discussed above and P_{A} determined by orbital reflectometry thus indicate a simple linear orbital-lattice coupling.

Whereas strain alone induces orbital polarizations of up to $P_{\mathrm{A}} \sim 25\%$, the additional enhancement of the polarization in the outer LNO layers generated by interfacial effects falls into a comparatively narrow band of width $\sim 5\%$ (grey area in Fig. 4.11). According to the DFT predictions [48, 49, 53], the orbital polarization at the LNO-RXO interface is strongly influenced by the dimensional confinement of the conduction electrons and by the chemical composition of the blocking layers. The effect of confinement is expected to be

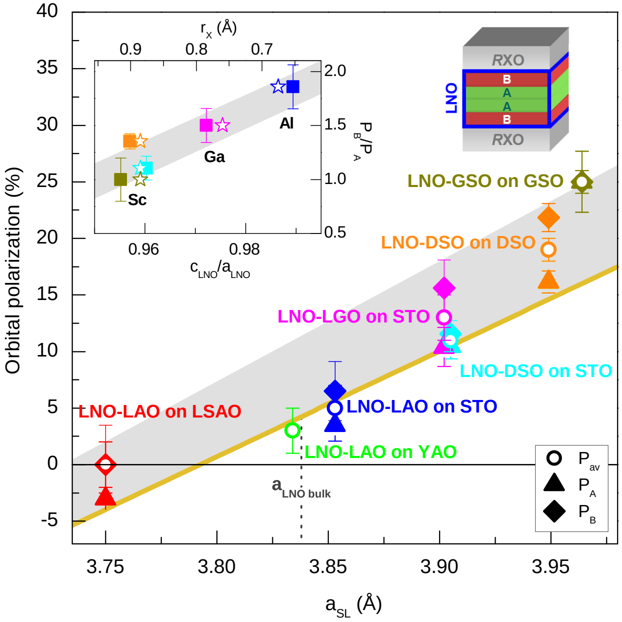

Figure 4.11.: Averaged (P_{av}) and layer-resolved (P_A, P_B) orbital polarizations obtained from the combined analysis of XAS and reflectivity as a function of the in-plane lattice constant a_{SL} measured by x-ray diffraction. The data for LNO-LAO on STO is obtained from Ref. [8]. Inset: ratio P_B/P_A vs. the lattice constant ratio $\mathrm{c}_{LNO}/\mathrm{a}_{LNO}$ (full squares) with $c_{LNO} = 2\, c_{SL}$-c_{RXO} and $a_{LNO} = a_{SL}$ and vs. the size of the X cation r_x (Ref. [22]; open stars) for superlattices under tensile strain. The c-axis lattice parameter of RXO was obtained from Poisson ratio: $c_{RXO} = \frac{2\nu}{\nu-1}(a_{SL} - a_{RXO}^{bulk}) + a_{RXO}^{bulk}$ using $\nu = 0.26$ [125].

similar in all of our superlattices, because the blocking layers have identical thicknesses (4 u.c.) and similar band gaps. The effect of chemical composition is due to the hybridization between the Ni $d_{3z^2-r^2}$ and the O p_z orbital of the apical oxygen at the interface, which in turn depends on the hybridization between the s-symmetry orbital of the X ion with the O-p_z states. The hybridization parameters are difficult to determine experimentally, but Han *et al.*

[48] pointed out a close relationship between these quantities and parameters characterizing the lattice structure, including especially the O-X bond length, which is controlled by the size of the X cation, r_{X}. Specifically, for large r_{X} (large O-X distances) the X s - O p_z hybridization is expected to be reduced, and the Ni $d_{3z^2-r^2}$ - O p_z hybridization correspondingly enhanced, resulting in a larger enhancement of the orbital polarization at the interface, and vice versa. We have therefore plotted the ratio $P_{\mathrm{B}}/P_{\mathrm{A}}$ (which is a measure of the modulation of orbital polarization within the LNO layer stack) as a function of the lattice parameter ratio $c_{\mathrm{LNO}}/a_{\mathrm{LNO}}$ (inset of Fig. 4.11), which is approximately proportional to r_{X} (top axis in the inset of Fig. 4.11). The resulting trend of reduced interfacial enhancement of P for smaller r_{X} is opposite to the trend predicted by the DFT calculations [48, 146]. A full crystallographic determination of the Ni-O and O-X distances and the Ni-O-X bond angle as well as corresponding DFT calculations are required to elucidate the origin of this discrepancy. Peil *et al.* presented the effect of octahedral distortion on orbital polarization based on GGA+DMFT calculations for LNO films on different substrates. The octahedral tilts result in a nonlinear response of the orbital polarization to external strain effect. In addition, the enhancement of orbital polarization in the distorted structure compared to the tetragonal case without distortions is related to different hybridization between e_g and t_{2g} states, which gives rise to different band structures.

4.4. The effect of different R cations

As discussed above, the orbital occupation in LNO-RXO heterostructures depends on the dimensionality, the choice of the X ion and strain induced by the substrate [20, 48, 49, 51, 52, 53]. More precisely, the confinement is expected to reduce the band dispersion of the Ni-$d_{3z^2-r^2}$ states along the z-direction, the effect of the chemical ion X is to change the hybridization between the Ni $d_{3z^2-r^2}$ orbital and O $2p_z$ orbital, and strain does not directly lift up the Ni $d_{3z^2-r^2}$ orbital but modifies the bandwidth. The biaxial strain induces a difference between the in-plane and the apical Ni-O bond lengths, resulting in an enhancement of the e_g orbital splitting. The choice of the R ion may also play an important role, i.e. the R ion, such as Dy, La, Gd, essentially changes the Ni-O bond length and the corresponding hybridization as indicated from LDA calculations.

Fig. 4.12 shows the GGA+U (generalized gradient approximation, $U = 3\,eV$) calculation results for a LNO-DSO (4 u.c.//4 u.c.) superlattice on DSO sub-

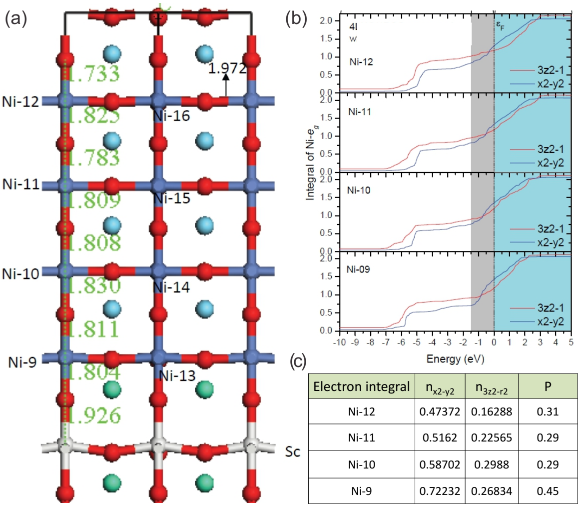

Electron integral	n_{x2-y2}	n_{3z2-r2}	P
Ni-12	0.47372	0.16288	0.31
Ni-11	0.5162	0.22565	0.29
Ni-10	0.58702	0.2988	0.29
Ni-9	0.72232	0.26834	0.45

Figure 4.12.: GGA+U calculation of the LNO-DSO (4 u.c.//4 u.c.) on DSO substrate ($U = 3\,eV$) without a consideration of the GdFeO$_3$ distortions. Panel (a): the optimized structure with an averaged unit cell volume conservation of the bulk LNO and the bulk DSO. The in-plane Ni-O bonds are set to 1.972 Å (fully strained to the DSO substrate). The apical Ni-O bond lengths are shown in the plot. Panel (b): integrated density of states of Ni $d_{3z^2-r^2}$ and $d_{x^2-y^2}$ orbitals. Panel (c): the calculated orbital polarization for each Ni ion which takes into account only the antibonding states near the Fermi level (from -1.5 eV to 0).

strate using the Vienna *ab*-initio simulation package (VASP) code.[2] The input structural parameters for DSO are $a = b = c = c_{pc} = 3.944$ Å [75]. In comparison with the GGA+U results of a LNO-LAO superlattice [8], the difference is that there is no mirror plane in the LNO-DSO superlattice, in particular, the Ni-9 connects with the DyO plane and the Ni-12 connects with the LaO plane (Fig. 4.12(a)). The structure optimization results in an oxygen buckling in the ScO$_2$ and DyO planes. The apical Ni-O bond distances are shown in panel (a). One can notice that there is a difference in apical Ni-O bond length between

---

[2] The GGA+U calculation results shown here were done by X.P. Yang, unpublished.

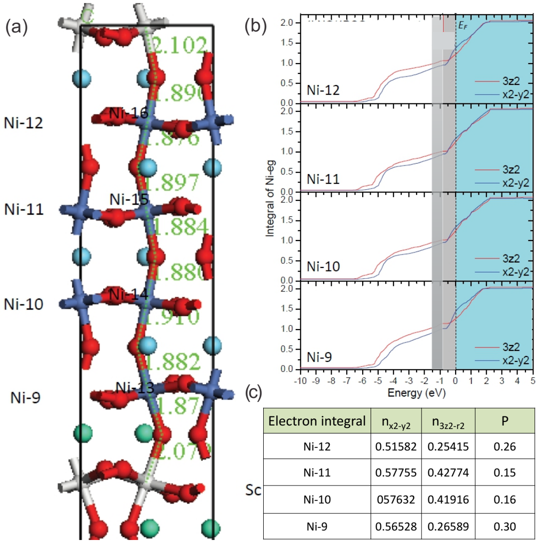

Electron integral	n_{x2-y2}	n_{3z2-r2}	P
Ni-12	0.51582	0.25415	0.26
Ni-11	0.57755	0.42774	0.15
Ni-10	057632	0.41916	0.16
Ni-9	0.56528	0.26589	0.30

Figure 4.13.: GGA+U calculation of the LNO-DSO (4 u.c.//4 u.c.) superlattice on DSO substrate with $U = 3\,eV$ taking into account the GdFeO$_3$ distortions. Panel (a): the optimized structure with an averaged volume conservation as well as the corresponding apical Ni-O bond lengths. Panel (b): integral of Ni $d_{3z^2-r^2}$ and $d_{x^2-y^2}$ density of states. Panel (c): the calculated orbital polarization for each Ni ion from -1.5 eV to E_f.

the two interface layers, i.e. Ni-9 and Ni-12, which affects the hybridization between Ni $d_{3z^2-r^2}$ and O $2p_z$ orbitals. In general, for a small apical Ni-O bond length, the Ni $d_{3z^2-r^2}$ - O p_z hybridization is expected to be enhanced, resulting in a preferred $d_{x^2-y^2}$ orbital, and vice versa. However, this cannot be simply applied here, since the bond lengths are quite different for the top and the bottom apical Ni-O bonds. Taking the octahedra of the Ni-12 ion for example, the top and bottom apical Ni-O bond lengths are 1.733 Å and 1.823 Å , respectively. As an estimate of the orbital polarization of each NiO$_6$ octahedron can be obtained by the relative change of the in-plane Ni-O/apical Ni-O bond length ratio. For instance, the apical Ni-O bonds in LNO-LAO (4 u.c.//4 u.c.) [8] are much larger than those in LAO-DSO (4 u.c.//4 u.c.), with a correspondingly smaller orbital polarization in the former case.

The orbital occupation is obtained by projecting the calculated electronic density of states to spheres. Technically, the sphere size is arbitrary and not well-defined. Here the VASP default values of the Wigner-Seitz radii were used (i.e. 1.286 Å for Ni d atomic orbitals and 0.820 Å for O p atomic orbitals), which provide a good estimation of the local charge and the local magnetic moment, etc. The integral of $d_{x^2-y^2}$ and $d_{3z^2-r^2}$ density of states as a function of energy are shown in Fig. 4.12(b). The orbital polarizations presented in panel (c) of Fig. 4.12 were calculated by integrating the antibonding states near the Fermi level (from -1.5 eV to E_f). The orbital polarization for Ni-12 ion is 31%, whereas a dramatic difference is observed for the Ni-9 ion with $P=45\%$. If such a difference exists, it would deserve an experimental confirmation.

On the other hand, bulk DSO exhibits an orthorhombic distortion. Fig. 4.13(a) shows the optimized structure taking into account the GdFeO$_3$ distortion. Once again the averaged unit cell volume of the bulk LNO and the bulk DSO is conserved in the calculation. Note that the O-Ni-O angle in the apical direction is almost 180° while the Ni-O-Ni angle deviates clearly from 180°, which leads to a stretched apical Ni-O bond compared to the case without GdFeO$_3$ distortion. The Sc with $3d$ outmost shell is quiet different from Al. Oxygen dimpling is very obvious in ScO$_2$ layer. When the NiO$_2$ mirror plane is avoided effectively, the dimpling of oxygen becomes more visible in energy, which strengthens the Jahn-Teller effect of the octahedra. Fig. 4.13(b) shows the integral of the Ni $d_{x^2-y^2}$ and $d_{3z^2-r^2}$ density of states and the corresponding orbital polarizations taking into account the anti-bonding states near E_f which are shown in panel (c). We notice that the orbital polarizations are smaller on average. Moreover, the difference arising from the Dy and La cations are partially canceled. Possibly this is related to the octahedra tilts, and the change of the Ni-O-Ni bond angle as well as the increased apical Ni-O bond length. The latter cause a reduced hybridization between Ni $d_{3z^2-r^2}$ and O $2p_z$ orbitals, i.e. the distortions cancel the non-symmetric interface effect due to interfacial Dy or La ions. However, the effect is nontrivial since the hybridization depends on a combined effect of the Ni-O and O-Sc distance and the Ni-O-Sc bond angle.

In summary, different cation ions R results in a change of orbital occupancies which may cause a big difference between the two outer LNO layers as suggested by the GGA+U calculation. This effect depends on how far the real structure deviates from the bulk environment. Note that for the LNO-RXO (4 u.c.//4 u.c.) superlattices, the scattering factor calculated for the $SL(002)$ reflection is not sensitive to the difference related to the cation R. In other words, for R = Dy, Gd, i.e. the LNO-DSO and the LNO-GSO superlattices, it is possible that the orbital polarizations of the top LNO layer (with the atomic form factor $f^{B'}_{LNO}$) and the bottom LNO layer (with the atomic form factor f^{B}_{LNO}) inside the LNO layer stack are different. An atomic sketch of the superlattice configuration shows that the top atomic NiO_2 layer is sandwiched between RO and LaO layer, whereas the bottom atomic NiO_2 layer is sandwiched by two LaO layers, or vice versa. We point out that our simulations based on $SL(002)$ diffraction index give equally good results for both models (BAAB and B′AAB), because the intensity for q_z around the (002) reflection is less sensitive to this interface difference (i.e. $f^{B'}_{LNO}$ - f^{B}_{LNO}) than to the difference between the outer and the inner layers, i.e. $f^{B'(B)}_{LNO}$ - f^{A}_{LNO}.

Luckily, it is possible to have a direct evaluation of the effect by carefully designing the superlattice configurations. For this purpose, two superlattices are studied:

(**a**) LNO-DSO (4 u.c.//4 u.c.) grown on DSO substrate;

(**b**) LNO-DSO (2 u.c.//4 u.c.) grown on DSO substrate.

The good sample qualities were confirmed by XRD measurement (*lscans* along the specular direction shown in Fig. 3.7 and the corresponding RSMs along the off-specular directions in Fig. 3.9 and Fig. 3.10). For sample (**a**), a direct confirmation of the cation R effect is to reach the $SL(004)$ reflex. Since the scattering factor of $SL(004)$ is only sensitive to the difference between the top and the bottom LNO layer, denoted as f^{B}_{LNO} and $f^{B'}_{LNO}$, i.e.

$$\begin{aligned} F_{(004)} &= \sum_i f_i \ \exp(iq_z \ z) \\ &= f^{B}_{LNO} - f^{A}_{LNO} + f^{A}_{LNO} - f^{B'}_{LNO} \\ &= f^{B}_{LNO} - f^{B'}_{LNO}. \end{aligned} \tag{4.5}$$

For sample (**b**), the scattering factor of the $SL(003)$ peak $F_{(003)}$ has the same form as the scattering factor of $F_{(004)}$ shown above (Eq. 4.4).

Prior to the experiments, let us have a simple estimation of the diffraction angle 2θ. For sample (**a**), (4u.c.//4u.c.) LNO-DSO superlattice (the same structure as that used in GGA+U calculations), the bilayer thickness is approximately:

$d_{\text{bilayer}} = (8 \times \frac{3.838+3.944}{2})$ Å $= 31.13$ Å,

from which a value $q_z \approx 0.8073$ Å^{-1} is estimated around the $SL(004)$ reflection index. For an incoming photon in the energy range of (810, 900) eV (around Ni L edges), a corresponding 2θ in the range of (160, 124.5)° is expected with a fixed $q_z \approx 0.8073$ Å^{-1}. Thus an experimental setup that can reach a diffraction angle as high as 160 ° is necessary.

Similarly, for sample (**b**) with a bilayer thickness of approximately 23.35 Å, a corresponding diffraction angle 2θ in the range of (160, 124.5) ° is expected for the soft x-ray $\hbar\omega$ between810 eV and 900 eV with a fixed $q_z \approx 0.8072$Å^{-1} around $SL(003)$ reflection index. Note that a measurement at this high scattering angle is difficult, because it is almost in the backscattering geometry, where the diffraction intensities are rather low and noisy. The Porod's law predicts that the scattering intensity for a smooth surface is related to the transferred wave vector q in a form known as $I \propto q^{-4}$, which also corresponds to a factor of $1/\sin\theta^4$ in the Fresnel equations of reflections. It indicates the small scattering intensities at a high q limit [127], even though we have the reflection intensities from the superlattice. The experiments were performed at the Canadian Light Source (CLS), since there high diffraction angles are available (nominally $2\theta \sim 160°$). Besides a different confinement and probably a different electronic structure between the two samples, a different amount of orthorhombic distortion exists from the crystallographic structure point of view. X-ray reciprocal space maps indicate that both superlattices exhibit an orthorhombic distortion of the DSO substrate. Assuming a $GaFeO_3$ distortion we deduced relatively small distortion angles, i.e. 0.84 ° and a slightly larger tilt angle $\beta = 0.97°$ for sample **a** and sample **b**, respectively.

Again we performed a combined study of the x-ray absorption and the resonant x-ray reflectivity to understand the effect of different cation Dy and La on the orbital occupancy. Fig. 4.14 shows the polarization and energy dependent x-ray reflectivity results of superlattice **a**. The XAS spectra are shown in Fig. 4.1(e), yielding an average orbital polarization $P_{\mathrm{av}} = +(19\pm1)\%$. Fig. 4.14(a) shows the resonant x-ray reflectivity at Ni L_2 and Ni L_3 edges for σ polarized light. The reflected intensities are rather small around the $SL(004)$ peak. Another experimental difficulty arises from the influence of the second-harmonic diffraction peak of the DSO substrate. Nevertheless, two constant q_z values were picked for the energy dependent fixed q_z reflectivity measurements. As demonstrated before, the fixed q_z reflectivity measurements are quite sensitive with a fixed depth resolution [8]. Two q_z values $q_z = 0.781$ Å, 0.788 Å were selected (marked as grey lines in panel (a)). Fig. 4.14(b) and (c) show the reflectivity curves which are normalized to the incoming beam intensity. A different background exists for σ and π polarization for both q_z values. The different linear background were subtracted. Note that at both constant q_z reflectivity measurements, the multiplet structures, i.e. the relative scattering intensities are not identical at the La edges and we do not observe any linear dichroism at the Ni L-edges.

Fig. 4.15 shows the experimental results for sample (**b**): LNO-DSO (2 //4) u.c. on DSO substrate. Panel (a) shows the x-ray absorption results for σ and π polarization. The experimental data are processed in the same way as described before providing an averaged orbital polarization $P_{\mathrm{av}} = (24{\pm}2)\%$. This orbital polarization is slightly enhanced compared to sample (**a**), which we attribute to a stronger confinement effect. Fig. 4.15(b) shows the resonant x-ray reflectivity at the Ni L-edges, where the diffraction intensities at high diffraction angles are extremely low which maybe related to the surface roughness. Fig. 4.15(c) shows the constant q_z reflectivity curves, hardly showing any signal at Ni L-edge energies.

In conclusion, for both superlattices with slightly different orthorhombic distortions, we do not observe a clearly different signal in the constant q_z reflectivity measurements related to different orbital occupancies of the two outer LNO layers. It implies that there is no clear difference in the orbital occupation arising from the different DyO-NiO$_2$-LaO or LaO-NiO$_2$-LaO bonding environ-

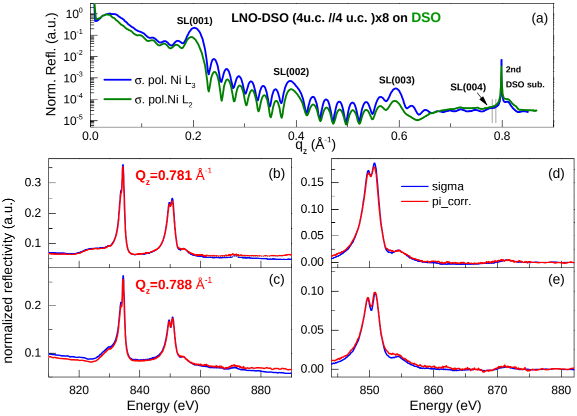

Figure 4.14.: Panel (a): resonant x-ray reflectivity at Ni L_3 and Ni L_2 edges for sample **a**. Panel (b),(c): constant q_z reflectivity spectra (σ and π polarization) around the $SL(004)$ peak for $q_z = 0.781$ Å, 0.788 Å, respectively. Panel (d),(e) show the enlarged constant q_z reflectivity spectra after subtracting a linear background.

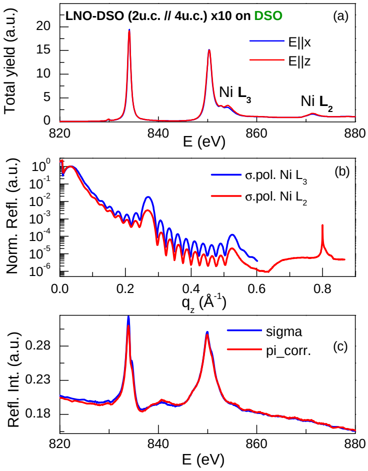

Figure 4.15.: (a): X-ray absorption spectra for LNO-DSO (2 u.c.//4 u.c.) superlattice with different linear polarized light, from which an averaged orbital polarization $P_{\mathrm{av}} = (24 \pm 2)\%$ is obtained; (b): Resonant x-ray reflectivity at Ni L_3 and Ni L_2 edges; (c) Constant q_z reflectivity spectra for different polarized light around the $SL(003)$ peak.

ments. This agrees to some extent with the GGA+U calculation result, i.e. the orthorhombic distortion cancels the difference arising from various cation R bonding environments. This result further suggests that a proper comparison between the theoretical calculation and the experimental results requires taking into account the $GdFeO_3$ distortions. The recent LDA+DMFT calculations also provide reasonably good agreements with the experimental results when including the structural distortions [111]. However, technical difficulties arising from the small scattering intensities with high q limit and the large fluorescence background present challenges for the experiments.

5. Orbital reflectometry on $PrNiO_3$-$PrAlO_3$ superlattices

In this chapter, we present the study of orbital occupations on PNO-PAO superlattices. Since the occupation of the Ni d-orbitals controls the electronic bandwidth, this parameter is of key importance for the phase behavior of nickel oxides. The orbital response to the strain-induced lattice deformation has therefore been intensively studied, both theoretically and experimentally. Conflicting results on the orbital-lattice interaction have been reported. Whereas for ultrathin LNO films [19] as well as LNO-LAO superlattices [36] with single-unit-cell thick LNO layers the response to tensile and compressive strain was reported to be markedly different, a linear, symmetric orbital-lattice coupling was observed in four unit-cell-thick LNO-based superlattices as presented in the previous chapter, in agreement with theoretical predictions [48, 52, 53, 111] and experimental findings for related heterostructures [1, 137].

Special interest in the PNO-based superlattices arose from the observation of tunable charge and spin order by very recent polarized Raman scattering measurements [60]. While a bulk-like insulating phase with charge and spin order is found for samples under tensile strain, a metallic spin-density-wave phase with no (or very weak) charge order is observed for compressive strain [60](as illustrated in Fig. 5.1(a)-(b)). Here, we present a continuation of the study of PNO-based superstructures, focusing on the temperature and strain-dependent spatially-resolved orbital polarizations using the orbital reflectometry technique described before. A series of PNO-PAO superlattices with four consecutive pseudocubic unit cells of PNO and equally thick layer stacks of the band insulators PAO were deposited on different substrates, i.e. LSAO, LAO, LSAT and STO, with $a_{LSAO} < a_{LAO} < a_{\mathrm{PNO\,bulk}} < a_{LSAT} < a_{STO}$, where a is the in-plane lattice constant of the perovskite unit cell.

Hard x-ray diffraction was used to characterize the superlattice quality as well as to study the structural properties. The structural parameters, including the in-plane a_{SL} and out-of-plane lattice constant c_{SL} assuming a tetragonal crystal symmetry are summarized as Fig. 3.12 in Sec. 3.3.5. The resonant x-ray reflectivity and x-ray absorption spectroscopy experimental setup was introduced in Sec. 2.6 (Fig. 2.17).

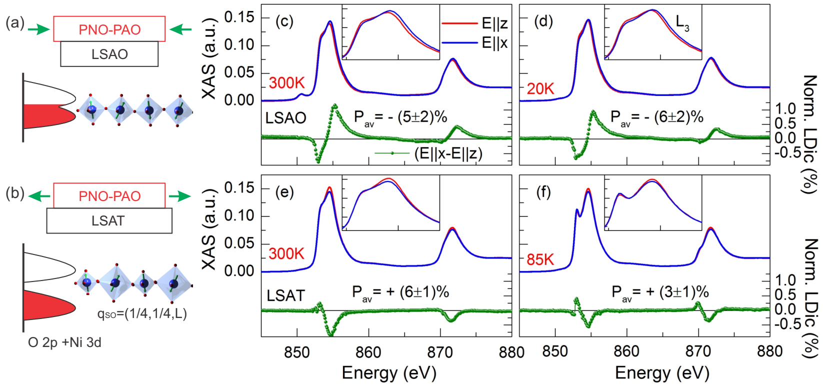

Figure 5.1.: Illustration of the suggested strain-dependent phases below the MIT of PNO-PAO superlattices. Panel (a): a metallic, spin density wave phase under compressive strain (on LSAO) and (b): an insulating state with both spin order ($q_{\text{so}} = (1/4,\ 1/4,\ L)$) and charge order ($q_{\text{co}} = (1/2,\ 1/2,\ L)$) under tensile strain (on LSAT). The corresponding temperature and polarization dependent x-ray absorption spectra for the superlattice under compressive strain are shown in panel (c)-(d) and for tensile strain in panel (e)-(f). The inset of each panel shows the enlarged spectrum near the Ni L_3 edge. In the bottom panels ((c)-(f)) the normalized difference spectra $(I_x(E)\text{-}I_z(E))/(\frac{1}{3}(2I_x + I_z))$ are presented. P_{av} denotes the averaged orbital polarization (Eq. 4.4).

5.1. Temperature dependent x-ray linear dichroism

Polarization dependent x-ray absorption probes the symmetry-dependent projected unoccupied density of states. The hole ratio X_{av} for a Ni^{3+} ion ($3d^7$: $t_{2g}^6 e_g^1$) can be obtained directly from a sum rule analysis as shown in Eq. 4.1, and the orbital polarization is also defined the same as before (Eq. 4.4, Sec. 4.3.2). According to LDA+DMFT calculations [49, 107, 111], the total number of d-orbital occupation n_{e_g} was found to be a crucial parameter for the Fermi surface properties. We like to point out that the experimental results presented here do not depend on n_{e_g}. When calculating P, different values of the d-orbital occupation are only a scaling factor to the total orbital polarization. For consistency with prior work [49, 107, 111],we chose a basis where the total number of electrons in the e_g orbital manifold is $n_{e_g} = 1$. In this basis, P corresponds to the orbital polarization of the integrated projected density of states of the anti-bonding Ni e_g and O p states near the Fermi level.

PNO-PAO superlattices with (4 u.c.//4 u.c.) structure under compressive strain exhibit a metallic phase with a magnetic transition with $T_{\mathrm{Neel}} \approx 100$ K but no (or only very weak) charge order (Fig. 5.1(a)). Fig. 5.1(c),(d) show the corresponding polarization dependent x-ray absorption spectra and the normalized difference spectrum at 300 K and 20 K. For photon polarization perpendicular to the atomic NiO_2 plane ($E \parallel z$), the absorption spectrum is shifted by ~ 0.1 eV to lower energies compared to the spectrum with polarization parallel to the NiO_2 plane ($E \parallel x$). This observation can be explained by the effect of the tetragonal crystal field: due to the compressive strain induced by the LSAO substrate, the Ni-O bond length along the out-of-plane direction is elongated compared to the in-plane bond length, resulting in a lower energy of the $3d_{3z^2-r^2}$ compared to the $3d_{x^2-y^2}$ orbital, thus a preferred out-of-plane orbital occupation. Note that such a shift was also observed for LNO thin films under compressive strain [19]. The low temperature spectra are almost identical to the room temperature measurements, indicating that the magnetic order does not induce any change in the relative orbital occupation.

The situation is different for the PNO-PAO superlattices under tensile strain. The corresponding x-ray linear dichroism data at 300 K and 85 K (above and below the transition temperature, respectively) are shown in Fig. 5.1(e)-(f). Two observations can be stated. First, the low temperature absorption spectra clearly show a double-peak structure at both Ni L_3 and Ni L_2-edges, with an energy splitting of $\sim 1.6\,eV$. This indicates a change of the electronic structure across the MIT to a state with a more localized nature of the final states of the $2p$ - $3d$ transition. The double-peak structure is very similar to those of the smaller rare earth ANO bulk compounds in the insulating phase, indicating a similar local electronic structure [112]. Piamonteze *et. al* reproduced the peak splitting of bulk PNO using an atomic multiplet calculation for D_{4h} symmetry and by varying the crystal field splitting and the spin-orbit coupling [112]. Alternatively the peak splitting can also be related to hybridization with O $2p$ orbitals. ANO compounds are regarded as self-doped Mott insulators, where the negative charge transfer energy implies a crucial role of the O $2p$ states in the band structure as well as the physical properties [71, 100, 101]. The lineshapes in the absorption spectra of PNO-PAO superlattices under tensile strain are almost identical to those of bulk PNO, indicating a common origin, i.e. charge order with two non-equivalent NiO_6 octahedra at low temperatures, in agreement with the robust spin and charge order below T_{MIT} reported in Ref. [60].

A second important observation on the superlattices under tensile strain is that the positions of the $E \parallel x$ and z absorption lines are identical within the experimental error (insets of Fig. 5.1(e),(f)), which implies that the crystal field splitting is too small to be observed. The orbital polarization is thus apparent only in different absorption intensities for $E \parallel x$ and z. A quantitative analysis reveals a reduced orbital polarization below the MIT, i.e. $P_{\mathrm{av}}(85\,\mathrm{K}) = +(3 \pm 1)\,\%$, compared to $P_{\mathrm{av}}(300\,\mathrm{K}) = +(6 \pm 1)\,\%$ (Tab. 5.1). The same measurements were performed at 200, 160 and 120 K (with a temperature error bar of 10 K), from which we obtained averaged orbital polarizations as follows: $P(160\,\mathrm{K}) = P(200\,\mathrm{K}) = P(300\,\mathrm{K}) = +(6 \pm 1)\,\%$, and $P(120\,\mathrm{K}) = P(85\,\mathrm{K}) = +(3 \pm 1)\,\%$. This indicates a rather sharp change across the transition temperature, in good agreement with the temperature dependent changes observed by dc transport and Raman measurements. The observation of $P(T < T_{\mathrm{MIT}}) < P(T > T_{\mathrm{MIT}})$ can be understood in a simplified Ni $3d^{7-\delta}$-$3d^{7+\delta}$ charge order picture, where the admixture of the $3d^8$ configuration (with nominally one electron in each e_g orbital due to Hund's coupling) effectively reduces the orbital polarization below T_{MIT} [93].

A careful reader may notice a weak, polarization-independent peak at ~ 850.5 eV ahead of the Ni L_3 edge in the 300 K spectrum of Fig. 5.1(c), which almost vanishes at 20 K (Fig. 5.1(d)). The peak energy corresponds to the La M_4 white line arising from the LSAO substrate. We relate the temperature dependence of the intensity of this peak to the small change in conductivity and the associated change in the TEY probing depth across the magnetic transition for superlattices on LSAO substrate. For the superlattice on the LSAT substrate, which exhibits a much higher resistivity at room temperature, the peak is not visible due to the lower probing depth.

5.2. Layer resolved orbital profiles

Spatially-resolved orbital polarizations were investigated by the x-ray orbital reflectometry technique (see Sec. 4.2 for details). Fig. 5.2(a)-(d) compares the polarization dependent x-ray absorption spectra for PNO-PAO (4 u.c. // 4 u.c.) superlattices on LSAO, LAO, STO and LSAT substrates. A monotonic increase of the orbital polarization P_{av} as a function of increasing in-plane lattice parameter a_{SL} is observed. The calculated averaged hole ratio X_{av} as well as P_{av} are summarized in Tab. 5.1. Similar to the LNO-based superlattices, a preferred electron occupation of the $d_{3z^2-r^2}$ orbitals ($P_{\mathrm{av}} < 0$) for the superlattice under compressive strain, and a preferred electron occupation of the $d_{x^2-y^2}$ orbitals ($P_{\mathrm{av}} > 0$) for the superlattice under tensile strain is found.

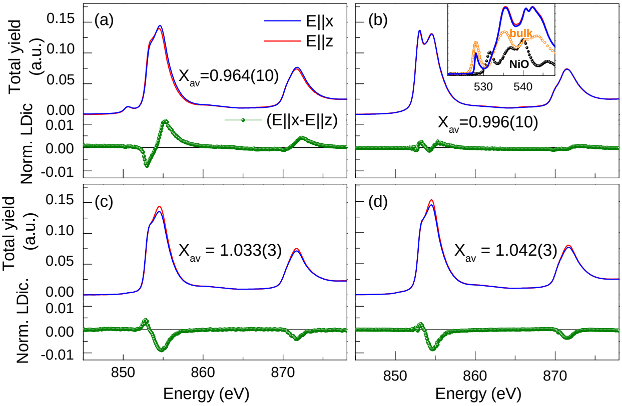

Figure 5.2.: X-ray absorption spectra measured with linearly polarized light for PNO-PAO (4 u.c. // 4 u.c.)×8 superlattice grown on (a) LSAO; (b) LAO; (c) STO and (d) LSAT substrate. Bottom panels are the corresponding normalized difference spectra $(I_x(E)$-$I_z(E))/(\frac{1}{3}(2I_x + I_z))$. Inset of panel (b) shows the polarization dependent absorption spectra at O K edge for PNO-PAO superlattice on LAO substrate (solid lines), as well as the O K edge absorption spectra for bulk PNO (empty circle) and NiO (solid circle) which are digitized from Medarde *et al.* [98].

For the PNO-PAO superlattice on LAO substrate, we observe the absence of average orbital polarization ($P_{\rm av} = (0{\pm}1)$ %). This average zero orbital polarization results from an approximately cubic lattice with $c_{\rm SL} \sim a_{\rm SL} \sim 3.79$ Å. Note that we preformed no resonant x-ray reflectivity measurements for this superlattice.

In particularly, the absorption curves look much different compared to the others which exhibit a much stronger double-peak-structure for PNO-PAO superlattice on LAO substrate. The double-peak-structure could be related to the existence of Ni^{2+} valence states, comparable to the absorption curves of NiO thin films with two distinguished peaks at Ni L-edge [55]. Inset of panel (b) shows the absorption curves around O K energies. The solid lines are the measured XAS spectra for the sample under investigation. The bulk solid circle and the orange empty circle curve correspond to the XAS spectrum for NiO and PNO powder, respectively, which are digitized from Ref. [96, 98] and shifted relatively with the same Pr-O hybridization peak at $\sim 828.1\,eV$.

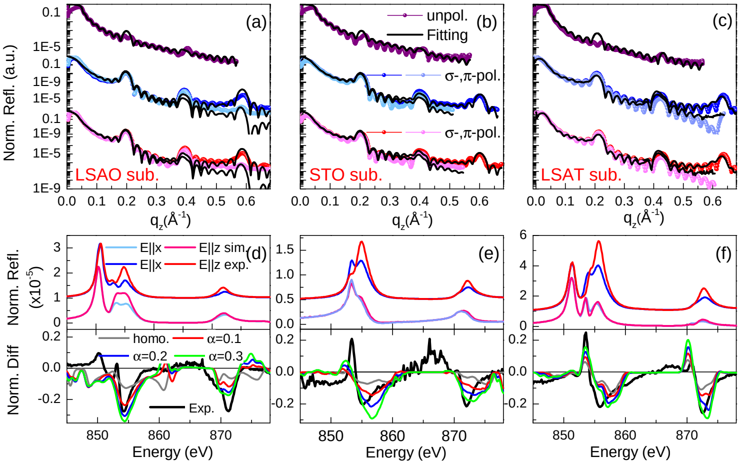

Figure 5.3.: Panel (a)-(c): reflectivity curves as a function of q_z for PNO-PAO superlattices grown on LSAO, STO and LSAT substrate. Top, middle and bottom panels show the reflectivity curves at $E = 8047.7\,eV$ (Cu K_α) and at Ni L_3 and Ni L_2 energies, respectively. All data were normalized to 1 at $q_z = 0$. The solid lines show the fit results based on Parratt's recursive approach. The fitting parameters are summarized in Tab. 5.1. Panel (d)-(f): the corresponding experimental and simulated constant-q_z energy scans at $SL(002)$. The experimental curves are shifted for clarify. The corresponding normalized difference $(I_\sigma(E)$-$I_\pi(E))/(I_\sigma(E)+I_\pi(E))$ are shown directly below together with difference in modulation denoted as α, which is defined as Eq. 4.3.

One can easily notice the existence of the pre-peak structure in the PNO-PAO superlattice (the same as in the bulk PNO), corresponding to $3d^8\underline{L} \rightarrow \underline{c}\ 3d^8$ core-hole excitations, where $\underline{c}$ labels one core hole in O $1s$ state. In comparison with the TEY spectra of bulk NiO, there is a clearly absence of the peak structure related to the presence of the Ni^{2+} valence state, with corresponding $3d^9\underline{L} \rightarrow \underline{c}\ 3d^9$ transitions. Therefore, we conclude that Ni ion in PNO-PAO superlattice on LAO substrate shows predominately Ni^{3+} valence state and the double-peak structure may originate from a more localized states due to the stronger octahedra distortion [13].

Now we turn to the results of the reflectometry measurements. The results of

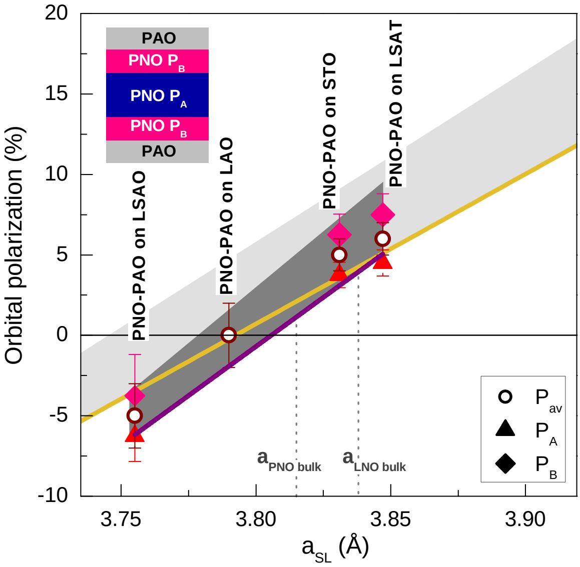

Figure 5.4.: Averaged (P_{av}) and layer-resolved (P_{A}, P_{B}) orbital polarizations as a function of the in-plane lattice constant a_{SL} measured by x-ray diffraction for PNO-PAO superlattices. The orange line represents the linear fitting of the inner layer orbital polarization of LNO-based superlattices, which is reproduced from Fig. 4.11 in Sec. 4.3.3. The light grey area corresponds the additional interfacial effects. The purple line represents a linear fit to the orbital polarization $\mathrm{P_A}$ of the inner layers within the PNO layer stacks. The enhancement of the orbital polarization due to interfacial effects are confined in the dark grey area. The in-plane lattice constant of bulk PNO and LNO are shown as the dashed lines with $a_{\mathrm{PNO\ bulk}} = 3.815$ Å and $a_{\mathrm{LNO\ bulk}} = 3.838$ Å. Note that PNO-PAO superlattice on STO substrate is partially relaxed (The details of the structure characterization for all samples are shown in Fig. 3.12).

the reflectometry measurements are shown in Fig. 5.3(a)-(c) as a function of the the momentum transfer (q_z) along the specular direction. The data processing is described in detail in Sec. 4.1. To obtain a proper structural model, we used Parratt's recursive approach implemented in our advanced reflectometry fitting program REMAGX [90]. The resulting structural parameters (which are summarized in Tab. 5.1) were kept fixed for the simulation of the dichroic reflectivity.

To probe the difference between the inner and outer layers (denoted as A and B, respectively) within a 4 u.c. thick PNO layer stack, the energy- and polarization dependent reflectivity spectra were measured at a fixed momentum transfer q_z close to the $SL(002)$ reflection(Fig. 5.3(d)-(f)). Following arguments provided before, the scattering factor of the $SL(002)$ reflection is particularly sensitive to the difference of the scattering factors of the outer and inner layers. Note that in TEY mode the contribution of the La M-edge from the LSAO and LSAT substrate is negligible (Fig. 5.2 (a)-(d)). To determine the contribution of the LASO and LSAT substrates to the reflectivity, we extracted the La M-edge optical constants from $LaCoO_3$ XAS spectra by fitting them to the theoretical values from the Chantler table. The simulated reflectivity curves are shown in the upper panels of Fig. 5.3(d) and (f). Since there is no dichroism at the La M_4 edge, the normalized difference spectra (lower parts of Fig. 5.3(d)-(f)) are not affected by this contribution.

Figure 5.4 summarizes the averaged orbital polarizations P_{av}, the inner layer orbital polarization P_{A}, and the outer layer orbital polarization P_{B} as a function of a_{SL} for superlattices based on PNO (this work; see also Tab. 5.1) and LNO (Sec. 4.3.3). For all superlattices we observe $P_{\mathrm{B}} > P_{\mathrm{A}}$, i.e. an enhanced occupation of the $d_{x^2-y^2}$ orbital in the interface layers adjacent to PAO. The results for P_{A} of the PNO-based superlattices fit reasonably well to the linear

Substrate	structure (u.c.)	α	$\mathbf{P}_{\mathrm{av}}$ (%)	$\mathbf{P}_{\mathbf{B}}$ (%)	$\mathbf{P}_{\mathbf{A}}$ (%)
$LSAO_{0.4}$	$3.9_{0.6}[(4.0_{0.7}/4.4_{0.3})x7]5.1_{0.7}$	0.25(10)	$\mathbf{-5 \pm 2}$	**-4**	**-6**
$STO_{0.6}$	$4.2_{0.9}[(4.2_{0.9}/4.1_{0.4})x7]4.5_{0.6}$	0.25(5)	$\mathbf{5 \pm 1}$	**6**	**4**
$LSAT_{0.5}$	$4.2_{0.4}[(3.8_{0.5}/4.0_{0.9})x7]4.0_{2.1}$	0.25(5)	$\mathbf{6 \pm 1}$	**8**	**5**

Table 5.1.: Structure parameters for PNO-PAO superlattices: substrate material, superlattice structure, the modulation α from the dichroic reflectivity modeling and the orbital polarizations of PNO-PAO heterostructures. The superlattice structure obtained from the fitting of the reflectivity (see text) is given in the following nomenclature: $d_\sigma^{PNObottom}[(d_\sigma^{PNO}/d_\sigma^{PAO})\mathrm{xM}]d_\sigma^{PAOtop}$ with thickness d and roughness σ in u.c. calculated by dividing c_{SL}.

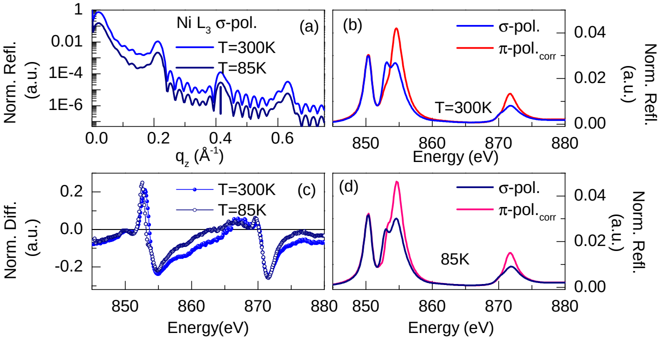

Figure 5.5.: Temperature dependent resonant x-ray reflectivity of the PNO-PAO superlattices on LSAT substrate. (a) Resonant x-ray reflectivity curves measured with σ polarized light. Panel (b) and (d) show the energy and polarization dependent normalized reflectivity spectra with fixed $q_z = 0.4148$ Å measured at T = 300 K and T = 85 K, respectively. Panel (c) compares the normalized different spectra $(I_\sigma(E)\text{-}I_\pi(\mathrm{E}))/(\mathrm{I}_\sigma(E)+I_\pi(E))$ of both phases.

P_A-a_SL dependence in LNO-based superlattices. For comparison, we also fitted P_A for the PNO-based superlattices alone (purple line in Fig. 5.4). The slope of the P_A-versus-a_SL line is slightly higher, which might be related to the increase of octahedral distortions in PNO-based superlattices, compared to those based on LNO, the latter exhibiting a tolerance factor closer to one. Such a tendency towards higher orbital polarizability for distorted structures with tilts and rotations of the $\mathrm{NiO_6}$ octahedra was also observed in recent calculations based on the GGA, and was attributed to the difference in hybridization between Ni d- and O p-orbitals [111].

For the PNO-PAO superlattice on the LSAT substrate, which shows a temperature dependent change in orbital occupancy across the MIT as discussed above, we obtained the spatially-resolved orbital polarizations of both metallic and insulating phases. Fig. 5.5(a) presents the momentum dependent resonant x-ray reflectivity curves measured with σ-polarized light at T = 300 K and T = 85 K. While temperature dependent changes in the q-dependent reflectivity are hardly visible, they become obvious in the energy-dependent data at fixed nocumentum close to the $SL(002)$ reflection (Fig. 5.5(b) and (d)). Note that these temperature dependent changes in scattering only occur at Ni L-edge energies; no corresponding change are observed at other energies including the La M_4-edge. Apart from these differences in line shape, which are related to the changes in XAS discussed above, the normalized difference of the constant-q_z spectra are identical in both phases (Fig. 5.5(c)). This implies that the difference in orbital occupation of the outer and the inner layers inside the 4 u.c. PNO stack is unaffected by the MIT, presumably because the charge disproportionation below T_{MIT} encompasses the entire PNO layer stacks.

In conclusion, the low-temperature charge- and spin-ordered phase in PNO-PAO superlattices under tensile strain exhibits a reduced orbital polarization, which can be qualitatively explained as a consequence of the Hund's coupling in the charge-disproportionated state. In contrast, we found no change in orbital polarization at the magnetic transition of superlattices under compressive strain. An approximately linear dependence of the orbital occupation on strain is observed both for PNO-PAO superlattices and for LNO-LAO superlattices grown on different substrates.

6. X-ray reflectometry as a probe of octahedral distortions

Strain engineering of octahedral rotations has been proposed as a means to tailor the electronic properties in perovskite thin films and superlattices [115]. The main mechanism is related to the modification of the bond lengths via octahedral distortions (e.g. the strain-induced enhancement of ferroelectric transition temperature in Ref. [23, 47]), or/and the modification of the octahedral rotation patterns and amplitudes which is linked to the electric and magnetic behaviors in the system (e.g. the stability of Ru magnetic moment in $SrRuO_3$-based thin films [152], the spin-state transition in epitaxial strained $LaCoO_3$ films [116], etc). The strain-induced octahedral distortion, in particular, the strain bond-angle coupling mechanism has been reported to provide the physical basis for the diversity of electronic propertied by first-principle calculations [103, 117]. Nickelates have served as an important model system for the exploration of these strategies. Bulk nickelates are sensitive to the magnitudes of the octahedral distortions. It has been shown that the Ni-O-Ni bond angles control the electronic bandwidth, thus the MIT temperature and the Neel temperature in the system [16]. In LNO thin films and LNO-based superlattices, different physical properties such as charge disproportionation, lattice-orbital coupling as well as magnetism have been reported in response to external tensile or compressive strain, which induce different octahedral distortion patterns to the layers [11, 19, 36, 71, 92]. In PNO and NNO thin films, strain has turned out to be an effective parameters in controlling the MIT but the underlying mechanism is still under debate [79, 85, 86]. The understanding of the strain-bond angle interaction is limited experimentally. A direct mapping of the atomic positions by transmission electron microscopy is still a challenge for light atoms such as oxygen [69, 142]. On the other hand, the measurement of half-order Bragg peaks using x-ray diffraction can provide information on the crystallographic space group as well as the oxygen positions quantitatively via structural refinements [34, 92], however, in an averaged manner, i.e. not resolved for the individual layer of a heterostructure. Here, we propose to apply the x-ray reflectometry technique to probe the octahedral distortions.

Before we present the experimental details, let us have a short review of the octahedral rotations for LNO-based thin films and superlattices. Bulk LNO shows an $a^-a^-a^-$ rotation pattern in Glazer's notation with rotation angles $\alpha = \beta = \gamma = 5.2\ ^\circ$, i.e. the neighboring octahedra are antiphase tilted along the crystal x-, y-, z-axes [40]. May *et al.* reported structural refinements for LNO thin films under tensile (on STO substrate, with lattice mismatch +1.7%) and compressive strain (on LAO substrate, with lattice mismatch -1.1%), where they presented the corresponding octahedral rotation angles $\alpha = \beta = 7.2 \pm 0.2\ ^\circ$, $\gamma = 0.3 \pm 0.7\ ^\circ$ and $\alpha = \beta = 1.2 \pm 0.2\ ^\circ$, $\gamma = 7.9 \pm 0.7\ ^\circ$, respectively [92]. Some parameters including the in-plane Ni-O bond lengths as well as the out-of-plane tilt angles are highly sensitive to strain effects. Researchers have also performed some structural refinements for LNO-LAO superlattices by the same measurement method [76, 88]. In partic-

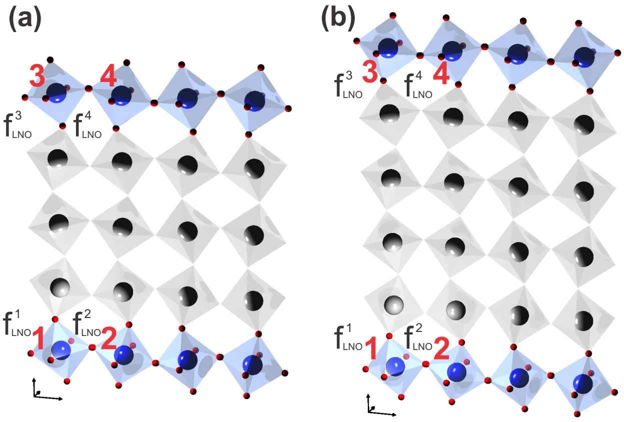

Figure 6.1.: Illustration of the octahedral rotation in nickel oxide heterostructures with an a^- rotation pattern along the crystal z-direction. Panel (a): LNO-LGO (1 u.c.//3 u.c.) superlattice (sample **A**) with the same octahedral rotation of the neighboring LNO layers along the specular direction (site 1 and 3, site 2 and 4); (b): LNO-LGO (1 u.c.//4 u.c.) superlattice (sample **B**) with the opposite octahedral rotation of the neighboring LNO layers along the specular direction. f^i_{LNO} denotes the corresponding scattering factor for site $i = 1, 2, 3, 4$.

ular, for LNO-LAO superlattices under compressive strain (LSAO substrate, with lattice mismatch -2.4%), the Ni-O bond distance is elongated along the out-of-plane direction, while the tilt angle γ is increased to accommodate the compressive strain. The corresponding tilt angles are: $\alpha = \beta = 1.9 \pm 0.2$ ° and $\gamma = 11.6 \pm 1.2$ °. For LNO-LAO superlattices on LSAT substrates (tensile, with lattice mismatch +1.0%), the in-plane Ni-O bonds are straightened, resulting in the following rotation angles: $\alpha = \beta = 0.0 \pm 0.2$ ° and $\gamma = 5.2 \pm 1.9$ °. Therefore, one can expect a monoclinic distortion with an $a^-a^-c^-$ rotation pattern as the starting point for the investigation of octahedral tilts in LNO-LXO superlattices (X = Al, Ga).

The experiment described here is an extension of the layer-resolved orbital profile and its sensitivity to different bonding environments, i.e. different ways of octahedral rotation in LNO layers. Two samples are under investigation:

Sample **A**: LNO-LGO (1 u.c.//3 u.c.) × 16 on STO substrate.

Sample **B**: LNO-LGO (1 u.c.//4 u.c.) × 13 on STO substrate.

Fig. 6.1 illustrates the octahedral rotation for LNO-LGO superlattices with a structural configuration of **A**: (1 u.c.//3 u.c.) and **B**: (1 u.c.//4 u.c.) considering an $a^-a^-c^-$ distortion pattern with monoclinic symmetry for the crystal. One can easily notice that the octahedra of the neighboring LNO layers along the z-direction are rotated in phase for sample **A** (Fig. 6.1(a)), whereas the neighboring LNO octahedra rotate antiphase for sample **B**. The artificially designed superlattice configuration in a sense changes the bonding environment of the neighboring LNO layers.

The scattering intensity for sample **A/B** $I_{001}^{A/B}$ can be written as follows:

$$\begin{aligned} I_{001}^{A/B} &\propto \sum_i f_i \, \exp(iq_z \, z) \\ &\propto (f_{LNO}^1 + f_{LNO}^3 - 2f_{LGO})^2 + (f_{LNO}^2 + f_{LNO}^4 - 2f_{LGO})^2. \end{aligned}$$

Here the superscripts $1, 2, 3, 4$ denote different $\mathrm{NiO_6}$ sites as shown in Fig. 6.1. Moreover, we can make the assumption that the octahedral distortions of the LGO layers are not so important when tuning the incident photon energies to Ni resonant edges where the scattering cross section from Ni is dramatically enhanced at resonant edges.

The conductivity tensor with a monoclinic symmetry can be written as:

$$\sigma^{mono} = \begin{pmatrix} \sigma_{xx} & \sigma_{xy} & 0 \\ \sigma_{yx} & \sigma_{yy} & 0 \\ 0 & 0 & \sigma_{zz} \end{pmatrix},$$

with $\sigma_{xy} = \sigma_{yx}$.

Moreover, for a crystal with an opposite rotation pattern, the conductivity can be written in a similar way, but with different signs in the off-diagonal terms, i.e. -σ_{xy} and -σ_{yx}. Therefore, we can specify the scattering intensity for sample **A** and sample **B** with corresponding structural configurations as shown in Fig. 6.1.

$$\begin{aligned}
I_{001}^{A} &\propto (\sigma_{LNO}^{1} + \sigma_{LNO}^{3})^2 + (\sigma_{LNO}^{2} + \sigma_{LNO}^{4})^2 \\
&= (\begin{pmatrix} \sigma_{xx} & \sigma_{xy} & 0 \\ \sigma_{yx} & \sigma_{yy} & 0 \\ 0 & 0 & \sigma_{zz} \end{pmatrix} + \begin{pmatrix} \sigma_{xx} & \sigma_{xy} & 0 \\ \sigma_{yx} & \sigma_{yy} & 0 \\ 0 & 0 & \sigma_{zz} \end{pmatrix})^2 \\
&\quad + (\begin{pmatrix} \sigma_{xx} & -\sigma_{xy} & 0 \\ -\sigma_{yx} & \sigma_{yy} & 0 \\ 0 & 0 & \sigma_{zz} \end{pmatrix} + \begin{pmatrix} \sigma_{xx} & -\sigma_{xy} & 0 \\ -\sigma_{yx} & \sigma_{yy} & 0 \\ 0 & 0 & \sigma_{zz} \end{pmatrix})^2 \\
&= 4 \times (\begin{pmatrix} \sigma_{xx} & \sigma_{xy} & 0 \\ \sigma_{yx} & \sigma_{yy} & 0 \\ 0 & 0 & \sigma_{zz} \end{pmatrix}^2 + \begin{pmatrix} \sigma_{xx} & -\sigma_{xy} & 0 \\ -\sigma_{yx} & \sigma_{yy} & 0 \\ 0 & 0 & \sigma_{zz} \end{pmatrix}^2); \qquad (6.1)
\end{aligned}$$

whereas the scattering intensity for sample **B** I_{001}^{B} can be expressed as:

$$\begin{aligned}
I_{001}^{B} &\propto (\sigma_{LNO}^{1} + \sigma_{LNO}^{3})^2 + (\sigma_{LNO}^{2} + \sigma_{LNO}^{4})^2 \\
&= (\begin{pmatrix} \sigma_{xx} & \sigma_{xy} & 0 \\ \sigma_{yx} & \sigma_{yy} & 0 \\ 0 & 0 & \sigma_{zz} \end{pmatrix} + \begin{pmatrix} \sigma_{xx} & -\sigma_{xy} & 0 \\ -\sigma_{yx} & \sigma_{yy} & 0 \\ 0 & 0 & \sigma_{zz} \end{pmatrix})^2 \\
&\quad + (\begin{pmatrix} \sigma_{xx} & -\sigma_{xy} & 0 \\ -\sigma_{yx} & \sigma_{yy} & 0 \\ 0 & 0 & \sigma_{zz} \end{pmatrix} + \begin{pmatrix} \sigma_{xx} & \sigma_{xy} & 0 \\ \sigma_{yx} & \sigma_{yy} & 0 \\ 0 & 0 & \sigma_{zz} \end{pmatrix})^2 \\
&= 8 \times \begin{pmatrix} \sigma_{xx} & 0 & 0 \\ 0 & \sigma_{yy} & 0 \\ 0 & 0 & \sigma_{zz} \end{pmatrix}^2 . \qquad (6.2)
\end{aligned}$$

The scattering factor of the $SL(001)$ peak is hence only sensitive to the different bonding environments of the neighboring LNO layers along the specular direction. The difference between sample **A** and **B** is obvious, i.e. the scattering intensity of sample **B** is not sensitive to the octahedral distortions, as indicated by the canceling of the off-diagonal terms in evaluating the sum

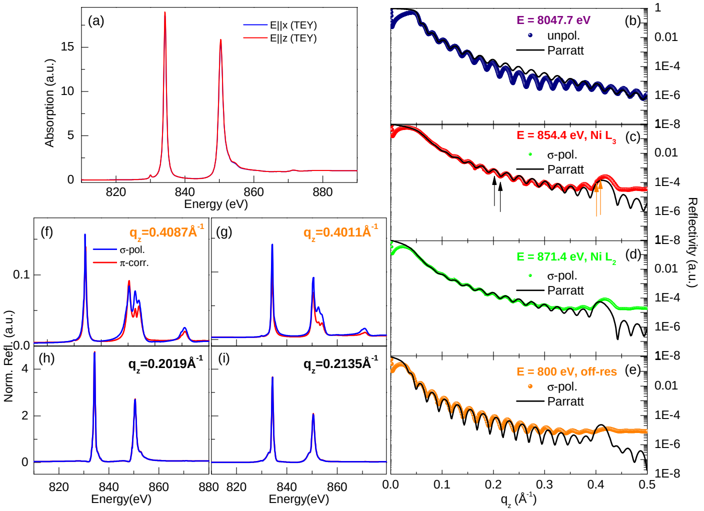

Figure 6.2.: Experimental results of sample **A**. Panel (a): X-ray absorption spectra for linear polarized lights. Panel (b)-(e) show the q_z dependent x-ray reflectivity curves at different resonant and off-resonant energies. The black curves are the fitting results using the Parratt's recursive method. The fitting structural parameters are listed as Tab 6.1. Panel (f)-(i) show the experimental measured reflectivity curves at a constant q_z with σ and π polarizations. Panel (f),(g) show the reflectivity curves around the $SL(001)$ peak with $q_z = 0.4087, 0.4011$ Å, respectively (marked as orange short lines in panel (c)). Panel (h)-(i) show the reflectivity spectra at $q_z = 0.1709$ Å and $q_z = 0.1809$ Å (black short lines in panel (c)).

of the conductivity tensors.

The method of orbital reflectometry introduced in previous chapters is extremely sensitive to subtle charge profiles between interface and inner layers. Here we study the constant q_z resonant reflectivity at $SL(001)$ to verify the in-phase/antiphase bonding environment. A further simulation of the fixed q_z reflectivity intensities allows us obtain quantitative information on the rotation angles. The samples are prepared with the same total thickness as shown in Fig. 3.11 (Sec. 3.3.4). Good sample qualities are verified by hard x-ray diffraction measurements.

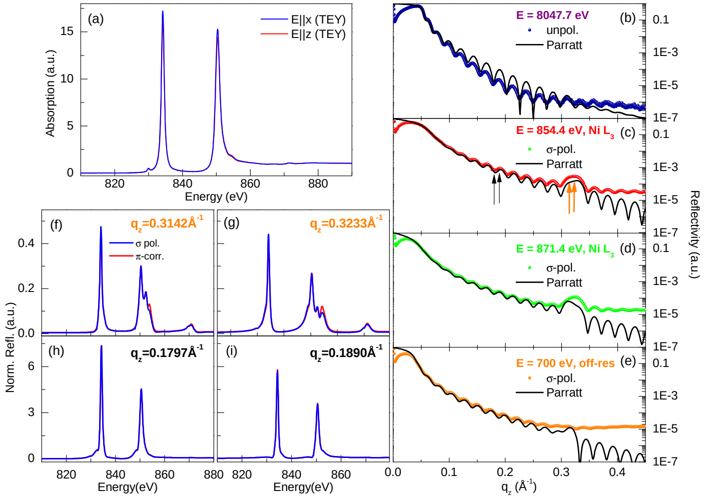

Figure 6.3.: Experimental results of sample **B**. (a): X-ray absorption spectra for linear polarized lights. (b)-(e) shows the q_z dependent x-ray reflectivity curves at different energies labeled at each panel. The black curves are the fitting result using the Parratt's recursive method. The fitting structural parameters are listed as Tab. 6.1. (f)-(i) show the experimental measured reflectivity curves at a constant q_z with σ and π polarizations. Panel (f)-(g) show the reflectivity results around the $SL(001)$ peak with $q_z = 0.3142$ Å and $q_z = 0.3233$ Å, respectively (marked as orange arrow in panel (c)). Panel (h)-(i) represent the reflectivity spectra at $q_z = 0.2019$ Å and $q_z = 0.2135$ Å (black arrows in panel (c)).

Fig. 6.2 and Fig. 6.3 show the result of the x-ray absorption and reflectivity measurements for sample **A** and sample **B**, respectively. The absorption spectra measured with linearly polarized light were collected in the TEY mode. For both samples, we observed the absence of linear dichroism at Ni resonant edges, which indicates that there is no clearly preferred orbital occupation. Note that the absorption spectrum only probes a thin LNO layer in this surface-sensitive TEY mode and the La M-edge is dominant. Unfortunately, we had some troubles with fluorescence diodes during this beamtime, otherwise it might have provided more conclusive results. Panel (b)-(e) show the q_z dependent reflectivity curves both on and off resonances, i.e. at Cu K_α

composition	subs. $t(\sigma)$ Å(Å)	LNO $t(\sigma)$ Å(Å)	LGO $t(\sigma)$ Å(Å)
LNO-LGO (1//3)	∞(3.1)	3.83(2.0)	11.5(3.0)
LNO-LGO (1//4)	∞(2.9)	3.2(2.1)	16.6(2.7)

Table 6.1.: The fitting parameters, i.e. the roughness of the substrate σ, the thickness t and the roughness σ of LNO and LGO layers for sample **A** and sample **B** based on Parratt's recursive method.

edge with $E = 8047.7\ eV$, at the Ni L_3-edge with $E = 854.4\ eV$, at the Ni L_2 resonant edge with $E = 871.4\ eV$ and at the soft x-ray off-resonant edge $E = 700\ eV$, respectively. The structural model is obtained by fitting the hard x-ray reflectivity data using Parratt's recursive method, which also gives a nice description of the full set of data measured for different energies (the black curves). The fitting parameters in terms of the thickness t and the roughness σ are summarized in the Tab. 6.1. Panel (f)-(i) of Figs. 6.2 and Figs. 6.3 show the corresponding constant-q_z curves, where polarization-dependent differences between scans with σ and π- polarized light become more obvious. In principle the differences should also exist in the polarization-dependent reflectivity measurement at fixed energies, but in a less distinct manner due to the lack of depth resolution. For sample **A**, the fixed-q_z curves show a strong polarization dependence around the $SL(001)$ reflex with $q_z = 0.4087$, 0.4011 Å. The pronounced difference appears not only in different intensities but also in different line-shapes. Moreover, there is almost no polarization dependence at other scattering momentum values. Fig. 6.2 (h) and (i) represent the polarization dependent reflectivity curves with $q_z = 0.1709$ Å and $q_z = 0.1809$ Å , which correspond to the valley with destructive interference and the peak position with constructive interference, respectively (as marked in Fig. 6.2(c)). According to the estimation of the $SL(001)$ scattering factor in Eq. 6.1, these differences arise from the difference of the top and the bottom LNO layers.

For sample **B** with a structure configuration of LNO-LGO (1 u.c.//4 u.c.), we do not observe a similar behavior. Fig. 6.3 (f) and (g) show the reflectivity curves with $q_z = 0.3142$ Å and $q_z = 0.3233$ Å around the $SL(001)$ reflection index, the change due to different polarized incident light is considerably smaller. The scattering spectra have similar line-shapes and almost indentical intensities. At the scattering momenta of $q_z = 0.2019$ Å and $q_z = 0.2135$ Å , there is no dichroic difference, as previously found in sample **A**.

We noted that the observed phenomena are not related to the lack of accuracies in the fitting results based on Parratt's recursive method at high q_z

limits, since similar fitting inaccuracies which might be related to the surface roughness appear in both sample **A** and sample **B**, whereas we only observed substantial polarization dependent reflectivity curves around $SL(001)$ for sample **A**. The experimentally observed strong polarization dependent reflectivity curves are qualitatively in agreement with the scattering intensity I^{A}_{001} calculated by taking into account the octahedral tilts and rotations. Therefore, we will focus on the quantitative description of the effect observed in sample **A** below.

In order to understand the experimental results, we modeled the reflectivity intensities with REMAGX. The effect of the octahedral rotation gives rise to a low crystal symmetry. A good starting point is the assumption of a monoclinic symmetry, as mentioned before. The conductivity tensor σ^{mono} then can be obtained by multiplying the tetragonal tensor σ^{tetra} with the rotation matrix R through:

$$\sigma^{mono} = R^T \cdot \sigma^{tetra} \cdot R, \tag{6.3}$$

with R^T being the transposed matrix of R.

Taking the example of a rotation along the x-axis with angle α, along the y-axis with angle α (no in-plane anisotropy), and along z-axis with angle θ (these rotation angles are specified in Fig. 3.1), the rotation matrix is given by:

$$R_1 \cdot R_2 \cdot R_3 =$$

$$\begin{pmatrix} 1 & 0 & 0 \\ 0 & \cos\alpha & \sin\alpha \\ 0 & -\sin\alpha & \cos\alpha \end{pmatrix} \cdot \begin{pmatrix} \cos\alpha & 0 & -\sin\alpha \\ 0 & 1 & 0 \\ \sin\alpha & 0 & \cos\alpha \end{pmatrix} \cdot \begin{pmatrix} \cos\theta & \sin\theta & 0 \\ -\sin\theta & \cos\theta & 0 \\ 0 & 0 & 1 \end{pmatrix}, \tag{6.4}$$

therefore, the corresponding monoclinic matrix σ_1^{mono} is:

$$\sigma_1^{mono} = R_1^T \cdot R_2^T \cdot R_3^T \cdot \sigma^{tetra} \cdot R_3 \cdot R_2 \cdot R_1. \tag{6.5}$$

For the adjacent layer with an opposite rotation, i.e. a rotation of -α, -α and

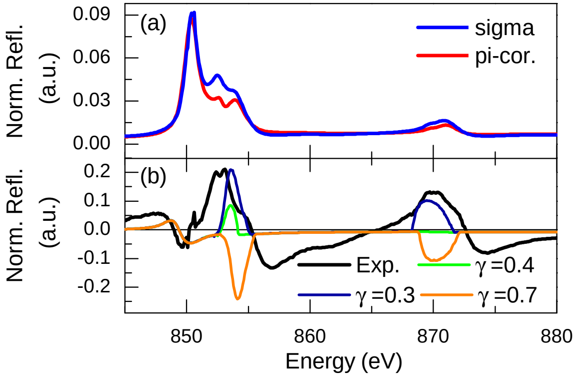

Figure 6.4.: Panel (a): experimental constant q_z reflectivity curves with fixed $q_z = 0.4011$ Å. (b): normalized different curves with different γ in cluster calculations with a fixed crystal field splitting $\Delta = 100\ meV$. $\gamma = 0.4$, 0.3 and 0.7 correspond to an average orbital polarization of $P_{\mathrm{av}} =$ -15%, -30% and +30%, respectively.

-θ along the x, y and z-axis, respectively, the rotation matrix is:

$$R'_1 \cdot R'_2 \cdot R'_3 =$$
$$\begin{pmatrix} 1 & 0 & 0 \\ 0 & \cos\alpha & -\sin\alpha \\ 0 & \sin\alpha & \cos\alpha \end{pmatrix} \cdot \begin{pmatrix} \cos\alpha & 0 & \sin\alpha \\ 0 & 1 & 0 \\ -\sin\alpha & 0 & \cos\alpha \end{pmatrix} \cdot \begin{pmatrix} \cos\theta & -\sin\theta & 0 \\ \sin\theta & \cos\theta & 0 \\ 0 & 0 & 1 \end{pmatrix}, \tag{6.6}$$

which gives rise to a different monoclinic conductivity tensor σ_2^{mono} as:

$$\sigma_2^{mono} = R_1'^T \cdot R_2'^T \cdot R_3'^T \cdot \sigma^{tetra} \cdot R'_3 \cdot R'_2 \cdot R'_1. \tag{6.7}$$

In particular, for sample **A**, the optical constants for site 1 and site 3 are given by σ_1^{mono}, while σ_2^{mono} is relevant for site 2 and site 4.

The script used in the REMAGX simulation can be found in Appendix A.3.

Based on Eq. 6.3 - Eq. 6.5, we notice that the off-diagonal terms in the monoclinic conductivity tensor are proportional to the difference of the diagonal terms, i.e. $\sigma_{xy} \propto (\sigma_{zz} - \sigma_{xx})$, and its influence is extremely small compared to the diagonal terms. The off-diagonal terms can only be obtained if there exist

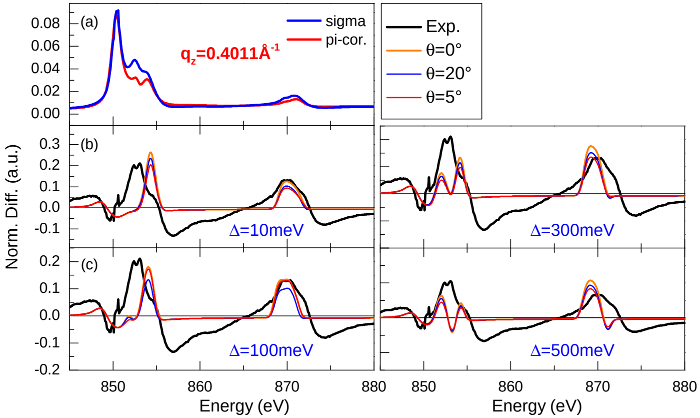

Figure 6.5.: Panel (a): constant q_z reflectivity curves for σ and π polarizations at $q_z = 0.4011$ Å. (b)-(e) Normalized different curves obtained by $(I_\sigma - I_{\pi_{cor.}})/(I_\sigma + I_{\pi_{cor.}})$ for different crystal field splitting energies $\Delta = 10\ meV$, $100\ meV$, $300\ meV$ as well as $500\ meV$, respectively. The dark black line shows the experimental normalized different curve. The others are the simulation curves with different octahedral rotation angles: $\theta = 0°, 5°, 20°$. The input optical constants are obtained by merging the absorption curves from cluster calculation to the Chantler table with $\gamma = 0.3$.

differences in the diagonal terms via matrix rotation approach. Thus we have to make a quantitative modeling taking into account the natural dichroism, which is not in agreement with the current absorption data (Fig. 6.2(a)) and will be addressed hereafter.

We hence first reduce the problem to a tetragonal tensor with relative big difference between the diagonal terms. We calculate the difference $(\sigma_{zz} - \sigma_{xx})$ following the principles presented in Chapter 2. Fig. 6.4(b) shows the simulated normalized difference curves together with the result of model calculations. In detail, the optical constant is obtained by merging the spectra from the cluster calculations to the Chantler table. The spectra with different magnitudes of orbital occupation are varied by changing the admixture coefficient γ. As discussed in Sec. 4.3.1, the measured spectra for the x-ray absorption measurements can be described as linear superposition of spectra, $I_{x,z}^{x^2-y^2}(E)$, $I_{x,z}^{3z^2-r^2}(E)$, which are calculated for 100% occupation of either the $x^2 - y^2$ or the $3z^2 - r^2$ orbital and for the polarization of the incoming light parallel to the x and z direction, respectively. For instance, the absorption spectra for the z-polarized light is obtained by $I_z(E) = \gamma I_z^{x^2-y^2}(E) + (1-\gamma) I_z^{3z^2-r^2}(E)$. $\gamma = 0.5$ indicates the same spectral weight of the linear x-polarized and z-polarized light, i.e. the same electron occupation between $d_{x^2-y^2}$ and $d_{3z^2-r^2}$ orbitals. Fig. 6.4(b) shows the effect of changing γ in the normalized different curves. $\gamma = 0.4$ corresponds to an orbital polarization $P_{\mathrm{av}} = +15\%$ (taking $\mathrm{n}_{eg} = 1$, see discussion in Sec. 4.3.2). A better agreement with the experimental result is obtained with $\gamma = 0.3$ (i.e. $P_{\mathrm{av}} = 30\%$), whereas $\gamma = 0.7$ (P_{av} = -30%) with a preferred orbital occupancy of $d_{3z^2-r^2}$ orbital is worse.

We fixed $\gamma = 0.3$ in the following discussions. Fig. 6.5 shows the REMAGX simulated reflectivity results with fixed $q_z = 0.4011$ Å. Fig. 6.5(b)-(d) show the normalized different curves with different crystal field splitting energies, i.e. $\Delta = 10\ meV$, $100\ meV$, $300\ meV$ and $500\ meV$, respectively. The simulations were performed with different rotation angles, i.e. $\alpha = \theta = 0^\circ$, 5° and 20°. The normalized different curves are shown in the corresponding panel. Note that the effect of the crystal field splitting produces a shift of the spectra with different polarizations. In particular, Δ corresponds to a bigger energy splitting between $d_{x^2-y^2}$ and $d_{3z^2-r^2}$ orbitals, and a lower energy of $d_{x^2-y^2}$ orbital is expected due to the preferred orbital occupations. Thus, for photons with polarization parallel to the $\mathrm{NiO_2}$ plane ($E \parallel x$), the absorption energy is lower than that for photons with polarization perpendicular to the $\mathrm{NiO_2}$ plane ($E \parallel z$). With increasing crystal field splitting energy Δ, the agreement at Ni L_3 edge becomes better. However, it is hard to judge which Δ provides a better description of the experimental results.

As mentioned above, a natural linear dichroism is needed for a better explanation of the measured spectra based on this approach. However, our experimental result (Fig. 6.2 (a)) does not indicate any preferred orbital occupation in the polarization dependent x-ray absorption measurements. One possible reason is that it is related to the presence of inhomogeneities inside the superlattice. XAS is a local approach that collects the intensities on average, but the x-ray reflectivity with a fixed penetration depth can provide spatially resolved information along the superlattice normal direction. However, this is not in agreement with sample **B**, which should have a comparable orbital polarization. In principle, for both samples with 1 u.c. thick LNO layers sandwiched with several layers of insulators $\mathrm{LaGaO_3}$, a strong confinement and thus a big orbital polarization is expected from theoretical calculations. Therefore, we can exclude the inhomogeneities as a possible origin. Another technical reason is that we only probe a few top LNO layers, which contribute tiny TEY signals at Ni edges compared to neighboring La edges with huge absorption intensities. The experimental result can be confirmed or rechecked in the future by collecting the bulk-sensitive fluorescence signal. Finally, the roughness of a single LNO layer is about half unit cell (~ 2 Å) from structural fitting, which suggests that the sample quality should be improved for further investigations.

In conclusion, the orbital reflectometry method is very sensitive to the octahedral tilt patterns. We provide the first step towards a quantitative understanding of the observed strong polarization dependent reflectivity results. This ansatz where the monoclinic conductivity tensor is obtained by rotating the tetragonal conductivity tensor obviously does not yet explain our experimental result quantitatively. Further efforts are required to obtain a fully understanding of the reflectivity behavior. For instance, an understanding of the current experimental results might be improved if one could get a proper optical constant from experiments (such as measuring the fluorescence yield spectra) or from theoretical calculations (such as the local-density-approximation calculations).

A. Appendices

A.1. Values of 3J symbols

The matrix element of spherical tensors are evaluated by Wigner-Eckart theorem in terms of $3J$ symbols, i.e.

$$\langle l_m|C_q^{(k)}|c_{m'}\rangle = (-1)^m\sqrt{(2l+1)(2c+1)}\begin{pmatrix} l & k & c \\ 0 & 0 & 0 \end{pmatrix}\begin{pmatrix} l & k & c \\ -m & q & m' \end{pmatrix}.$$

For a $2p \rightarrow 3d$ transition, $l=2$, $c=1$, and $k=1$ for the incident beam. Here we list the values of $3J$ symbols for calculating the transition probability (neglecting the prefactors). With linear z-polarized light, i.e. $q=0$, the non-vanishing $3J$ symbols are:

$$\begin{pmatrix} 2 & 1 & 1 \\ -1 & 0 & 1 \end{pmatrix} = -\sqrt{\frac{1}{10}}\,;$$

$$\begin{pmatrix} 2 & 1 & 1 \\ 0 & 0 & 0 \end{pmatrix} = \sqrt{\frac{2}{15}}\,;$$

$$\begin{pmatrix} 2 & 1 & 1 \\ 1 & 0 & -1 \end{pmatrix} = -\sqrt{\frac{1}{10}}\,.$$

With circular left polarized light, i.e. $q=$-1, the non-vanishing $3J$ symbols include:

$$\begin{pmatrix} 2 & 1 & 1 \\ 0 & -1 & 1 \end{pmatrix} = \sqrt{\frac{1}{30}}\,;$$

$$\begin{pmatrix} 2 & 1 & 1 \\ 1 & -1 & 0 \end{pmatrix} = -\sqrt{\frac{1}{10}}\,;$$

$$\begin{pmatrix} 2 & 1 & 1 \\ 2 & -1 & -1 \end{pmatrix} = \sqrt{\frac{1}{5}}\,.$$

With circular left polarized light, i.e. $q=+1$, they include:

$$\begin{pmatrix} 2 & 1 & 1 \\ -2 & 1 & 1 \end{pmatrix} = \sqrt{\frac{1}{5}}\,;$$

$$\begin{pmatrix} 2 & 1 & 1 \\ -1 & 1 & 0 \end{pmatrix} = -\sqrt{\frac{1}{10}}\,;$$

$$\begin{pmatrix} 2 & 1 & 1 \\ 0 & 1 & -1 \end{pmatrix} = \sqrt{\frac{1}{30}}\,.$$

A.2. Kramers-Kronig transformations

The real and imaginary part of the scattering factor ($f = f' + if''$) are not independent, but connected by the Kramers-Kronig relations, which can also be used for any complex function, as described in [77]. Regarding x-ray scattering factor ($f = f'+if''$), one cannot rely on the theoretical values since it is very sensitive to the chemical local environment. The imaginary part of the scattering factor f'' is directly related to the absorption coefficients σ_a through:

$$f'' = -\frac{\omega}{4\pi r_0 c}\sigma_a \tag{A.1}$$

The real part of the scattering factor f' is obtained from the Kramers-Kronig relations which are given by

$$\begin{aligned} f'(\omega) &= \frac{2}{\pi}\mathbf{P}\int_0^{+\infty} \frac{\omega' f''(\omega)}{(\omega'^2-\omega^2)}d\omega' \\ f''(\omega) &= -\frac{2\omega}{\pi}\mathbf{P}\int_0^{+\infty} \frac{f'(\omega)}{(\omega'^2-\omega^2)}d\omega', \end{aligned} \tag{A.2}$$

where **P** is the Cauchy principal value of the integral. The Kramers-Kronig relations are derived from Cauchy's theorem for complex integration from mathematical point of view.

Practically, one cannot integrate from 0 to $+\infty$. As mentioned in Sec. 2.1.3, the imaginary part of the scattering factor f'' is obtained by merging the experimental measure absorption spectra near resonant energies to the values from Chantler table within a range from $10\,eV$ to $400{,}000\,eV$. The numerical estimation of the equation is more complicated due to the singularity at $\omega' =$

ω, which is solved by a summarization of discrete parts as follows:

$$f'(\omega) = \frac{2}{\pi}\mathbf{P}\sum_{\omega_i}\frac{\omega' f''(\omega)}{(\omega'^2 - \omega_i^2)}d\omega'. \tag{A.3}$$

A.3. Scripts of layer-resolved orbital occupation modulation in Remagx simulation

```
for $i = 6, 26, 4$ do
   $\mathit{thickness}\ [i] = \mathit{thickness}\ [2]$
   $\mathit{sigma}\ [i] = \mathit{sigma}\ [2]$
   end

   for $i = 7, 29, 4$ do
   $\mathit{thickness}\ [i] = \mathit{thickness}\ [3]$
   $\mathit{sigma}\ [i] = \mathit{sigma}\ [3]$
   end

   for $i = 8, 28, 4$ do
   $\mathit{thickness}\ [i] = \mathit{thickness}\ [4]$
   $\mathit{sigma}\ [i] = \mathit{sigma}\ [4]$
   end

   for $i = 9, 29, 4$ do
   $\mathit{thickness}\ [i] = \mathit{thickness}\ [5]$
   $\mathit{sigma}\ [i] = \mathit{sigma}\ [5]$
   end

   $\mathit{epsilon} = 8\text{e-}6$
   for $i = 1, 29, 4$ do
   $e_{xx}\text{ - }r[i] = (1. - \mathit{delta}[1]) * (1. - \mathit{delta}[1]) - \mathit{beta}[1] * \mathit{beta}[1]$
   $e_{yy}\text{ - }r[i] = (1. - \mathit{delta}[1]) * (1. - \mathit{delta}[1]) - \mathit{beta}[1] * \mathit{beta}[1]$
   $e_{zz}\text{ - }r[i] = (1. - \mathit{delta}[5]) * (1. - \mathit{delta}[5]) - \mathit{beta}[5] * \mathit{beta}[5]$
   $e_{xx}\text{ - }i[i] = 2. * (1 - \mathit{delta}[1]) * \mathit{beta}[1]$
   $e_{yy}\text{ - }i[i] = 2. * (1 - \mathit{delta}[1]) * \mathit{beta}[1]$
   $e_{zz}\text{ - }i[i] = 2. * (1 - \mathit{delta}[5]) * \mathit{beta}[5]$
```

```
end

for $i = 3$, 27, 4 do
$e_{xx}$ - $r[i] = (1. - delta[3]) * (1. - delta[3]) - beta[3] * beta[3]$
$e_{yy}$ - $r[i] = (1. - delta[3]) * (1. - delta[3]) - beta[3] * beta[3]$
$e_{zz}$ - $r[i] = (1. - delta[7]) * (1. - delta[7]) - beta[7] * beta[7]$
$e_{xx}$ - $i[i] = 2.$ * $(1 - delta[3]) * beta[3]$
$e_{yy}$ - $i[i] = 2.$ * $(1 - delta[3]) * beta[3]$
$e_{zz}$ - $i[i] = 2.$ * $(1 - delta[7]) * beta[7]$
end

for $i = 4$, 28, 4 do
$e_{xx}$ - $r[i] = (1. - delta[4]) * (1. - delta[4]) - beta[4] * beta[4]$
$e_{yy}$ - $r[i] = (1. - delta[4]) * (1. - delta[4]) - beta[4] * beta[4]$
$e_{zz}$ - $r[i] = (1. - delta[8]) * (1. - delta[8]) - beta[8] * beta[8]$
$e_{xx}$ - $i[i] = 2.$ * $(1 - delta[4]) * beta[4]$
$e_{yy}$ - $i[i] = 2.$ * $(1 - delta[4]) * beta[4]$
$e_{zz}$ - $i[i] = 2.$ * $(1 - delta[8]) * beta[8]$
end

–ShowMatrixEigenvalues()
```

A.4. Scripts of octahedra rotation in Remagx simulation

```
– create 3x3 matrices
  – first index $i$ = row
  – second index $j$ = column
  – $R$: rotation matrix
  – $E_r$: epsilon tensor real part
  – $E_i$: epsilon tensor imaginary part
  – $T_r$: temporary matrix real part
  – $T_i$: temporary matrix imaginary part

  $R = \{\}$
  $E_r = \{\}$
  $E_i = \{\}$
  $T_r = \{\}$
```

```
$T_i = \{\}$

for $i = 1$, 3 do
$R[i] = \{\}$
$E_r[i] = \{\}$
$E_i[i] = \{\}$
$T_r[i] = \{\}$
$T_i[i] = \{\}$

for $j = 1$, 3 do
$R[i][j] = 0;$
$E_r[i][j] = 0;$
$E_i[i][j] = 0;$
$T_r[i][j] = 0;$
$T_i[i][j] = 0;$
end
end

– for each layer calculate $R * E * R_T$ ($R_T =$ transposed matrix of $R$)
for $l$ = 1, 31, 2 do
– define epsilon tensor
$delta_{xx} = delta[1];$
$beta_{xx} = beta[1];$
$delta_{zz} = delta[3];$
$beta_{zz} = beta[3];$
$delta_{yy} = (delta[1] + delta[3])$ * 0.5;
$beta_{yy} = (beta[1] + beta[3])$ * 0.5;

$E_r[1][1] =$ 1. - 2.$*delta_{xx} + delta_{xx} * delta_{xx}$ - $beta_{xx} * beta_{xx};$
$E_r[2][2] =$ 1. - 2.*$delta_{yy} + delta_{yy} * delta_{yy}$ - $beta_{yy} * beta_{yy};$
$E_r[3][3] =$ 1. - 2.*$delta_{zz} + delta_{zz} * delta_{zz}$ - $beta_{zz} * beta_{zz};$
$E_i[1][1] =$ 2.*beta$_{xx}$ - 2.*$delta_{xx} * beta_{xx};$
$E_i[2][2] =$ 2.*beta$_{yy}$ - 2.*$delta_{yy} * beta_{yy};$
$E_i[3][3] =$ 2.*$beta_{zz}$ - 2.*$delta_{zz} * beta_{zz};$

– define rotation matrix for each layer with a rotation angle of 10°
angle = $l$ / 36. * 2. * math.pi;
–print("angle of layer ", $l$, ": ", angle);
```

```
$R[1][1]$ = math.cos(angle);
$R[1][2]$ = math.sin(angle);
$R[2][1]$ = -math.sin(angle);
$R[2][2]$ = math.cos(angle);
$R[3][3] = 1.$;

– $T = R * E$
for $i = 1, 3$ do
  for $j = 1, 3$ do
    $T_r[i][j] = 0.$;
    $T_i[i][j] = 0.$;
    for $k = 1, 3$ do
      $T_r[i][j] = T_r[i][j] + R[i][k] * E_r[k][j]$;
      $T_i[i][j] = T_i[i][j] + R[i][k] * E_i[k][j]$;
    end
  end
end

– $E = T * R_T$
for $i = 1, 3$ do
  for $j = 1, 3$ do
    $E_r[i][j] = 0.$;
    $E_i[i][j] = 0.$;
    for $k = 1, 3$ do
      $E_r[i][j] = E_r[i][j] + T_r[i][k] * R[j][k]$;
      $E_i[i][j] = E_i[i][j] + T_i[i][k] * R[j][k]$;
end end end

– set epsilon tensor
$e_{xx}$ - $r[l] = E_r[1][1]$;
$e_{xy}$ - $r[l] = E_r[1][2]$;
$e_{xz}$ - $r[l] = E_r[1][3]$;
$e_{yx}$ - $r[l] = E_r[2][1]$;
$e_{yy}$ - $r[l] = E_r[2][2]$;
$e_{yz}$ - $r[l] = E_r[2][3]$;
$e_{zx}$ - $r[l] = E_r[3][1]$;
$e_{zy}$ - $r[l] = E_r[3][2]$;
$e_{zz}$ - $r[l] = E_r[3][3]$;
$e_{xx}$ - $i[l] = E_i[1][1]$;
```

```
$e_{xy}$ - $i[l] = E_i[1][2]$;
$e_{xz}$ - $i[l] = E_i[1][3]$;
$e_{yx}$ - $i[l] = E_i[2][1]$;
$e_{yy}$ - $i[l] = E_i[2][2]$;
$e_{yz}$ - $i[l] = E_i[2][3]$;
$e_{zx}$ - $i[l] = E_i[3][1]$;
$e_{zy}$ - $i[l] = E_i[3][2]$;
$e_{zz}$ - $i[l] = E_i[3][3]$;
end
```

Bibliography

[1] K. H. Ahn, T. Lookman, and A. R. Bishop. Strain-induced metal-insulator phase coexistence in perovskite manganites. *Nature*, 428:401–404, 2004. 91

[2] J. A. Alonso, M. J. Martínez-Lope, M. T. Casais, J. L. García-Muñoz, and M. T. Fernández-Díaz. Room-temperature monoclinic distortion due to charge disproportionation in $\mathrm{RNiO_3}$ perovskites with small rare-earth cations ($\mathrm{R = Ho, Y, Er, Tm, Yb}$, and Lu): A neutron diffraction study. *Phys. Rev. B*, 61:1756–1763, 2000. 10

[3] J. A. Alonso, M. J. Martínez-Lope, M. T. Casais, J. L. García-Muñoz, M. T. Fernández-Díaz, and M. A. G. Aranda. High-temperature structural evolution of $\mathrm{RNiO_3(R = Ho, Y, Er, Lu)}$ perovskites: Charge disproportionation and electronic localization. *Phys. Rev. B*, 64:094102, 2001. 10

[4] O. K. Andersen and T. Saha-Dasgupta. Muffin-tin orbitals of arbitrary order. *Phys. Rev. B*, 62:R16219–R16222, 2000. 79

[5] O. K. Andersen, T. Saha-Dasgupta, R. W. Tank, C. Arcangeli, O. Jepsen, and G. Krier. In H. Dreysse, editor, *Electronic Structure and Physical Properties of Solids. The Uses of the* LMTO *Method*. Springer, New York, 2000. 79

[6] A. Ankudinov and J. J. Rehr. Sum rules for polarization-dependent x-ray absorption. *Phys. Rev. B*, 51:1282–1285, 1995. 17

[7] C. Bell, S. Harashima, Y. Hikita, and H.Y. Hwang. Thickness dependence of the mobility at the $\mathrm{LaAlO_3/SrTiO_3}$ interface. *Applied Physics Letters*, 94(22):222111–222111–3, 2009. 8

[8] Eva Benckiser, Maurits W. Haverkort, Sebastian Brueck, Eberhard Goering, Sebastian Macke, Alex Frano, Xiaoping Yang, Ole K. Andersen, Georg Cristiani, Hanns-Ulrich Habermeier, Alexander V. Boris, Ioannis Zegkinoglou, Peter Wochner, Heon-Jung Kim, Vladimir Hinkov, and Bernhard Keimer. Orbital reflectometry of oxide heterostructures. *Nature Materials*, 10(3):189–193, 2011. 27, 68, 70, 72, 77, 82, 84, 85, 88, 142

[9] G. Berner, M. Sing, F. Pfaff, E. Benckiser, M. Wu, G. Christiani, G. Logvenov, H.-U. Habermeier, M. Kobayashi, V.N. Strocov, T. Schmitt, H. Fujiwara, S. Suga, A. Sekiyama, B. Keimer, and R. Claessen. Dimensionality-tuned electronic structure of nickelate superlattices explored by soft-x-ray angle resolved photoelectron spectroscopy. *arXiv:1411.7177*, 2014. 10

[10] A. Bhattacharya, S. J. May, S. G. E. te Velthuis, M. Warusawithana, X. Zhai, Bin Jiang, J.-M. Zuo, M. R. Fitzsimmons, S. D. Bader, and J. N. Eckstein. Metal-insulator transition and its relation to magnetic structure in $\mathrm{(LaMnO_3)_{2n}/(SrMnO_3)_n}$ superlattices. *Phys. Rev. Lett.*, 100:257203, 2008. 7

[11] Ariadna Blanca-Romero and Rossitza Pentcheva. Confinement-induced metal-to-insulator transition in strained $LaNiO_3 - LaAlO_3$ superlattices. *Phys. Rev. B*, 84:195450, 2011. 78, 101, 137, 141

[12] A. E. Bocquet, T. Mizokawa, T. Saitoh, H. Namatame, and A. Fujimori. Electronic structure of $3d$-transition-metal compounds by analysis of the $2p$ core-level photoemission spectra. *Phys. Rev. B*, 46:3771–3784, 1992. 3, 4, 39

[13] Y Bodenthin, U Staub, C Piamonteze, M García-Fernández, M J Martíŋnez-Lope, and J A Alonso. Magnetic and electronic properties of $RNiO_3$ ($R = Pr, Nd, Eu, Ho$ and Y) perovskites studied by resonant soft x-ray magnetic powder diffraction. *Journal of Physics: Condensed Matter*, 23(3):036002, 2011. 96

[14] A. V. Boris, Y. Matiks, E. Benckiser, A. Frano, P. Popovich, V. Hinkov, P. Wochner, M. Castro-Colin, E. Detemple, V. K. Malik, C. Bernhard, T. Prokscha, A. Suter, Z. Salman, E. Morenzoni, G. Cristiani, H.-U. Habermeier, and B. Keimer. Dimensionality control of electronic phase transitions in nickel-oxide superlattices. *Science*, 332(6032):937–940, 2011. 5, 12, 67

[15] Sebastian Brück, Steffen Bauknecht, Bernd Ludescher, Eberhard Goering, and Gisela Schütz. An advanced magnetic reflectometer. *Review of Scientific Instruments*, 79:0803109, 2008. 47

[16] G. Catalan. Progress in perovskite nickelate research. *Taylor & Francis*, 81:729–749, 2008. 9, 101

[17] J. Chakhalian, J. W. Freeland, H.-U. Habermeier, G. Cristiani, G. Khaliullin, M. van Veenendaal, and B. Keimer. Dimensionality control of electronic phase transitions in nickel-oxide superlattices. *Science*, 318(5853):1114–1117, 2007. 8, 52

[18] J. Chakhalian, J. W. Freeland, G. Srajer, J. Strempfer, G. Khaliullin, J. C. Cezar, T. Charlton, R. Dalgliesh, C. Bernhard, G. Cristiani, H.-U. Habermeier, and B. Keimer. Magnetism at the interface between ferromagnetic and superconducting oxides. *Nat Phys*, 2:244–248, 2007. 8

[19] J. Chakhalian, J. M. Rondinelli, Jian Liu, B. A. Gray, M. Kareev, E. J. Moon, N. Prasai, J. L. Cohn, M. Varela, I. C. Tung, M. J. Bedzyk, S. G. Altendorf, F. Strigari, B. Dabrowski, L. H. Tjeng, P. J. Ryan, and J. W. Freeland. Asymmetric orbital-lattice interactions in ultrathin correlated oxide films. *Phys. Rev. Lett.*, 107:116805, 2011. 12, 78, 79, 91, 93, 101

[20] Jiří Chaloupka and Giniyat Khaliullin. Orbital order and possible superconductivity in $LaNiO_3/LaMO_3$ superlattices. *Phys. Rev. Lett.*, 100:016404, 2008. 5, 8, 10, 83, 137, 141

[21] C. T. Chantler. Theoretical form factor, attenuation and scattering tabulation for $Z = 1 - 92$ from $E = 1 - 10eV$ to $E = 0.4 - 1.0MeV$. *J. Phys. Chem. Ref. Data*, 24:71–643, 1995. 31

[22] C. T. Chantler. Detailed tabulation of atomic form factors, photoelectric absorption and scattering cross section, and mass attenuation coefficients in the vicinity of absorption edges in the soft x-ray ($Z = 30 - 36$, $Z = 60 - 89$, $E = 0.1keV - 10keV$), addressing convergence issues of earlier work. *Journal of Physical and Chemical Reference Data*, 29(4):597–1056, 2000. 82

[23] K. J. Choi, M. Biegalski, Y. L. Li, A. Sharan, J. Schubert, R. Uecker, P. Reiche, Y. B. Chen, X. Q. Pan, V. Gopalan, L.-Q. Chen, D. G. Schlom, and C. B. Eom. Enhancement of ferroelectricity in strained $BaTiO_3$ thin films. *Science*, 306(5698):1005–1009, 2004. 101

[24] F. de Bergevin and M. Brunel. Observation of magnetic superlattice peaks by x-ray diffraction on an antiferromagnetic NiO crystal. *Physics Letters A*, 39(2):141 – 142, 1972. 15

[25] F. de Bergevin and M. Brunel. Diffraction of X-rays by magnetic materials. I. General formulae and measurements on ferro- and ferrimagnetic compounds. *Acta Crystallographica Section A*, 37(3):314–324, 1981. 15

[26] F. M. F. de Groot, J. C. Fuggle, B. T. Thole, and G. A. Sawatzky. $2p$ x-ray absorption of $3d$ transition-metal compounds: An atomic multiplet description including the crystal field. *Phys. Rev. B*, 42:5459–5468, 1990. 42, 76

[27] E. Detemple, Q. M. Ramasse, W. Sigle, G. Cristiani, H.-U. Habermeier, E. Benckiser, A. V. Boris, A. Frano, P. Wochner, M. Wu, B. Keimer, and P. A. van Aken. Polarity-driven nickel oxide precipitation in $lanio_3$-$laalo_3$ superlattices. *Applied Physics Letters*, 99(21):211903, 2011. 13, 56

[28] E. Detemple, Q. M. Ramasse, W. Sigle, G. Cristiani, H.-U. Habermeier, B. Keimer, and P. A. van Aken. Ruddlesden-popper faults in $LaNiO_3/LaAlO_3$ superlattices. *Journal of Applied Physics*, 112(1):013509, 2012. 13, 56

[29] P. Dhak, P. Pramanik, S. Bhattacharya, Anushree Roy, S. N. Achary, and A. K. Tyagi. Structural phase transition in lanthanum gallate as studied by raman and x-ray diffraction measurements. *physica status solidi (b)*, 248(8):1884–1893, 2011. 53

[30] D. A. Dikin, M. Mehta, C. W. Bark, C. M. Folkman, C. B. Eom, and V. Chandrasekhar. Coexistence of superconductivity and ferromagnetism in two dimensions. *Phys. Rev. Lett.*, 107:056802, 2011. 8

[31] Shuai Dong and Elbio Dagotto. Quantum confinement induced magnetism in $LaNiO_3 - LaMnO_3$ superlattices. *Phys. Rev. B*, 87:195116, 2013. 8

[32] N. Driza, S. Blanco-Canosa, M. Bakr, S. Soltan, M. Khalid, L. Mustafa, K. Kawashima, G. Christiani, H-U. Habermeier, G. Khaliullin, C. Ulrich, M. Le Tacon, and B. Keimer. Long-range transfer of electronŰphonon coupling in oxide superlattices. *Nature Materials*, 11:675–681, 2012. 8, 52

[33] A. Frano, E. Schierle, M. W. Haverkort, Y. Lu, M. Wu, S. Blanco-Canosa, U. Nwankwo, A. V. Boris, P. Wochner, G. Cristiani, H. U. Habermeier, G. Logvenov, V. Hinkov, E. Benckiser, E. Weschke, and B. Keimer. Orbital control of noncollinear magnetic order in nickel oxide heterostructures. *Phys. Rev. Lett.*, 111:106804, 2013. 5, 12, 16, 27, 67

[34] Alex Frano, Eva Benckiser, Yi Lu, Meng Wu, Miguel Castro-Colin, Manfred Reehuis, Alexander V. Boris, Eric Detemple, Wilfried Sigle, Peter van Aken, Georg Cristiani, Gennady Logvenov, Hanns-Ulrich Habermeier, Peter Wochner, Bernhard Keimer, and Vladimir Hinkov. Layer selective control of the lattice structure in oxide superlattices. *Advanced Materials*, pages 258–262, 2013. 7, 13, 56, 101

[35] J. W. Freeland, J. Chakhalian, A. V. Boris, J.-M. Tonnerre, J. J. Kavich, P. Yordanov, S. Grenier, P. Zschack, E. Karapetrova, P. Popovich, H. N. Lee, and B. Keimer. Charge transport and magnetization profile at the interface between the correlated metal $CaRuO_3$ and the antiferromagnetic insulator $CaMnO_3$. *Phys. Rev. B*, 81:094414, 2010. 7

[36] J. W. Freeland, Jian Liu, M. Kareev, B. Gray, J. W. Kim, P. Ryan, R. Pentcheva, and J. Chakhalian. Orbital control in strained ultra-thin $LaNiO_3/LaAlO_3$ superlattices. *EPL (Europhysics Letters)*, 96(5):57004, 2011. 12, 78, 79, 91, 101

[37] Atsushi Fujimori and Fujio Minami. Valence-band photoemission and optical absorption in nickel compounds. *Phys. Rev. B*, 30:957–971, 1984. 3

[38] Guanyin Gao, Zhizhen Yin, Zhen Huang, Shaowei Jin, and Wenbin Wu. The thickness evolution of orthorhombic lattice distortions in heteroepitaxial $La_{0.67}Ca_{0.33}MnO_3/NdGaO_3$ (110) or observed by x-ray reciprocal space mapping. *Journal of Physics D: Applied Physics*, 41(15):152001, 2008. 63

[39] Yuze Gao, Guixin Cao, Jincang Zhang, and Hanns-Ulrich Habermeier. Intrinsic and precipitate-induced quantum corrections to conductivity in $La_{2/3}Sr_{1/3}MnO_3$ thin films. *Phys. Rev. B*, 85:195128, 2012. 66

[40] J. L. García-Muñoz, J. Rodríguez-Carvajal, and P. Lacorre. Neutron-diffraction study of the magnetic ordering in the insulating regime of the perovskites $RNiO_3$ (R = Pr and Nd). *Phys. Rev. B*, 50:978–992, 1994. 79, 80, 102

[41] G. Ghiringhelli, M. Le Tacon, M. Minola, S. Blanco-Canosa, C. Mazzoli, N. B. Brookes, G. M. De Luca, A. Frano, D. G. Hawthorn, F. He, T. Loew, M. Moretti Sala, D. C. Peets, M. Salluzzo, E. Schierle, R. Sutarto, G. A. Sawatzky, E. Weschke, B. Keimer, and L. Braicovich. Long-range incommensurate charge fluctuations in $(Y,Nd)Ba_2Cu_3O_{6+x}$. *Science*, 337(6096):821–825, 2012. 16

[42] Marta Gibert, Pavlo Zubko, Raoul Scherwitzl, Jorge Íñiguez, and Jean-Marc Triscone. Exchange bias in $LaNiO_3LaMnO_3$ superlattices. *Nat. Mater.*, 11:195–198, 2012. 8

[43] A. M. Glazer. Simple ways of determining perovskite structures. *Acta Crystallographica Section A*, 31(6):756–762, 1975. 5, 6, 7, 52

[44] A. Gozar, G. Logvenov, L. Fitting Kourkoutis, A. T. Bollinger, L. A. Giannuzzi, D. A. Muller, and I. Bozovic. High-temperature interface superconductivity between metallic and insulating copper oxides. *Nature*, 455:782–785, 2008. 8

[45] X. Granados, J. Fontcuberta, X. Obradors, Ll. Mañosa, and J. B. Torrance. Metallic state and the metal-insulator transition of $NdNO_3$. *Phys. Rev. B*, 48:11666–11672, 1993. 9, 10

[46] Frank de Groot. Multiplet effects in x-ray spectroscopy. *Coordination Chemistry Reviews*, 249:31 – 63, 2005. Synchrotron Radiation in Inorganic and Bioinorganic Chemistry. 39

[47] J. H. Haeni, P. Irvin, W. Chang, R. Uecker, P. Reiche, Y. L. Li, S. Choudhury, W. Tian, M. E. Hawley, B. Craigo, A. K. Tagantsev, X. Q. Pan, S. K. Streiffer, L. Q. Chen, S. W. Kirchoefer, J. Levy, and D. G. Schlom. Room-temperature ferroelectricity in strained $SrTiO_3$. *Nature*, 430:758–761, 2004. 101

[48] M. J. Han, C. A. Marianetti, and A. J. Millis. Chemical control of orbital polarization in artificially structured transition-metal oxides: $La_2NiXO_6(X = B, Al, Ga, In)$ from first principles. *Phys. Rev. B*, 82:134408, 2010. 10, 11, 78, 79, 80, 81, 83, 91, 137, 141

[49] M. J. Han, Xin Wang, C. A. Marianetti, and A. J. Millis. Dynamical mean-field theory of nickelate superlattices. *Phys. Rev. Lett.*, 107:206804, 2011. 10, 11, 78, 79, 80, 81, 83, 92, 137, 141

[50] M. J. Han, Xin Wang, C. A. Marianetti, and A. J. Millis. Erratum: Dynamical mean-field theory of nickelate superlattices [phys. rev. lett. 107, 206804 (2011)]. *Phys. Rev. Lett.*, 110:179904, 2013. 80

[51] Myung Joon Han and Michel van Veenendaal. Spin-moment formation and reduced orbital polarization in $LaNiO_3/LaAlO_3$ superlattice: LDA + U study. *Phys. Rev. B*, 85:195102, 2012. 78, 83, 137, 141

[52] P. Hansmann, A. Toschi, Xiaoping Yang, O. K. Andersen, and K. Held. Electronic structure of nickelates: From two-dimensional heterostructures to three-dimensional bulk materials. *Phys. Rev. B*, 82:235123, 2010. 78, 81, 83, 91, 137, 141

[53] P. Hansmann, Xiaoping Yang, A. Toschi, G. Khaliullin, O. K. Andersen, and K. Held. Turning a nickelate fermi surface into a cupratelike one through heterostructuring. *Phys. Rev. Lett.*, 103:016401, 2009. 5, 8, 10, 11, 78, 80, 81, 83, 91, 137, 141

[54] M. W. Haverkort. *spin and orbit degrees of freedom in transition metal oxides and oxide thin film studied by x ray absorption spectroscopy.* PhD thesis, 2005. 17, 39, 41, 42

[55] M. W. Haverkort, S. I. Csiszar, Z. Hu, S. Altieri, A. Tanaka, H. H. Hsieh, H.-J. Lin, C. T. Chen, T. Hibma, and L. H. Tjeng. Magnetic versus crystal-field linear dichroism in NiO thin films. *Phys. Rev. B*, 69:020408, 2004. 95

[56] M. W. Haverkort, N. Hollmann, I. P. Krug, and A. Tanaka. Symmetry analysis of magneto-optical effects: The case of x-ray diffraction and x-ray absorption at the transition metal $L_{2,3}$ edge. *Phys. Rev. B*, 82:094403, 2010. 27

[57] M. W. Haverkort, M. Zwierzycki, and O. K. Andersen. Multiplet ligand-field theory using wannier orbitals. *Phys. Rev. B*, 85:165113, 2012. 39, 80

[58] S. A. Hayward, F. D. Morrison, S. A. T. Redfern, E. K. H. Salje, J. F. Scott, K. S. Knight, S. Tarantino, A. M. Glazer, V. Shuvaeva, P. Daniel, M. Zhang, and M. A. Carpenter. Transformation processes in $LaAlO_3$: Neutron diffraction, dielectric, thermal, optical, and raman studies. *Phys. Rev. B*, 72:054110, 2005. 10, 53, 54

[59] B.L. Henke, E. M. Gullikson, and J. C. Davis. X-ray interactions: photoabsorption, scattering, transmission and reflection at $E = 50 - 30,000$eV, $Z = 1 - 92$. *Atomic Data and Nuclear Data Tables*, 54:181–342, 1993. 31

[60] M. Hepting, M. Minola, A. Frano, G. Cristiani, G. Logvenov, E. Schierle, M. Wu, M. Bluschke, E. Weschke, H.U. Habermeier, E. Benckiser, M. Le Tacon, and B. Keimer. Tunable charge and spin order in $PrNiO_3$ thin films and superlattices. *Phys. Rev. Lett.*, 113:227206, 2014. 13, 66, 91, 93, 139, 143, 144

[61] G. Herranz, M. Basletić, M. Bibes, C. Carrétéro, E. Tafra, E. Jacquet, K. Bouzehouane, C. Deranlot, A. Hamzić, J.-M. Broto, A. Barthélémy, and A. Fert. High mobility in $\mathrm{LaAlO_3-SrTiO_3}$ heterostructures: Origin, dimensionality, and perspectives. *Phys. Rev. Lett.*, 98:216803, 2007. 8

[62] T. Higuchi, Y. Hotta, T. Susaki, A. Fujimori, and H. Y. Hwang. Modulation doping of a mott quantum well by a proximate polar discontinuity. *Phys. Rev. B*, 79:075415, 2009. 8

[63] S. A. Howard, J. K. Yau, and H. U. Anderson. Structural characteristics of $\mathrm{Sr_{1-x}La_xTi_{3+\delta}}$ as a function of oxygen partial pressure at 1400°C. *Journal of Applied Physics*, 65(4), 1989. 53, 54

[64] J. Hubbard. Electron correlations in narrow energy bands. ii. the degenerate band case. *Proceedings of the Royal Society of London. Series A. Mathematical and Physical Sciences*, 277(1369):237–259, 1964. 3

[65] H. Y. Hwang, Y. Iwasa, M. Kawasaki, B. Keimer, N. Nagaosa, and Y. Tokura. Emergent phenomena at oxide interfaces. *Nature Materials*, 11:103–113, 2012. 7

[66] Jinwoo Hwang, Junwoo Son, Jack Y. Zhang, Anderson Janotti, Chris G. Van de Walle, and Susanne Stemmer. Structural origins of the properties of rare earth nickelate superlattices. *Phys. Rev. B*, 87:060101, 2013. 13

[67] Masatoshi Imada, Atsushi Fujimori, and Yoshinori Tokura. Metal-insulator transitions. *Rev. Mod. Phys.*, 70:1039–1263, 1998. 3

[68] Des McMorrow Jens Als-Nielsen. *Elements of Modern X-ray Physics (Second Edition), ISBN 9781119998365.* Wiley, 2011. 32

[69] C. L. Jia, S. B. Mi, M. Faley, U. Poppe, J. Schubert, and K. Urban. Oxygen octahedron reconstruction in the $\mathrm{SrTiO_3-LaAlO_3}$ heterointerfaces investigated using aberration-corrected ultrahigh-resolution transmission electron microscopy. *Phys. Rev. B*, 79:081405, 2009. 101

[70] Takeo Jo. X-ray magnetic circular dichroism, symmetry and orbital magnetization. *Journal of the Physical Society of Japan*, 62(5):1814–1815, 1993. 17

[71] Steve Johnston, Anamitra Mukherjee, Ilya Elfimov, Mona Berciu, and George A. Sawatzky. Charge disproportionation without charge transfer in the rare-earth-element nickelates as a possible mechanism for the metal-insulator transition. *Phys. Rev. Lett.*, 112:106404, 2014. 4, 10, 93, 101

[72] A. P. Jones, F. Wall, and C. T. Williams. *Rare Earth Minerals - Chemistry, Origin and Ore Deposits, ISBN 978-0-412-61030-1.* Springer, 1996. 5

[73] Alexey Kalabukhov, Robert Gunnarsson, Johan Börjesson, Eva Olsson, Tord Claeson, and Dag Winkler. Effect of oxygen vacancies in the $\mathrm{SrTiO_3}$ substrate on the electrical properties of the $\mathrm{LaAlO_3-SrTiO_3}$ interface. *Phys. Rev. B*, 75:121404, 2007. 8

[74] M. Kareev, S. Prosandeev, J. Liu, C. Gan, A. Kareev, Min Freeland, J. W. Xiao, and J. Chakhalian. Atomic control and characterization of surface defect states of $\mathrm{TiO_2}$ terminated $\mathrm{SrTiO_3}$ single crystals. *Applied Physics Letters*, 93:061909, 2008. 55

[75] X. Ke, C. Adamo, D. G. Schlom, M. Bernhagen, R. Uecker, and P. Schiffer. Low temperature magnetism in the perovskite substrate $DyScO_3$. *Applied Physics Letters*, 94(15):–, 2009. 84

[76] M. K. Kinyanjui, Y. Lu, N. Gauquelin, M. Wu, A. Frano, P. Wochner, M. Reehuis, G. Christiani, G. Logvenov, H.-U. Habermeier, G. A. Botton, U. Kaiser, B. Keimer, and E. Benckiser. Lattice distortions and octahedral rotations in epitaxially strained $LaNiO_3$/LaAlO3 superlattices. *Applied Physics Letters*, 104(22):–, 2014. 102

[77] R. DE L. KRONIG. On the theory of dispersion of x-rays. *J. Opt. Soc. Am.*, 12(6):547–556, 1926. 114

[78] H. Kronmüller and S. Parkin. *Handbook of magnetism and advanced magnetic materials, ISBN 978-0-470-02217-7.* 2007. 5

[79] Ashvani Kumar, Preetam Singh, Davinder Kaur, John Jesudasan, and Pratap Raychaudhuri. Substrate effect on electrical transport properties of $RNiO_3$ thin films prepared by pulsed laser deposition. *Journal of Physics D: Applied Physics*, 39, 2006. 13, 101

[80] Patrick A. Lee and T. V. Ramakrishnan. Disordered electronic systems. *Rev. Mod. Phys.*, 57:287–337, 1985. 66

[81] SungBin Lee, Ru Chen, and Leon Balents. Landau theory of charge and spin ordering in the nickelates. *Phys. Rev. Lett.*, 106:016405, 2011. 10, 13

[82] SungBin Lee, Ru Chen, and Leon Balents. Metal-insulator transition in a two-band model for the perovskite nickelates. *Phys. Rev. B*, 84:165119, 2011. 10, 13

[83] Lu Li, C. Richter, J. Mannhart, and R. C. Ashoori. Tunable quasi-two-dimensional electron gases in oxide heterostructures. *Nature Physics*, 7:762Ũ766, 2011. 8

[84] Ruslan P. Liferovich and Roger H. Mitchell. A structural study of ternary lanthanide orthoscandate perovskites. *Journal of Solid State Chemistry*, 177(6):2188 – 2197, 2004. 53

[85] Jian Liu, M. Kareev, B. Gray, J. W. Kim, P. Ryan, B. Dabrowski, J. W. Freeland, and J. Chakhalian. Strain-mediated metal-insulator transition in epitaxial ultrathin films of $NdNiO_3$. *Applied Physics Letters*, 96(23):–, 2010. 13, 101

[86] Jian Liu, Mehdi Kargarian, Mikhail Kareev, Ben Gray, Phil J. Ryan, Alejandro Cruz, Nadeem Tahir, Yi-De Chuang, James M. Guo, Jinghua Rondinelli, John W. Freeland, Gregory A. Fiete, and Jak Chakhalian. Heterointerface engineered electronic and magnetic phases of $NdNiO_3$ thin films. *Nat. Commun.*, 4:2714, 2013. 13, 101

[87] Jian Liu, S. Okamoto, M. van Veenendaal, M. Kareev, B. Gray, P. Ryan, J. W. Freeland, and J. Chakhalian. Quantum confinement of mott electrons in ultrathin $LaNiO_3$/$LaAlO_3$ superlattices. *Phys. Rev. B*, 83:161102, 2011. 12

[88] Y. Lu. Structural and electronic properties of perovskite rare earth nickelate superlattices. Master's thesis, 2012. 7, 102

[89] A. H. MacDonald and M. Tsoi. Antiferromagnetic metal spintronics. *Philosophical Transactions of the Royal Society A: Mathematical, Physical and Engineering Sciences*, 369(1948):3098–3114, 2011. 13

[90] S. Macke. *ReMagX x-ray magnetic reflectivity tool - http://remagx.org.* 71, 72, 98

[91] Y. Matsushita, H. Bluhm, T. H. Geballe, and I. R. Fisher. Evidence for charge kondo effect in superconducting Tl-doped PbTe. *Phys. Rev. Lett.*, 94:157002, 2005. 66

[92] S. J. May, J.-W. Kim, J. M. Rondinelli, E. Karapetrova, N. A. Spaldin, A. Bhattacharya, and P. J. Ryan. Quantifying octahedral rotations in strained perovskite oxide films. *Phys. Rev. B*, 82:014110, 2010. 7, 13, 52, 101, 102

[93] I. I. Mazin, D. I. Khomskii, R. Lengsdorf, J. A. Alonso, W. G. Marshall, R. M. Ibberson, A. Podlesnyak, M. J. Martínez-Lope, and M. M. Abd-Elmeguid. Charge ordering as alternative to jahn-teller distortion. *Phys. Rev. Lett.*, 98:176406, 2007. 94, 140, 144

[94] M. Medarde, C. Dallera, M. Grioni, B. Delley, F. Vernay, J. Mesot, M. Sikora, J. A. Alonso, and M. J. Martínez-Lope. Charge disproportionation in $RNiO_3$ perovskites (R = *rare*earth) from high-resolution x-ray absorption spectroscopy. *Phys. Rev. B*, 80:245105, 2009. 10

[95] M. Medarde, M. T. Fernández-Díaz, and Ph. Lacorre. Long-range charge order in the low-temperature insulating phase of $PrNiO_3$. *Phys. Rev. B*, 78:212101, 2008. 10

[96] M. Medarde, A. Fontaine, J. L. Garcia-Munoz, J. Rodriguez-Carvajal, M. de Santis, M. Sacchi, G. Rossi, and P. Lacorre. $RNiO_3$: Nickel valence and the metal-insulator transition investigated by x-ray-absorption spectroscopy. *Phys. Rev. B*, 46:14975–14984, 1992. 95

[97] M. Medarde, J. Mesot, P. Lacorre, S. Rosenkranz, P. Fischer, and K. Gobrecht. High-pressure neutron-diffraction study of the metallization process in $PrNiO_3$. *Phys. Rev. B*, 52:9248–9258, 1995. 54

[98] María Luisa Medarde. Structural, magnetic and electronic properties of $RNiO_3$ perovskites (R = rare earth). *Journal of Physics: Condensed Matter*, 9(8):1679, 1997. 95

[99] T. Mizokawa and A. Fujimori. Electronic structure and orbital ordering in perovskite-type 3*d* transition-metal oxides studied by hartree-fock band-structure calculations. *Phys. Rev. B*, 54:5368–5380, 1996. 3, 41

[100] T. Mizokawa, A. Fujimori, T. Arima, Y. Tokura, N. Mōri, and J. Akimitsu. Electronic structure of $PrNiO_3$ studied by photoemission and x-ray-absorption spectroscopy: Band gap and orbital ordering. *Phys. Rev. B*, 52:13865–13873, 1995. 4, 93

[101] T. Mizokawa, D. I. Khomskii, and G. A. Sawatzky. Spin and charge ordering in self-doped mott insulators. *Phys. Rev. B*, 61:11263–11266, 2000. 4, 93

[102] N. F. Mott. The basis of the electron theory of metals, with special reference to the transition metals. *Proceedings of the Physical Society. Section A*, 62(7):416, 1949. 3

[103] David A. Muller. Structure and bonding at the atomic scale by scanning transmission electron microscopy. *Nat Mater*, 8:263–270, 2004. 101

[104] Névot, L. and Croce, P. Caractérisation des surfaces par réflexion rasante de rayons x. application álêtude du polissage de quelques verres silicates. *Rev. Phys. Appl. (Paris)*, 15(3):761–779, 1980. 35

[105] J. F. NYE. *Physical Properties of Crystals: Their Representation by Tensors and Matrices.* 1985. 27

[106] A. Ohtomo and H. Y. Hwang. A high-mobility electron gas at the $LaAlO_3/SrTiO_3$ heterointerface. *Nature*, 427:423–426, 2004. 7

[107] N. Parragh, G. Sangiovanni, P. Hansmann, S. Hummel, K. Held, and A. Toschi. Effective crystal field and fermi surface topology: A comparison of d- and dp-orbital models. *Phys. Rev. B*, 88:195116, 2013. 11, 92

[108] L. G. Parratt. Surface studies of solids by total reflection of x-rays. *Phys. Rev.*, 95:359–369, 1954. 32

[109] L. G. Parratt and C. F. Hempstead. Anomalous dispersion and scattering of x-rays. *Phys. Rev.*, 94:1593–1600, 1954. 32

[110] Dorota A. Pawlak, Masahiko Ito, Lukasz Dobrzycki, Krzysztof Wozniak, Masaoki Oku, Kiyoshi Shimamura, and Tsuguo Fukuda. Structure and spectroscopic properties of $(AA')(BB')O_3$ mixed-perovskite crystals. *Journal of Materials Research*, null:3329–3337, 2005. 54

[111] Oleg E. Peil, Michel Ferrero, and Antoine Georges. Orbital polarization in strained $LaNiO_3$: Structural distortions and correlation effects. *Phys. Rev. B*, 90:045128, 2014. 81, 90, 91, 92, 99, 140, 144

[112] C. Piamonteze, F. M. F. de Groot, H. C. N. Tolentino, A. Y. Ramos, N. E. Massa, J. A. Alonso, and M. J. Martínez-Lope. Spin-orbit-induced mixed-spin ground state in $RNiO_3$ perovskites probed by x-ray absorption spectroscopy: Insight into the metal-to-insulator transition. *Phys. Rev. B*, 71:020406, 2005. 93, 139, 144

[113] P. G. Radaelli, D. E. Cox, M. Marezio, and S-W. Cheong. Charge, orbital, and magnetic ordering in $La_{0.5}Ca_{0.5}MnO_3$. *Phys. Rev. B*, 55:3015–3023, 1997. 5

[114] N. Reyren, S. Thiel, A. D. Caviglia, L. Fitting Kourkoutis, G. Hammer, C. Richter, C. W. Schneider, T. Kopp, A.-S. Rüetschi, D. Jaccard, M. Gabay, D. A. Muller, J.-M. Triscone, and J. Mannhart. Superconducting interfaces between insulating oxides. *Science*, 317(5842):1196–1199, 2007. 8

[115] James M. Rondinelli and Craig J. Fennie. Octahedral rotation-induced ferroelectricity in cation ordered perovskites. *Advanced Materials*, 24(15):1961–1968, 2012. 12, 101

[116] James M. Rondinelli and Nicola A. Spaldin. Structural effects on the spin-state transition in epitaxially strained $LaCoO_3$ films. *Phys. Rev. B*, 79:054409, 2009. 12, 101, 138, 143

[117] James M. Rondinelli and Nicola A. Spaldin. Structure and properties of functional oxide thin films: Insights from electronic-structure calculations. *Advanced Materials*, 23(30):3363–3381, 2011. 101, 138, 143

[118] N. L Ross, J Zhao, and R. J Angel. High-pressure single-crystal x-ray diffraction study of $YAlO_3$ perovskite. *Journal of Solid State Chemistry*, 177(4-5):1276 – 1284, 2004. 53

[119] Andreas Rüegg and Gregory A. Fiete. Topological insulators from complex orbital order in transition-metal oxides heterostructures. *Phys. Rev. B*, 84:201103, 2011. 8

[120] J. J. Sakurai and Jim J. Napolitano. *Modern Quantum Mechanics (2nd Edition), ISBN 0-201-53929-2.* Addison Wesley, 1994. 18

[121] D. K. Satapathy, M. A. Uribe-Laverde, I. Marozau, V. K. Malik, S. Das, Th. Wagner, C. Marcelot, J. Stahn, S. Brück, A. Rühm, S. Macke, T. Tietze, E. Goering, A. Frañó, J. H. Kim, M. Wu, E. Benckiser, B. Keimer, A. Devishvili, B. P. Toperverg, M. Merz, P. Nagel, S. Schuppler, and C. Bernhard. Magnetic proximity effect in $YBa_2Cu_3O_7/La_{2/3}Ca_{1/3}MnO_3$ and $YBa_2Cu_3O_7/LaMnO_{3+\delta}$ superlattices. *Phys. Rev. Lett.*, 108:197201, 2012. 8

[122] V. Scagnoli, U. Staub, Y. Bodenthin, M. Garcia-Fernandez, A. M. Mulders, G. I. Meijer, and G. Hammerl. Induced noncollinear magnetic order of Nd^{3+} in $NdNiO_3$ observed by resonant soft x-ray diffraction. *Phys. Rev. B*, 77:115138, 2008. 10

[123] V. Scagnoli, U. Staub, M. Janousch, A. M. Mulders, M. Shi, G. I. Meijer, S. Rosenkranz, S. B. Wilkins, L. Paolasini, J. Karpinski, S. M. Kazakov, and S. W. Lovesey. Charge disproportionation and search for orbital ordering in $NdNiO_3$ by use of resonant x-ray diffraction. *Phys. Rev. B*, 72:155111, 2005. 10, 16, 27

[124] C. Schüßler-Langeheine, J. Schlappa, A. Tanaka, Z. Hu, C. F. Chang, E. Schierle, M. Benomar, H. Ott, E. Weschke, G. Kaindl, O. Friedt, G. A. Sawatzky, H.-J. Lin, C. T. Chen, M. Braden, and L. H. Tjeng. Spectroscopy of stripe order in $La_{1.8}Sr_{0.2}NiO_4$ using resonant soft x-ray diffraction. *Phys. Rev. Lett.*, 95:156402, 2005. 41, 42

[125] R. D. Shannon. Revised effective ionic radii and systematic studies of interatomie distances in halides and chaleogenides. *Acta Cryst.*, A32:751, 1976. 82

[126] R. D. Shannon, R. A. Oswald, J. B. Parise, B. H. T. Chai, P. Byszewski, A. Pajaczkowska, and R. Sobolewski. Dielectric constants and crystal structures of $CaYAlO_4$, $CaNdAlO_4$, and $SrLaAlO_4$, and deviations from the oxide additivity rule. *Journal of Solid State Chemistry*, 98(1):90 – 98, 1992. 53, 54

[127] S. K. Sinha, E. B. Sirota, S. Garoff, and H. B. Stanley. X-ray and neutron scattering from rough surfaces. *Phys. Rev. B*, 38:2297–2311, 1988. 88

[128] Jairo Sinova and Igor Zutic. New moves of the spintronics tango. *Nature Materials*, 11:368–371, 2012. 13

[129] J. C. Slater and G. F. Koster. Simplified LCAO method for the periodic potential problem. *Phys. Rev.*, 94:1498–1524, 1954. 41

[130] S. Smadici, J. C. T. Lee, S. Wang, P. Abbamonte, G. Logvenov, A. Gozar, C. Deville Cavellin, and I. Bozovic. Superconducting transition at 38 K in insulating-overdoped $La_2CuO_4 - La_{1.64}Sr_{0.36}CuO_4$ superlattices: Evidence for interface electronic redistribution from resonant soft x-ray scattering. *Phys. Rev. Lett.*, 102:107004, 2009. 8

[131] St˙ Exploring the microscopic origin of magnetic anisotropies with x-ray magnetic circular dichroism (xmcd) spectroscopy. *Journal of Magnetism and Magnetic Materials*, 200:470 – 497, 1999. 48

[132] U. Staub, G. I. Meijer, F. Fauth, R. Allenspach, J. G. Bednorz, J. Karpinski, S. M. Kazakov, L. Paolasini, and F. d'Acapito. Direct observation of charge order in an epitaxial $NdNiO_3$ film. *Phys. Rev. Lett.*, 88:126402, 2002. 10, 16

[133] K. S. Takahashi, M. Kawasaki, and Y. Tokura. Interface ferromagnetism in oxide superlattices of $CaMnO_3/CaRuO_3$. *Applied Physics Letters*, 79(9), 2001. 7

[134] M. Takizawa, Y. Hotta, T. Susaki, Y. Ishida, H. Wadati, Y. Takata, K. Horiba, M. Matsunami, S. Shin, M. Yabashi, K. Tamasaku, Y. Nishino, T. Ishikawa, A. Fujimori, and H. Y. Hwang. Spectroscopic evidence for competing reconstructions in polar multilayers $LaAlO_3/LaVO_3/LaAlO_3$. *Phys. Rev. Lett.*, 102:236401, 2009. 8

[135] Arata Tanaka and Takeo Jo. Resonant $3d$, $3p$ and $3s$ photoemission in transition metal
oxides predicted at $2p$ threshold. *Journal of the Physical Society of Japan*, 63(7):2788–2807, 1994. 41

[136] S. Thiel, G. Hammerl, A. Schmehl, C. W. Schneider, and J. Mannhart. Tunable quasi-two-dimensional electron gases in oxide heterostructures. *Science*, 313(5795):1942–1945, 2006. 8

[137] Y. Tokura and N. Nagaosa. Orbital physics in transition-metal oxides. *Science*, 288(5465):462–468, 2000. 5, 91

[138] J. B. Torrance, P. Lacorre, A. I. Nazzal, E. J. Ansaldo, and Ch. Niedermayer. Systematic study of insulator-metal transitions in perovskites $RNiO_3(R = Pr, Nd, Sm, Eu)$ due to closing of charge-transfer gap. *Phys. Rev. B*, 45:8209–8212, 1992. 9

[139] G. van der Laan. Sum rules and fundamental spectra of magnetic x-ray dichroism in crystal field symmetry. *Journal of the Physical Society of Japan*, 63(6):2393–2400, 1994. 68

[140] G. van der Laan, C. Westra, C. Haas, and G. A. Sawatzky. Satellite structure in photoelectron and auger spectra of copper dihalides. *Phys. Rev. B*, 23:4369–4380, 1981. 39

[141] G. van der Laan, J. Zaanen, G. A. Sawatzky, R. Karnatak, and J.-M. Esteva. Comparison of x-ray absorption with x-ray photoemission of nickel dihalides and NiO. *Phys. Rev. B*, 33:4253–4263, 1986. 39

[142] David I. Woodward and Ian M. Reaney. Electron diffraction of tilted perovskites. *Acta Crystallographica Section B*, 61(4):387–399, 2005. 101

[143] Hiroyuki Yamada, M. Kawasaki, T. Lottermoser, T. Arima, and Y. Tokura. $LaMnO_3 - SrMnO_3$ interfaces with coupled charge-spin-orbital modulation. *Applied Physics Letters*, 89(5):–, 2006. 7

[144] J. Yang. Structural analysis of perovskite $LaCr_{1-x}Ni_xO_3$ by rietveld refinement of x-ray powder diffraction data. *Acta Cryst.*, B64:281–286, 2008. 53

[145] Kai-Yu Yang, Wenguang Zhu, Di Xiao, Satoshi Okamoto, Ziqiang Wang, and Ying Ran. Possible interaction-driven topological phases in (111) bilayers of $LaNiO_3$. *Phys. Rev. B*, 84:201104, 2011. 8

[146] X. Yang, P. Hansmann, A. Toschi, K. Held, G. Khaliullin, and O. K. Andersen. unpublished; see also O. K. Andersen, APS March Meeting, (Pittsburgh, Pennsylvania, 2009). 83

[147] H. K. Yoo, S. I. Hyun, L. Moreschini, H. D. Kim, Y. J. Chang, C. H. Sohn, D. W. Jeong, S. Sinn, Y. S. Kim, A. Bostwick, E. Rotenberg, J. H. Shim, and T. W. Noh. Latent instabilities in metallic $LaNiO_3$ films by strain control of fermi-surface topology. *arXiv:1406.2433*, 2014. 10

[148] P. Yordanov, A. V. Boris, J. W. Freeland, J. J. Kavich, J. Chakhalian, H. N. Lee, and B. Keimer. Far-infrared and dc magnetotransport of $CaMnO_3 - CaRuO_3$ superlattices. *Phys. Rev. B*, 84:045108, 2011. 7

[149] J. Zaanen, G. A. Sawatzky, and J. W. Allen. Band gaps and electronic structure of transition-metal compounds. *Phys. Rev. Lett.*, 55:418–421, 1985. 4

[150] J. Zak, E. R. Moog, C. Liu, and S. D. Bader. Magneto-optics of multilayers with arbitrary magnetization directions. *Phys. Rev. B*, 43:6423–6429, 1991. 37, 38

[151] J. Zak, E.R. Moog, C. Liu, and S.D. Bader. Universal approach to magneto-optics. *Journal of Magnetism and Magnetic Materials*, 89(1-2):107 – 123, 1990. 37, 38

[152] A. Zayak, X. Huang, J. Neaton, and Karin Rabe. Structural, electronic, and magnetic properties of $SrRuO_3$ under epitaxial strain. *Phys. Rev. B*, 74:094104, 2006. 101

[153] Jing Zhao, Nancy L Ross, Ross J Angel, Michael A Carpenter, Christopher J Howard, Dorota A Pawlak, and Tadeusz Lukasiewicz. High-pressure crystallography of rhombohedral $PrAlO_3$ perovskite. *Journal of Physics: Condensed Matter*, 21(23):235403, 2009. 54

[154] P. Zubko, N. Stucki, C. Lichtensteiger, and J.-M. Triscone. X-ray diffraction studies of 180° ferroelectric domains in $PbTiO_3/SrTiO_3$ superlattices under an applied electric field. *Phys. Rev. Lett.*, 104:187601, 2010. 52

Abbreviations

TMOs	transition metal oxides
LDA	local density approximation
DFT	density functional theory
MIT	metal-insulator transition
LNO	$LaNiO_3$
LAO	$LaAlO_3$
STO	$SrTiO_3$
LGO	$LaGaO_3$
DSO	$DyScO_3$
GSO	$GdScO_3$
YAO	$YAlO_3$
LSAO	$LaSrAlO_4$
PNO	$PrNiO_3$
PAO	$PrAlO_3$
LSAT	$(LaAlO_3)_{0.3}$-$(Sr_2Al_{0.5}Ta_{0.5}O_6)_{0.7}$
XAS	x-ray absorption spectroscopy
REXS	resonant elastic x-ray scattering
CI	configuration interaction
TEY	total electron yield
FY	fluorescence yield
PLD	pulsed laser deposition
AFM	atomic force microscopy
XRD	x-ray diffraction
RSM	reciprocal space mapping
LDic	linear dichroism

Acknowledgements

First, my deepest thank to Prof. Keimer for his teaching, supervision and support. I appreciate a lot for giving me the chance to stay here with great time, for his suggestion in some really frustrated times during this phd period. Thank to Prof. Dressel as my second supervisor, for his comments and supports. Thank to Prof. Büchler as the chairman for the examination.

Many thanks for Dr. Eva Benckiser as my day-by-day supervisor, especially your patience and suggestions whenever I encounter troubles. Thanks very much for your scientific attitude that taking every experimental results so seriously, which encourages me to go deeper and learn more. Without both of your correction and comments, this thesis could not have reached the present form.

Then I would like to thank all the work teams, Alex Frano for your supports from teaching me how to start with a normal XRD experiment, especially your explanation of x-ray diffraction in an Artist's way, Yi Lu for all the discussions and helps in interpreting the experimental results, Maurits Haverkort for all the suggestions and clear explanations of physical concepts, Georg Cristiani for the great samples and the early morning discussions, Agnes Szoekefalvi-Nagy and Peter Wochner for x-ray diffraction experiments, Martin Bluschke, Friederike Wrobel and Christopher Dietl for our team during Bessy beamtimes. Xiaoping Yang for your input in the LDA calculations.

My personal thanks go to my office mates with whom I spent a pleasant time: Daniel Propper, Yi Lu, Maximilian Krautloher, Michaela Souliou, Peter Yordanov, Paul Popovich. To the old and current members in x-ray scattering group: Sangita Baniya, Uba Nwankwo, Matthias Hepting and Vladimir Hinkov as well as the members in Keimer's group: Santi Blanco-Canosa, Juan Porras, Junghwa Kim, Alex Charnukha, Yulia Matiks, Kuofeng Tseng, Youngie Um, Dr. Hanns-Ulrich Habermeier, Michael Schulz, Dr. Gennady Logvenov, Manfred Ohl, Benjamin Stuhlhofer, Stephan Heinze and so on. Thanks for all the discussions and providing a good environment here.

I thank Partrick Audehm, Sebastian Bruck for all the supports during Bessy beamtime as well as the following data analysis and discussions together with Dr. Eberhard Goering and Sebastian Macke. Thanks for the assistance from Bessy beamline scientist W. Mahler and B. Zada.

I would also like to thank our current secretary Mrs. Balkema and the former secretary Mrs. Hagemann in dealing with all the documental things, and help me call the in-house technician to fix the office heater every year. Thank to Mrs. King in helping me to extend the visa several times. Thanks to Dr. Eva Rose, Dr. Hans-Georg Libuda for all the helps during the enrollment in the university of Stuttgart.

I thank my Chinese friends in spending the happy spare time with me, we explored Europe especially Germany for beautiful sightseeing, fantastic church culture and delicious food. All the experiences were recorded by photos which will be as my forever memory. Especially the traveling in Strasbourg, I met and knew my husband.

Last my great thank to my beloved family. For my parents, brother and sister, thank you for your trust, understanding and encouragement all the time. Special thanks to my husband Chengxiang Zhu. All these loves make my world so beautiful.

Abstract

Despite extensive research for decades, cuprates still play the dominant role for high-T_c superconductors and the mechanism for the superconductivity is of considerable debate. The key ingredients of the electronic properties of cuprates include no orbital degeneracy, spin-one-half, quasi-two dimensionality and strong antiferromagnetic correlations. There is no high T_c superconductor found among the nickel oxides although Nickel is next to Copper in the periodic table.

Rare-earth nickelates heterostructures were proposed as candidates to potentially exhibit the same electronic structure [20], and the past years have seen several attempts to realize these properties, but no high-T_c superconductivity was reported so far. In particular, superlattices composed of the paramagnetic metal $LaNiO_3$ (LNO) and a large band-gap insulator RXO_3 (RXO) with R = rare-earth ion and X = trivalent cation, were studied in detail. Both materials exhibit a perovskite-type structure. One important aspect of the electronic structure, in analogy to the cuprates is the orbital occupation of the Ni d-orbitals. In LNO, the nominal Ni^{3+} electron configuration is $3d^7 : t_{2g}^6 e_g^1$ due to the cubic crystal field of the octahedrally coordinated oxygen ligands, i.e. an unpaired electron with $S = 1/2$ occupies the e_g orbitals ($x^2 - y^2$ and $3z^2 - r^2$). While studies on bulk LNO have shown that the e_g levels are degenerated, epitaxial heterostructuring offers new routs to manipulate orbital occupations via quantum confinement, strain induced by the underlying substrate and the choice of the second, insulating material as demonstrated by recent theoretical and experimental work [11, 48, 49, 51, 52, 53]. More precisely, the effect of quantum confinement is expected to reduce the three dimensional bulk band dispersion of the Ni $d_{3z^2-r^2}$ state along the z-direction, resulting in a lifting of e_g orbital degeneracy by lowering the $x^2 - y^2$ state. Biaxial strain induces a difference between the in-plane and apical Ni-O bond lengths, giving rise to an e_g orbital splitting and a modification of the bandwidth. Depending on the sign of biaxial strain, compressive or tensile, this possibly results in a preferentially occupation of one of the e_g orbtials. The effect of different trivalent ions X, e.g. Al, Ga, In or Sc, in the insulating layer is to change the hybridization between the Ni $d_{3z^2-r^2}$ orbital and O $2p_z$ orbital, thus the X-O-Ni hybridization along the surface normal direction serves as a tuning parameter. As the ionic radius of X increases, the overlap of X s - O $2p_z$ is expected to be reduced, resulting in the enhanced hybridization of Ni $d_{3z^2-r^2}$ - O $2p_z$ and an enhanced $d_{x^2-y^2}$ orbital occupation.

The present Phd work reports an experimental investigation of layer-resolved orbital occupations, which allow a direct, quantitative comparison with theoretical calculations and therefore provide important information on the possibility to manipulate the electronic structure in nickelate-based heterostructure. We used orbital reflectometry, a new method combining x-ray absorption and x-ray reflectivity to study layer-resolved orbital occupations. In x-ray absorption measurements, linearly polarized soft x-rays tuned to the Ni L edge were used to measure absorption spectra. The absorption intensities are directly proportional to the imaginary part of the layer-averaged scattering factor. For the quantitative analysis, we applied the sum rule for linear dichroism, which relates the ratio of holes in the Ni e_g orbitals to the energy-integrated absorption intensities across the Ni L edge. In order to partially separate the influence of strain and interfacial effects induced by different X ions on the orbital polarization, we performed resonant reflectivity measurements. First, the specularly reflected beam intensity at fixed energies, resonant and non-resonant, was analyzed to obtain a proper structural model of the superlattice. To account for the strong resonances, we used the measured linearly polarization absorption data scaled to theoretical values of the scattering factor as input for the fitting routines. In a second step, the energy- and polarization-dependent resonant reflectivity with fixed momentum was measured. The momentum transfer q_z was chosen to be particularly sensitive to a possible difference between interface and inner layer of the LNO layer stack and allowed us to map out layer-resolved orbital profiles. Two systems were investigated:

First, we focused on LNO-based heterostructures, with a structural composition of 4 unit cell (u.c.) LNO and equally thick layer stacks of the band insulators RXO (R = La, Gd, Dy and X = Al, Ga, Sc). The results allowed us to partly disentangle the orbital polarization originating from strain, affecting all four LNO layers in the stack, from the change in chemical composition across the LNO-RXO interface, which largely affects the outer two interfacial layers. The strain dependence of both, the energy splitting between e_g levels (i.e. the energy difference between $d_{x^2-y^2}$ and $d_{3z^2-r^2}$ levels) extracted from a comparison of the x-ray absorption spectra with cluster calculations and the inner layer orbital polarization determined by orbital reflectometry indicate a linear orbital-lattice coupling and confirm the stabilization of the planar $d_{x^2-y^2}$ orbital under tensile strain with values of orbital polarization up to $P = 25\,\%$. Such an simple linear orbital-lattice interaction is surprising, when considering the very complex crystal structures of these materials [116, 117]. Furthermore

our results indicate that strain is the most effective control parameter, whereas the influence of the chemical composition of the blocking layers falls into a comparatively narrow band of width ~5%, at least for superlattices investigated here. The direct and quantitative comparison with theoretical results performed within the scope of this thesis is an important feedback for the theory and the rational design on nickelate heterostructures in general.

In the second part of this thesis, we report the investigation of the orbital properties of $PrNiO_3$-$PrAlO_3$ (PNO-PAO) superlattices. Different from bulk LNO, which stays paramagnetic and metallic down to the lowest temperatures, bulk PNO shows a metal-insulator transition and magnetic order below a common temperature of $T \approx 130\,\mathrm{K}$. Very recent transport, x-ray scattering and Raman experiments demonstrated that the electronic and magnetic properties can be tuned by strain and confinement in heterostructures of PNO [60]. It was shown by us and others that the metal-insulator transition can be suppressed in thin films grown epitaxially under compressive strain, while a bulk-like transition is observed under tensile strain. When confined in a PNO-PAO superlattice and compressively strained, the PNO layers retain their comparatively high conductivity down to lowest temperatures, but show antiferromagnetic order below $\sim 100\,\mathrm{K}$ for layer thicknesses of 4 u.c. We identified this phase as a possible realization of a pure spin density wave. In contrast, superlattices under tensile strain show a robust insulating phase with spin and possible charge order. In the present thesis, we performed x-ray absorption and resonant reflectometry measurements on PNO-PAO superlattices under compressive and tensile strain, in order to investigate the local electronic structure of Ni and its temperature dependence.

For superlattices under compressive strain, the low-temperature x-ray absorption spectra are almost identical to those measured at room temperature, indicating that the magnetic order hardly change the electronic structure and the relative orbital occupation. The situation is different for PNO-PAO superlattices under tensile strain. First, the low temperature absorption spectra show a double-peak structure at both Ni L_3 and Ni L_2 edges, with an energy splitting of $\sim 1.6\,eV$. The fine structure of the absorption spectra of PNO-PAO superlattices under tensile strain is almost identical to those of bulk PNO. For bulk PNO this multiplet structure has been interpreted as a signature of charge order with two non-equivalent NiO_6 octahedra at low temperatures [112], in agreement with the robust spin and charge order below $\sim 160\,\mathrm{K}$ reported in Ref. [60]. A second important observation for the superlattices under tensile strain is that our quantitative analysis reveals a reduced orbital polarization in the low temperature phase, which can be understood in a simplified Ni $3d^{7-\delta}$ - $3d^{7+\delta}$ charge order picture, where the admixture of the $3d^8$ configura-

tion, with nominally one electron in each e_g orbital due to Hund's coupling, effectively reduces the orbital polarization below the metal-insulator transition temperature, in qualitative agreement with theoretical scenarios [93].

From our resonant reflectometry study we observe a similar linear orbital-lattice interaction as compared to the LNO-based superlattices. A tendency towards higher orbital polarizability is observed for PNO-PAO superlattices, which possibly is related to the increase of octahedral distortions in PNO-based superlattices, compared to those based on LNO, the latter exhibiting a tolerance factor closer to one. This tendency for distorted structures with tilts and rotations of the NiO_6 octahedra was also predicted by recent calculations based on the generalized gradient approximation and was attributed to the difference in hybridization between Ni *d*- and O *p*-orbitals [111]. Such a quantitative comparison of experiment and theory is important for the design of "orbitally engineered" oxide heterostructures and their potential applications.

In the third part of the thesis, we report results indicating that orbital reflectometry is a uniquely sensitive probe of octahedral rotation pattern in oxide superlattices.

Zusammenfassung

Trotz jahrzehntelanger umfassender Forschung spielen Kuprate immer noch die dominante Rolle auf dem Gebiet der Hochtemperatursupraleiter und der Mechanismus der Supraleitung ist weiterhin Gegenstand wissenschaftlicher Diskussion. Die wesentlichen Bestandteile der elektronischen Struktur der Kuprate sind das Fehlen von orbitaler Entartung, ein Spin von 1/2, quasi Zwei-Dimensionalität und starke antiferromagnetische Korrelationen. Unter den Nickeloxiden wurde bisher noch kein Supraleiter gefunden, obwohl Nickel im Periodensystem neben Kupfer zu finden ist.

Seltenerdnickelat-Heterostrukturen wurden als Kandidaten vorgeschlagen, die möglicherweise die gleiche elektronische Struktur wie die Kuprate vorweisen [20]. In den vergangenen Jahren wurden vielfältige Versuche unternommen diese Eigenschaften zu realisieren, aber bisher gibt es keinen Bericht von Hochtemperatursupraleitung. Insbesondere wurden Übergitter zusammengesetzt aus dem paramagnetischen Metall $LaNiO_3$ (LNO) und dem Bandisolator RXO_3 (RXO), mit R = Seltenerdion und X = dreiwertiges Kation, eingehend studiert. Beide Materialien haben eine Perowskit-artige Kristallstruktur. In Analogie zu den Kupraten ist einer der wesentlichen Aspekte der elektronischen Struktur die Besetzung der Ni d-Orbitale. In LNO ist die nominelle Ni^{3+} Elektronenkonfiguration aufgrund der oktaedrischen Koordination der Sauerstoffliganden $3d^7 : t_{2g}^6 e_g^1$, d.h. ein ungepaartes Elektron mit Spin 1/2 besetzt die sogenannten e_g Orbitale ($x^2 - y^2$ und $3z^2 - r^2$). Während Studien an Bulk LNO auf entartete e_g Niveaus hinweisen, zeigen neuere theoretische Arbeiten, dass epitaktische Heterostrukturierung mittels Quantenbeschränkung, Verspannungen induziert durch das darunter liegende Substrat und die Wahl des zweiten, isolierenden Materials, neue Möglichkeiten bieten um die orbitalen Besetzungen zu manipulieren [11, 48, 49, 51, 52, 53]. Genauer gesagt, es wird davon ausgegangen, dass der Effekt der Quantenbeschränkung die drei-dimensionale Banddispersion der Ni $d_{3z^2-r^2}$ Zustände entlang der z-Richtung reduziert, und somit eine Aufhebung der e_g-Orbitalentartung durch Absenkung des $x^2 - y^2$ Zustandes resultiert. Biaxiale Verspannung induziert einen Unterschied zwischen den planaren und apikalen Ni-O Bindungslängen, die wiederum eine Aufhebung der e_g-Orbitalentartung und eine Modifikation der Bandbreite bewirken. Abhängig vom Vorzeichen der

Verspannung, Druck- oder Zugspannung, resultiert diese in einer möglichen Vorzugsbesetzung von einem der e_g Orbitale. Der Effekt der unterschiedlichen dreiwertigen X Ionen in der isolierenden Schicht, z.B. Al, Ga, In oder Sc, besteht darin, dass die Hybridisierung zwischen dem Ni $d_{3z^2-r^2}$ Orbital und dem O $2p_z$ Orbital verändert wird. Daher dient die X-O-Ni Hybridisierung entlang der Oberflächennormale als Anpassungsparameter. Wenn der X Ionenradius ansteigt, wird erwartet, dass der X s- O $2p_z$ Überlapp reduziert wird, so dass eine verstärkte Ni $d_{3z^2-r^2}$- O $2p_z$ Hybridisierung und eine bevorzugte $d_{x^2-y^2}$ Orbitalbesetzung resultiert.

Die vorliegende Doktorarbeit berichtet über eine experimentelle Studie der lagenaufgelösten orbitalen Besetzungen in Nickelat-basierten Übergittern, welche einen direkten, qualitativen Vergleich mit theoretischen Vorhersagen erlaubt und deshalb wichtige Informationen über die mögliche Manipulation der elektronischen Struktur mittels Heterostrukturierung liefert. Um die lagenaufgelösten orbitalen Besetzungen zu studieren haben wir " Orbitale Reflektometrie" genutzt, eine neue Methode, die Röntgenabsorption und Röntgenreflektometrie verbindet [8]. Für die Röntenabsorptionsmessungen wurden linear polarisierte weiche Röngtgenstrahlen abgestimmt auf die Ni L Kante verwendet. Die Absorptionsintensitäten sind direkt proportional zu dem Imaginärteil des lagengemittelten Streufaktors. Für die quantitative Analyse haben wir die Summenregel für den linearen Dichroismus angewendet, die das Verhältnis der Löcher in den Ni e_g Orbitalen mit den über die Ni L Kante energieintegrierten Absorptionsintensitäten in Zusammenhang setzt. Um den Einfluss der Verspannung und die Grenzflächeneffekte, induziert durch die verschiedenen X Ionen, auf die orbitalen Besetzungen teilweise separieren zu können, haben wir resonante Reflektivitätsmessungen durchgeführt. Zunächst wurden die spekular reflektierten Strahlintensitäten bei fester Energie, resonant und nicht-resonant, analysiert um ein geeignetes Strukturmodel des Übergitters zu erhalten. Um die starken Resonanzen zu berücksichtigen, wurden die gemessenen linear polarisierten Absorptionsdaten an die theoretischen Werte der Streufaktoren skaliert und als Eingabe für die Fitroutinen benutzt. In einem weiteren Schritt wurden die energie- und polarisationsabhängigen Reflektivitäten bei festem Impulstransfer gemessen. Der Impulstransfer q_z wurde so gewählt, dass er besonders sensitiv auf einen möglichen Unterchied zwischen den Grenzflächenlagen und den inneren Lagen der LNO Schicht ist, was es uns ermöglicht hat die lagenaufgelösten orbitalen Profile abzubilden. Zwei Systeme wurden untersucht:

Als erstes haben wir uns auf die Untersuchung von LNO-basierten Heterostrukturen, mit einer strukturellen Zusammensetzung von 4 Einheitszellen LNO und gleich dicken Schichten des Bandisolators RXO ($\mathrm{R} = \mathrm{La}, \mathrm{Gd}, \mathrm{Dy}$ und

$X = \mathrm{Al}, \mathrm{Ga}, \mathrm{Sc}$) konzentriert. Die Ergebnisse erlaubten uns die orbitale Polarisation, verursacht durch die Verspannung, welche alle vier LNO Lagen in der Schicht gleichermassen betrifft, und die orbitale Polarisation, die durch Änderung der chemische Zusammensetzung über die LNO-RXO Grenzfläche verursacht wird und stärker die äusseren Grenzflächenlagen betrifft, teilweise zu separieren. Die Verspannungs-Abhängigkeit der Energieaufspaltung der e_g Niveaus (d.h. der Energieunterschied zwischen dem $d_{x^2-y^2}$ und $d_{3z^2-r^2}$ Niveau) bestimmt durch einen Vergleich der Röntgenabsorptionsspektren mit Clusterrechnungen, sowie die durch orbitale Reflektometrie bestimmte Polarisation der inneren Lagen deuten auf eine lineare Orbital-Gitter-Kopplung hin und bestätigen die Stabilisierung des planaren $d_{x^2-y^2}$ Orbitals unter Zugspannung mit Werten der orbitalen Polarisation bis zu $P = 25\%$. Eine solche einfache, lineare Orbital-Gitter-Wechselwirkung ist überraschend, wenn man die sehr komplexe Struktur dieser Materialien in Betracht zieht [116, 117]. Desweiteren deuten unsere Ergebnisse an, dass die Verspannung der effektivste Kontrollparameter ist, wohingegen der Einfluss der chemischen Komposition der RXO-Sperrschicht, zumindest für die hier untersuchten Übergitter, nur in einen vergleichsweise schmalen Bereich von $\sim 5\,\%$ fallen. Der direkte und quantitative Vergleich mit theoretischen Ergebnissen, der im Rahmen dieser Doktorarbeit vorgenommen wurde, ist eine wichtige Information für die Theorie und die zukünftige Gestaltung von Nickelat-Heterostrukturen generell.

Im zweiten Teil dieser Arbeit berichten wir über die Untersuchung der orbitalen Eigenschaften von $\mathrm{PrNiO_3}$-$\mathrm{PrAlO_3}$ (PNO-PAO) Übergittern. Anders als Bulk LNO, welches paramagnetisch und metallisch bis zu tiefsten Temperaturen bleibt, zeigt Bulk PNO einen Metall-Isolator-Übergang und magnetische Ordnung unterhalb einer gemeinsamen Temperatur von $T \approx 130\,\mathrm{K}$. Kürzlich wurde mittels Transportmessungen, Röntgenstreuung und Raman Experimenten gezeigt, dass die elektronischen und magnetischen Eigenschaften durch Verspannung und Eingrenzung in Heterostrukturen von PNO manipuliert werden können [60]. Es wurde durch uns und andere gezeigt, dass der Metall-Isolator-Übergang in Dünnfilmen unter epitaktischer Druckspannung unterdrückt werden kann, während ein bulk-artiger Übergang für Zugspannung beobachtet wird. Eingegrenzt in einem PNO-PAO Übergitter unter Druckspannung, ist die vergleichsweise hohe Leitfähigkeit der PNO Schichten bis zu tiefsten Temperaturen erhalten, aber antiferromagnetische Ordnung unterhalb $\sim 100\,\mathrm{K}$ wird für Schichtdicken von 4 Einheitszellen beobachtet. Wir haben diese Phase als eine mögliche Realisierung einer reinen Spindichtewelle identifiziert. Im Gegensatz hierzu zeigen Übergitter unter Zugspannung eine robuste isolierende Phase mit Spin- und Ladungsordnung. In der vorliegenden Doktorarbeit haben wir Röntgenabsorptions- und resonante Reflektivitätsmessungen an PNO-PAO Übergitter unter Druck- und Zugspannung durchgeführt um die lokale elektronische Struktur von Ni und deren Temperaturabhängigkeit zu untersuchen. Für Übergitter unter Druckspannung sind die Tieftemperatur-Röntgenabsorptionsspektren nahezu identisch zu denen die bei Raumtemperatur gemessen wurden, was andeutet das die magnetische Ordnung die elektronische Struktur und die relative orbitale Besetzung nur wenig ändert. Die Situation ist deutlich verschieden für PNO-PAO Übergitter unter Zugspannung. Erstens zeigen die Tieftemperaturabsorptionspektren eine Doppelpeakstruktur, sowohl an der Ni L_3, wie auch an der Ni L_2 Kante, mit einer Energieaufspaltung von $\sim 1.6\,\mathrm{eV}$. Diese Feinstruktur der Absorptionsspektren ist nahezu identisch zu denen von Bulk PNO. Für Bulk PNO wurde diese Multipletstruktur als Merkmal von Ladungsordnung mit zwei nicht-äquivalenten NiO_6 Oktaedern bei tiefen Temperaturen interpretiert [112], in Übereinstimmung mit der in Ref. [60] berichteten robusten Spin- und Ladungsordnung unterhalb von $\sim 160\,\mathrm{K}$. Eine zweite wichtige Beobachtung für Übergitter unter Zugspannung ist die reduzierte orbitale Polarisation in der Tieftemperaturphase die sich aus unserer quantitativen Analyse ergeben hat und welche in einem vereinfachten Ni $3d^{7-\delta}$ - $3d^{7+\delta}$ Ladungsordnungsbild verstanden werden kann, wo die Beimischung der $3d^8$ Konfiguration mit nominal einem Elektron in jedem e_g Orbital aufgrund der Hundschen Kopplung, effektiv die orbitale Polarisation unterhalb der Metall-Isolator-Übergangstemperatur reduziert [93]. Basierend auf den Ergebnissen der orbitalen Reflektrometrie beobachten wir eine ähnliche, lineare Orbital-Gitter-Kopplung im Vergleich mit den LNO-basierten Übergittern. Für PNO-PAO Übergitter wird eine Tendenz zu höherer orbitaler Polarisierbarkeit beobachtet, die möglicherweise mit den grösseren Oktaederverzerrungen, im Vergleich zu LNO, in Zusammenhang steht. LNO weist einen Toleranzfaktor näher bei eins auf. Eine solche Tendenz für verzerrte Strukturen mit Verkippungen und Drehungen der NiO_6 Oktaeder wurde kürzlich auch von Rechnungen basieren auf der " Generalized Gradient Approximation" vorhergesagt und dem Unterschied in der Hybridisierung zwischen Ni d- und O p- Orbitalen zugeordnet [111]. Ein solcher qualitativer Vergleich von Experiment und Theorie ist wichtig für das Design von " orbital technisierten" Oxidheterostrukturen und deren potentielle Anwendung.

Im dritten Teil dieser Doktorarbeit berichten wir von Ergebnissen, die aufzeigen, dass die orbitale Reflektometrie eine einzigartig sensitive Messmethode von Oktaederrotationsmustern in Oxidübergittern ist.